

SPACE, TELECOMMUNICATIONS AND RADIOSCIENCE LABORATORY



STARLAB
DEPARTMENT OF ELECTRICAL ENGINEERING / SEL
STANFORD UNIVERSITY • STANFORD, CA 94305

CYCLOTRON RESONANT SCATTERING OF ENERGETIC ELECTRONS BY ELECTROMAGNETIC WAVES IN THE MAGNETOSPHERE

By

Hung-chun Chang

September 1983

Technical Report No. E414-1

Prepared under

National Aeronautics and Space Administration
Grant NGL-05-020-008

Atmospheric Sciences Section of the National Science Foundation
Grant ATM-80-18248

Office of Naval Research
Grant N00014-82-K-0489

**CYCLOTRON RESONANT SCATTERING OF ENERGETIC ELECTRONS
BY ELECTROMAGNETIC WAVES IN THE MAGNETOSPHERE**

by

Hung-chun Chang

September 1983

Technical Report No. E414-1

Prepared under

**National Aeronautics and Space Administration
Grant NGL-05-020-008**

**Atmospheric Sciences Section of the National Science Foundation
Grant ATM-80-18248**

**Office of Naval Research
Grant N00014-82-K-0489**

Space, Telecommunications and Radioscience Laboratory

Stanford Electronics Laboratories

Stanford University Stanford, California

**A DISSERTATION
SUBMITTED TO THE DEPARTMENT OF ELECTRICAL ENGINEERING
AND THE COMMITTEE ON GRADUATE STUDIES
OF STANFORD UNIVERSITY
IN PARTIAL FULFILLMENT OF THE REQUIREMENTS
FOR THE DEGREE OF
DOCTOR OF PHILOSOPHY**

**By
Hung-chun Chang
September 1983**

**This Ph.D. dissertation is dedicated to
my parents
Mr. and Mrs. M. K. Chang**

ABSTRACT

As a magnetoplasma, the earth's magnetosphere can support a variety of electromagnetic wave modes in a wide range of frequencies. An important example is the right-hand elliptically polarized whistler mode wave that propagates at frequencies below the electron gyrofrequency. The whistler mode waves can interact through doppler-shifted resonance with energetic electrons trapped in the geomagnetic field. Due to these interactions, the waves can be amplified and the distribution of the energetic electrons can be disturbed. In this work we consider one important class of wave-particle interactions in the inner magnetosphere, namely, the cyclotron resonance interaction between coherent VLF waves and radiation belt electrons. One consequence of such interactions is the pitch angle scattering of the electrons and the resultant precipitation of these electrons into the ionosphere where they can cause ionization and conductivity enhancements, heating and the emission of X rays and light.

We employ a test particle simulation method to study the wave-induced perturbations of electron trajectories. To include the quasi-relativistic electron energies up to at least hundreds of keV, the well-known equations of motion for the cyclotron resonance wave-particle interaction are rewritten by taking into account relativistic effects. Based on these equations and the test particle scheme, a computer model is developed for determining the transient evolution of the energy flux into the ionosphere of electrons precipitated due to interactions with VLF wave packets propagating longitudinally along the geomagnetic field lines. By taking account of the group travel times of wave components of different frequency as well as the wave amplitude variations resulting from the signal dispersion, the transient precipitation model is applied to the cases of variable frequency VLF signals, such as whistlers, chorus emissions and triggered emissions. Our results show that, under conditions of moderate wave intensities, the total deposited energy density is not strongly dependent on the frequency-time format of the input signal. However, when wave growth is considered, the signal with rising frequency is shown to be more efficient in inducing particle precipitation than the signal with falling frequency.

The computer model is useful in examining the characteristic shape of the wave-induced precipitation pulse under a wide range of magnetospheric conditions. It thus provides a theoretical basis for experiments designed to detect precipitation induced by coherent VLF waves. We have compared the predictions of our model, i.e., the

precipitation flux level, pulse shape and associated time relationships, with ground based observations of the ionospheric effects of particle precipitation. The results demonstrate that our model can be used to interpret the observed experimental results and to diagnose some features of the energetic electron distributions in the magnetosphere. A potential application is to plan future experiments to detect wave-induced electron precipitation.

ACKNOWLEDGMENTS

This research was supervised by Professors R. A. Helliwell and U. S. Inan. I wish to express my sincere gratitude for their continual support, patient guidance and encouragement during the course of this work. Their advise and critical reading have considerably improved the content of this report.

I owe a great deal to Drs. T. F. Bell and D. L. Carpenter for their constant interest in this work and for their valuable suggestions and comments on many aspects of this research. I also wish to thank my third reader Prof. C. F. Quate for reviewing this manuscript.

I would like to thank all the other members of the VLF group of the Radioscience Laboratory of Stanford for their help, cooperation and friendship. Special thanks are due to Vikas Sonwalkar and Curt Carlson, with whom I had the pleasure of not only sharing the same office but also having numerous stimulating discussions.

I am grateful to my parents, sister and brother for their love, moral support and encouragement throughout the course of my academic years.

This research was supported in part by the National Aeronautics and Space Administration under grant NGL-05-020-008, in part by the Division of Atmospheric Sciences of the National Science Foundation under grant ATM-80-18248, and in part by the Office of Naval Research under grant N00014-82-K-0489. The computer calculations were made using the CDC7600 and CRAY-1 computers of the National Center for Atmospheric Research (NCAR) in Boulder, Colorado, through a Remote Job Entry Terminal at Stanford. Our use of this facility was made possible by a Computer Resources grant from NCAR. NCAR is sponsored by the National Science Foundation.

TABLE OF CONTENTS

Chapter	Page
I. INTRODUCTION	1
A. WAVE-PARTICLE INTERACTIONS IN THE MAGNETOSPHERE . . .	1
B. VLF-WAVE-INDUCED ENERGETIC ELECTRON PRECIPITATION . . .	5
C. OVERVIEW AND ORGANIZATION OF THE REPORT	7
D. CONTRIBUTIONS OF THE PRESENT WORK	9
II. PHYSICS OF GYRORESONANT WAVE-PARTICLE INTERACTIONS . . .	11
A. MODELS OF THE MAGNETOSPHERIC MEDIUM	11
B. VLF WHISTLER MODE WAVES IN THE MAGNETOSPHERE	13
C. DYNAMICS OF TRAPPED RADIATION BELT PARTICLES	16
D. CYCLOTRON RESONANT WAVE-PARTICLE INTERACTIONS . . .	20
E. SCATTERING OF NEAR-LOSS-CONE PARTICLES	28
F. ENERGETIC ELECTRON DISTRIBUTION FUNCTIONS	36
III. TRANSIENT ENERGETIC ELECTRON PRECIPITATION INDUCED BY VLF WAVE PACKETS IN THE MAGNETOSPHERE	41
A. INTRODUCTION	41
B. CYCLOTRON RESONANCE VELOCITY CURVES	42
C. FORMULATION OF THE TRANSIENT PROBLEM	46
D. PRECIPITATION INDUCED BY VARIABLE FREQUENCY SIGNALS .	54
IV. APPLICATION OF THE THEORETICAL MODEL	59
A. INTRODUCTION	59
B. APPLICATION TO A LIGHTNING-GENERATED WHISTLER	60
C. COMPARISON WITH GROUND BASED OBSERVATIONS	66
D. COMPARISON WITH SATELLITE OBSERVATIONS	77
E. DISCUSSION	82
V. SUMMARY AND RECOMMENDATIONS	85
A. SUMMARY	85
B. RECOMMENDATIONS FOR FUTURE WORK	87
APPENDIX A.	91
APPENDIX B.	93
APPENDIX C.	95
REFERENCES	100

ILLUSTRATIONS

Figure	Page
1.1 A sketch of the magnetosphere	2
2.1 Coordinate system for the dipole field geometry	12
2.2 Normalized electron density versus geomagnetic latitude at $L = 4$ for diffusive equilibrium and collisionless models	13
2.3 Trajectory of an energetic particle in the earth's dipole field	18
2.4 Coordinate system for the equations of motion	21
2.5 Equatorial resonance velocity vs. equatorial pitch angle for different normalized frequencies $\Lambda = \omega/\omega_{Heq}$	25
2.6 Equatorial resonance energy versus equatorial pitch angle for the same parameters as in Figure 2.5	26
2.7 Equatorial resonance energy versus equatorial cold plasma density for different normalized frequencies Λ	27
2.8 Trajectory of a relativistic test particle under the influence of a monochromatic wave of 5.46 kHz having $B_w = 7.5$ pT at $L = 2$	29
2.9 Dependence of particle scattering on the initial Larmor phase and the wave intensity	31
2.10 The rms scattering versus the particle energy for the same magneto- plasma and wave parameters as in Figure 2.8	32
2.11 The rms scattering versus particle energy for a half-sided wave structure	34
2.12 The envelope of rms scattering pattern versus particle energy for three different wave frequencies at $L = 2$	35
2.13 The energy spectrum of precipitating particles for the case of Figure 2.10	39
3.1 Resonant interaction between a particle and a monochromatic wave pulse	43
3.2 Resonance velocity curves for the cases of variable frequency waves	45
3.3 Schematics describing the wave-particle interactions and the calculation of the individual responses	48
3.4 The responses due to four different positions of the wave front as it propagates along the field line	51
3.5 Transient precipitated energy flux induced by a wave pulse at $L = 4$	53
3.6 Precipitated energy fluxes induced by variable frequency waves	56

ILLUSTRATIONS (Cont.)

Figure	Page
3.7 The precipitated energy fluxes for the same input signal formats as in Figure 4.3 except that a 20 db wave growth near the principal interaction region is taken into account	58
4.1 The frequency-time format observed at the equatorial plane of a lightning-generated signal propagating on the $L = 4$ field line, termed a half-hop whistler	61
4.2 The v_R curves for a particle whose adiabatic parallel velocity is given by the dashed curve and the propagating whistler signal described in Figure 4.1	63
4.3 The wave amplitude variation versus latitude experienced by the test particle shown in Figure 4.2 as it travels within the whistler wave packet	64
4.4 The transient precipitation for the whistler described in Figure 4.1	65
4.5 Field line model showing the whistler-induced precipitation	67
4.6 The frequency-time formats of the whistler used in the computer model	68
4.7 Precipitation pulses induced by the one-hop whistler given in Figure 4.6	69
4.8 Schematic showing the paths of scattered electrons and their precipitation effects	72
4.9 Time lag between the peak of the flux and the arrival of the wave as function of n_{eq} for DE and collisionless models	74
4.10 Peak flux level versus n in equation (2.28) with Φ_E as a parameter for the case of direct precipitation for the photometer case	76
4.11 The equatorial cold plasma density and the equatorial bounce loss cone as functions of L value used for the results shown in Figure 4.12	78
4.12 The envelope of rms scattering pattern vs. energy for the near-loss-cone particles resulting from one-pass interactions with a 23-keV wave on three different L shells	80
A1 Definition of the differential energy spectrum	92
C1 Perturbation of electron population resulting from resonant interaction with a 5.95 kHz wave.	96
C2 Curves showing the relationship between pitch angle and equatorial resonant parallel velocity for various wave frequencies	97
C3 Equatorial resonance energy at different pitch angles for resonant wave frequencies of 6.0 kHz and 5.75 kHz	98

I. INTRODUCTION

This research concerns the cyclotron resonant interactions between radiation belt electrons and whistler mode electromagnetic waves in the earth's magnetosphere. One consequence of these interactions is the pitch angle scattering of the particles which in turn results in the precipitation of these initially trapped particles into the ionosphere. The purpose of this chapter is to give a brief introduction to the topic and to review specific contributions of the present work.

A. WAVE-PARTICLE INTERACTIONS IN THE MAGNETOSPHERE

Surrounding the conducting earth is the non-conducting atmosphere, roughly 60–80 km thick, depending on its precise definition. The next layer above the neutral atmosphere is the ionosphere which extends upwards to ~ 1000 km. The ionosphere is a conductive medium, in which a small percentage ($< 0.1\%$) of the atmospheric constituents are ionized due to solar UV and X ray radiation. The region outside the ionosphere is called the magnetosphere. The word 'magnetosphere' was first used by *Gold* [1959]. In this volume of space the motion of charged particles is largely governed by the geomagnetic field. The magnetosphere is filled with a tenuous neutral gas, mainly hydrogen, and an ionized gas with protons as the dominant positive ion. The collision rate is so low that for many purposes the region can be considered collisionless. Thus each particle moves under the influence of the earth's magnetic field, essentially independently of its neighbors.

The large scale morphology of the magnetosphere is controlled by the interaction between the solar wind and the earth's magnetic field. A sketch of the magnetosphere is shown in Figure 1.1. The solar wind, a hot gas of $\sim 10^5$ K consisting mainly of protons and electrons traveling outward from the sun at supersonic speeds of ~ 500 km/s, exerts a pressure on the earth's magnetic field and distorts it into the shape shown in Figure 1.1. The particles of the solar wind enter the earth's magnetosphere in various ways. Some of the energy is introduced at the outer boundary of the magnetosphere, called the magnetopause, located at a distance of about 10 earth radii in the solar direction. In the anti-solar direction there is the magnetotail with undefined length, due to the dragging of the geomagnetic field lines by the solar wind. A bow shock is formed at about 12 earth radii where the kinetic pressure of the solar wind is balanced by the pressure of the earth's magnetic field. In the cusp region the solar wind plasma follows open field lines directly to the ionosphere,

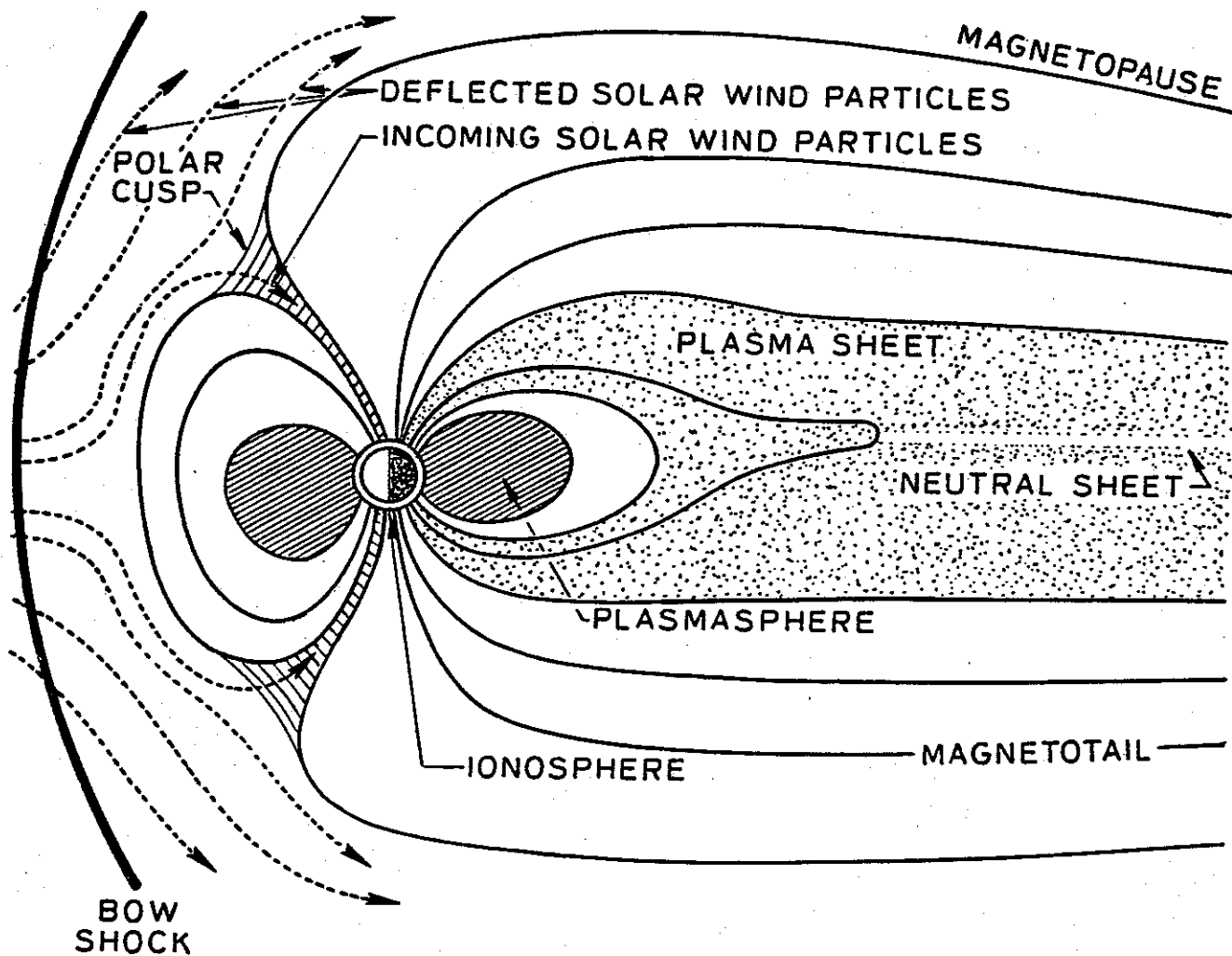


FIGURE 1.1 A SKETCH OF THE MAGNETOSPHERE. It is shown in a noon-midnight meridian plane view.

giving rise to auroras, heating and electromagnetic radiation such as VLF hiss and kilometric radiation.

The magnetosphere is dominated by the magnetic field of the earth. In the inner magnetosphere, i.e., in the region within about 6 earth radii and between about $\pm 66^\circ$ geomagnetic latitudes of the earth, the geomagnetic field can be approximated by a centered dipole. However, further out the dipole symmetry is distorted and the field lines are compressed into a form that departs rather markedly from a dipole field at large radial distances.

The inner magnetosphere is basically a magnetoplasma with thermal electrons and positive ions (mainly protons, and some He^+ and O^+) in the 1-eV or less energy range constituting the background cold plasma. Ionization by solar UV radiation in the daytime F region of the ionosphere is believed to generate the cold plasma, which then flows upward along field lines to fill the inner magnetosphere. The cold plasma electron densities measured at the geomagnetic equator gradually decrease with increasing distance away from the earth up to the region called the plasmapause, at which the electron concentration drops by as much as two orders of magnitude [Carpenter, 1963]. The location of the plasmapause is often near $L=4\sim 5$ during geomagnetic quiet conditions. The region inside this abrupt boundary of cold plasma population is called the plasmasphere.

As a magnetoplasma, the magnetosphere can support a variety of wave modes in a wide range of frequencies. In this report we consider one of these modes, that is, the whistler mode electromagnetic waves propagating in the magnetosphere. The frequency of propagation of the whistler mode waves is below the electron gyrofrequency. In the region of interest the whistler mode wave frequencies are generally in the kHz range, or within the VLF band. The wave is elliptically polarized in general and is right-hand circularly polarized for the case of longitudinal propagation along the static magnetic field line, with the wave field vectors rotating in the same sense as an electron gyrating around the field line.

In addition to the cold plasma composed of thermal particles, the inner magnetosphere is also populated by energetic particles, mainly protons and electrons with energies extending from ~ 100 eV up to hundreds of MeV. These particles are magnetically trapped in the geomagnetic field and form the earth's radiation belts. These charged energetic particles execute a helical gyro motion around the field lines. They also bounce back and forth between two conjugate hemispheres and drift slowly in longitude across the field lines. These undisturbed trajectories are

adequately described by the well-known adiabatic theory, that is, the gyro motion, latitudinal motion, and drifting motion are governed by three adiabatic invariants [Alfvén and Fälthammar, 1963].

This report deals with the resonant interactions between the trapped radiation belt energetic electrons and the whistler mode VLF waves in the magnetosphere. During these wave-particle interactions the waves can be amplified or damped. One important result of these interactions is the loss of the trapped particles out of the magnetosphere. The wave fields perturb the adiabatic motion of the particle and change the particle's pitch angle, that is, inclination angle of the particle momentum with respect to the static magnetic field direction. The result is that the mirror altitude of the latitudinal bounce motion of some particles is lowered, causing those particles to experience increased number of collisions with atmospheric constituents and hence to be precipitated.

The wave-particle resonant interactions can be in the form of either longitudinal (Landau) resonance or cyclotron (gyro) resonance. In the Landau resonance the interactions are achieved through the match of the particle's parallel velocity along the magnetic field line with the phase velocity of the wave, while during cyclotron resonances the particles see a doppler-shifted wave frequency approximately equal to their gyrofrequency [Brice, 1964]. The cyclotron resonance is an important wave-particle interaction process in the inner magnetosphere. Perturbations in the particles' momenta can occur through these cumulative resonant interactions in which the particles observe an approximately stationary wave field for a significant period of time. Exchange of energy between the wave and the particles can also take place through the wave's electric field.

One important class of magnetospheric signals is the narrow-band coherent VLF waves that have attracted much attention in the past two decades. Examples of such signals are natural whistlers generated from lightning, chorus emissions, signals from ground based VLF transmitters, and emissions triggered by these signals. During the past decade active VLF wave injection experiments have been carried out using the Stanford University VLF transmitter at Siple Station in the Antarctic [Helliwell and Katsufakis, 1974]. This transmitter is able to generate both fixed and variable frequency signals. The goal of the wave injection experiments is to study the wave-particle and wave-wave interactions in the magnetosphere on a controllable basis. Such interactions can lead to such interesting processes as amplification, suppression, triggering, and entrainment of waves in the magnetosphere. These experiments

have been highly successful in achieving new discoveries and in understanding the complex response of the magnetosphere to the injection of coherent VLF signals [Helliwell, 1974; Carpenter and Miller, 1976; Inan et al., 1977; Helliwell, 1977; Raghuram et al., 1977a, b; Helliwell and Katsufakis, 1978; Chang and Helliwell, 1979; Helliwell et al., 1980b; Bell et al., 1981; Park, 1981; Tsuruda et al., 1982].

Wave growth and triggered emissions due to the phase bunching and trapping of the energetic electrons are important results of the coherent cyclotron resonance wave-particle interactions in the magnetosphere. These processes have been theoretically studied by numerous authors [Bell, 1964, 1965; Brice, 1964; Bell and Buneman, 1964; Helliwell, 1967, 1970; Das, 1971; Dysthe, 1971; Nunn, 1971, 1974; Sudan and Ott, 1971; Palmadesso and Schmidt, 1971, 1972; Ashour-Abdalla, 1972; Brinca, 1972; Bud'ko et al., 1972; Matsumoto, 1972; Helliwell and Crystal, 1973; Crystal, 1975; Karpman et al., 1974a, b, 1975; Roux and Pellat, 1976, 1978; Vomvoridis and Denavit, 1979, 1980; Vomvoridis et al., 1982; Matsumoto et al., 1980; Bell and Inan, 1981; Matsumoto and Omura, 1981; Helliwell and Inan, 1982; Omura and Matsumoto, 1982].

B. VLF-WAVE-INDUCED ENERGETIC ELECTRON PRECIPITATION

In this report we examine the scattering in pitch angle and the resultant precipitation of energetic electrons from the magnetosphere due to cyclotron resonance interactions. In the auroral region at magnetic latitudes between 65° and 75° , the role of wave-particle interactions in terrestrial auroral precipitation is not well known, although recently Coroniti et al. [1980] have attributed the observed Jovian auroral luminosity to pitch angle scattering by observed VLF chorus emissions. We are especially interested in the precipitation at latitudes below the auroral zones, or at mid-latitudes. Wave-induced precipitation at these latitudes is an important loss process for the population of radiation belt electrons trapped in the inner magnetosphere [Paulikas, 1975]. The precipitating electrons, when colliding with the atmospheric constituents at ionospheric altitudes, cause optical emissions and bremsstrahlung X rays, and create ionization enhancements in the lower ionosphere.

Dungey [1963] and Cornwall [1964] were the first to calculate explicitly the pitch angle scattering of a trapped electron due to the cyclotron resonance interaction with a lightning-generated whistler. The lightning-generated whistlers are but one example of the variety of both coherent and incoherent ELF/VLF waves in the magnetosphere. ELF/VLF plasmaspheric hiss which is always present within the plasmasphere [Thorne et al., 1973] is one example of incoherent wide band electromagnetic signals. Lyons and Thorne [1973] have suggested that ELF whistler mode hiss

is an effective electron scatterer throughout the outer plasmasphere. In the process of interactions with such wide band incoherent waves, individual particles execute a random walk in velocity or momentum space and the pitch angle scatterings can thus be considered as a diffusion process and can be described by computing the diffusion coefficients [Roberts, 1966]. Theoretical estimates of the diffusion coefficient and resultant pitch angle distributions of trapped electrons have been presented by Kennel and Petschek [1966], Lyons *et al.* [1972], Spjeldvik and Thorne [1975], and others.

The pitch angle distribution of geomagnetically trapped electrons is an important factor in determining the trapped flux level as well as the long term behavior of the radiation belts, which are the result of the balance between losses due to wave-induced diffusion and sources, such as radial diffusion. Lyons *et al.*, [1972] used the observed wave turbulence characteristics to derive electron lifetimes and found agreement with observed decay rates. Based on these wave-particle interactions involving incoherent whistler mode turbulence, Lyons *et al.* [1972] and Lyons and Thorne [1973] were able to explain the two-zone structure of the population of radiation belt electrons and attribute the slot in the quiet-time electron population to a local maximum in the rate of pitch angle scattering of electrons by cyclotron resonances with whistler mode waves.

In the present work we investigate the pitch angle scattering induced by another class of whistler mode waves, that is, highly coherent narrowband VLF signals. We shall in particular study the cases of short-duration signals such as natural and triggered emissions, wave pulses injected from ground based transmitters, and lightning-generated whistlers. When interacting with such coherent waves, particles can undergo large pitch angle changes since they can be in resonance with the coherent wave over distances of many hundred wavelengths [Inan *et al.*, 1978]. This process, especially that of transient scattering through the one-pass interaction of the particles with short discrete waves, can not be simply modeled as diffusion in pitch angle.

Electron precipitation induced by natural discrete VLF wave events (whistlers, chorus emissions, noise bursts, etc.) have been observed on numerous occasions [Rosenberg *et al.*, 1971; Helliwell *et al.*, 1973; Foster and Rosenberg, 1976; Lohrey and Kaiser, 1979; Helliwell *et al.*, 1980a; Mende *et al.*, 1980; Rosenberg *et al.*, 1981; Dingle and Carpenter, 1981; Carpenter and LaBelle, 1982]. In these observations

the ionospheric effects of precipitated electrons, such as sub-ionospheric VLF perturbations, X ray emissions, or photoemissions, were found to be in one-to-one correspondence with and therefore believed to be induced by natural VLF waves.

Recent satellite measurements show that electrons in the drift loss cone precipitate from the slot region between the inner and outer radiation zones ($L \sim 2$ to ~ 3.5) and from the outer edge ($L \sim 1.5$ to ~ 1.8) of the inner radiation zone [Imhof *et al.*, 1974, 1981a, b; Vampola and Kuck, 1978; Koons *et al.*, 1981]. Detailed study of the spectral characteristics of the precipitating electrons has suggested that these electrons were precipitated by first-order cyclotron resonance interactions with nearly monochromatic waves, possibly from ground based VLF transmitters. While these measurements amount to indirect evidence of wave-induced precipitation, the first direct observation of energetic electrons precipitated by controlled injection of VLF waves from ground based navigational transmitters has been achieved in the recent SEEP experiments [Imhof *et al.*, 1983a, b].

The effect of coherent VLF waves, both natural and manmade, relative to that of incoherent waves such as plasmaspheric hiss on the long term spatial distribution of trapped electrons is as yet not determined. However, the experimental observations reveal that these waves can have significant short term effects on the loss of electrons from the magnetosphere. One important goal of the Siple wave injection experiments is to investigate how the injected waves can affect the energetic electron population in the magnetosphere and therefore achieve a measure of control of various precipitation-induced processes in the ionosphere.

The purpose of the present work is to study the cyclotron resonant pitch angle scattering of energetic electrons induced by coherent VLF signals propagating in the magnetosphere. One particular goal is to model the transient electron precipitation into the ionosphere due to short-duration discrete VLF waves such that the precipitation signatures of artificially injected VLF wave pulses, natural whistlers, triggered emissions, and other coherent wave events can be quantitatively predicted. It is hoped that this model study can be used to interpret the experimental results related to particle precipitation and to plan future experiments designed to detect such wave-induced particle precipitation.

C. OVERVIEW AND ORGANIZATION OF THE REPORT

The major task in the determination of wave-induced pitch angle perturbations of trapped electrons involves the solution of a set of nonlinear coupled differential

equations. We adopt a test particle computer simulation approach similar to that employed by *Inan* [1977] and *Inan et al.* [1978]. Using this method the trajectories of individual test particles during the interaction with a prescribed wave can be numerically obtained. The wave-induced perturbation of a full distribution of electrons can then be modeled by considering a sufficiently large number of test particles distributed in velocity or momentum space.

The test particle simulation model is generalized by employing a set of equations of motion with relativistic corrections in order to cover a wide range of electron energies as is required in the study of the cyclotron resonant wave-particle interaction for certain magnetospheric parameters. Based on this test particle simulation method and the fundamental concept of a linear slowly time-varying system, a computer model is developed to determine the detailed time variation of the transient precipitated energy flux induced by short-duration VLF waves propagating along the inhomogeneous geomagnetic field lines. This model is capable of dealing with propagating VLF wave packets of either fixed or variable frequency by taking into account the signal dispersion of different wave frequency components. As such, it provides a technique for determining the pitch angle scattering and therefore the precipitation of energetic electrons induced by various coherent signals such as frequency ramps, rising or falling emissions as well as hooks and natural whistlers. This model is useful in examining the dependence of the characteristic shape of the wave-induced precipitation pulse on various magnetospheric parameters

We limit ourselves to the case of longitudinal wave propagation along the static magnetic field lines in which the wave normal direction is parallel to the direction of the magnetic field. This simplification is suitable for wave propagation in a whistler mode duct and thus for the study of ground based observations. It should be noted that although the present work emphasizes wave-induced pitch angle perturbations of those electrons that could contribute to the precipitation at ionospheric heights, the test particle model is general and can be used in the study of coherent wave amplification which involves phase bunching and trapping of electrons with higher pitch angles as well as the wave-induced modification of the trapped particle distribution in a wide range of pitch angles. One example of the full distribution calculations related to the 'quiet band' phenomenon [*Raghuram et al.*, 1977b] is given in Appendix C.

We outline the organization of this report as follows.

Chapter II describes the basic physics of cyclotron resonant wave-particle interactions including models of the magnetoplasma, characteristics of whistler mode waves, dynamics of trapped particles, and relativistic equations of motion.

Chapter III formulates the problem of computing the transient electron precipitation induced by short-duration VLF wave pulses propagating along the geomagnetic field line including the case of variable frequency waves. Input signals of different frequency-time format are then examined.

In Chapter IV we apply the transient precipitation computer model to observed precipitation-induced ionospheric disturbances correlated to VLF wave events. Three cases corresponding to sub-ionospheric VLF perturbations, X ray emissions, and photometer observations are studied in detail. We also compare our theoretical calculations of pitch angle scattering with electron energy spectra observed in satellite measurements.

In the last chapter we summarize and discuss our results and give suggestions for future work.

D. CONTRIBUTIONS OF THE PRESENT WORK

The present work has been reported in a series of papers in the *Journal of Geophysical Research* [Inan et al., 1982; Chang and Inan, 1983a, b; Chang et al., 1983]. The specific contributions are listed as follows.

- 1) The well-known equations of motion for the cyclotron resonance interaction between energetic electrons and coherent VLF waves in the magnetosphere are extended to relativistic energies for the first time. Based on these equations and the relativistic cyclotron resonance condition, a test particle simulation method is used to study the wave-particle interactions between coherent waves and quasi-relativistic electrons. It is suggested that the exact equations be used for electron energy higher than 50 keV (corresponding to a 10% correction in average pitch angle scattering with respect to a nonrelativistic formulation).

- 2) The root mean square pitch angle scattering of the near-loss-cone quasi-relativistic electrons and the corresponding precipitated energy spectrum are calculated and compared with observations of recent satellite experiments. The agreement in the spectral width between the computed and measured spectra supports the suggestions that the observed narrow peaks in precipitated energy spectra may

be caused by monochromatic signals injected into the magnetosphere by VLF transmitters.

3) By numerically taking account of the group travel times of wave components of different frequency as well as the wave amplitude variations resulting from the signal dispersion, a transient precipitation model is generalized to include the case of variable frequency VLF waves. For the first time the time evolution of the precipitated electron energy fluxes into the ionosphere due to magnetospheric signals such as natural whistlers, emissions, hooks can be quantitatively calculated.

4) From the examination of input signals of different frequency-time format, it is concluded that under condition of moderate wave intensities ($B_w < 10$ pT at $L=4$), the total deposited energy density induced by coherent slowly varying signals is not strongly dependent on the input frequency-time format. However, it is found that when wave growth is present, a signal with rising frequency is more efficient than a signal with falling frequency in inducing electron precipitation.

5) The transient precipitation model is applied to three observed correlations between electron precipitation and VLF wave events. The precipitation flux level, pulse shape, and associated time relationships obtained from the model agree well with the reported data.

II. PHYSICS OF GYRORESONANT WAVE-PARTICLE INTERACTIONS

A. MODELS OF THE MAGNETOSPHERIC MEDIUM

In this report we are mainly interested in the 'inner magnetosphere', defined here as the region within ~ 6 earth radii and between $\sim \pm 66^\circ$ geomagnetic latitudes of the earth. In this region the earth's magnetic field is a moderately good centered dipole field with the dipole axis tilted with respect to the rotation axis by about 11.5 degrees. A sketch of the dipole field geometry is shown in Figure 2.1. In this dipole model the equation of a field line in any meridional plane is described by the relation

$$R \cos^2 \lambda = R_0 \cos^2 \lambda_0, \quad (2.1)$$

where R is the distance from the center of the earth, R_0 ($=6370$ km) is the mean radius of the earth, λ is the geomagnetic latitude, and λ_0 is the latitude of the point where the field line intercepts the earth surface. A field line can be identified by the McIlwain's magnetic shell parameter L defined as

$$L = R_{eq}/R_0 = 1/\cos^2 \lambda_0, \quad (2.2)$$

where R_{eq} is the geocentric distance of the field line at the equator. The strength of the magnetic field in this dipole model is given by

$$B_0(R, \lambda) = 3.12 \times 10^{-5} \left(\frac{R_0}{R} \right)^3 (1 + 3 \sin^2 \lambda)^{1/2} \text{ wb/m}^2. \quad (2.3)$$

The inner magnetosphere is populated mainly by electrons and protons with energy in the order of 1 eV, constituting a background cold plasma. In the presence of the static magnetic field, a charged particle undergoes a motion of gyration along the field line. Electrons and protons gyrate in opposite directions because of their different signs of charge. The frequency of gyration for the 'cold' plasma electrons, called electron gyrofrequency, is given by

$$\omega_H = \frac{eB_0}{m}, \quad (2.4)$$

where e and m are the electronic charge and rest mass of electron, respectively. One important feature of this region is the existence of the plasmopause, discovered in

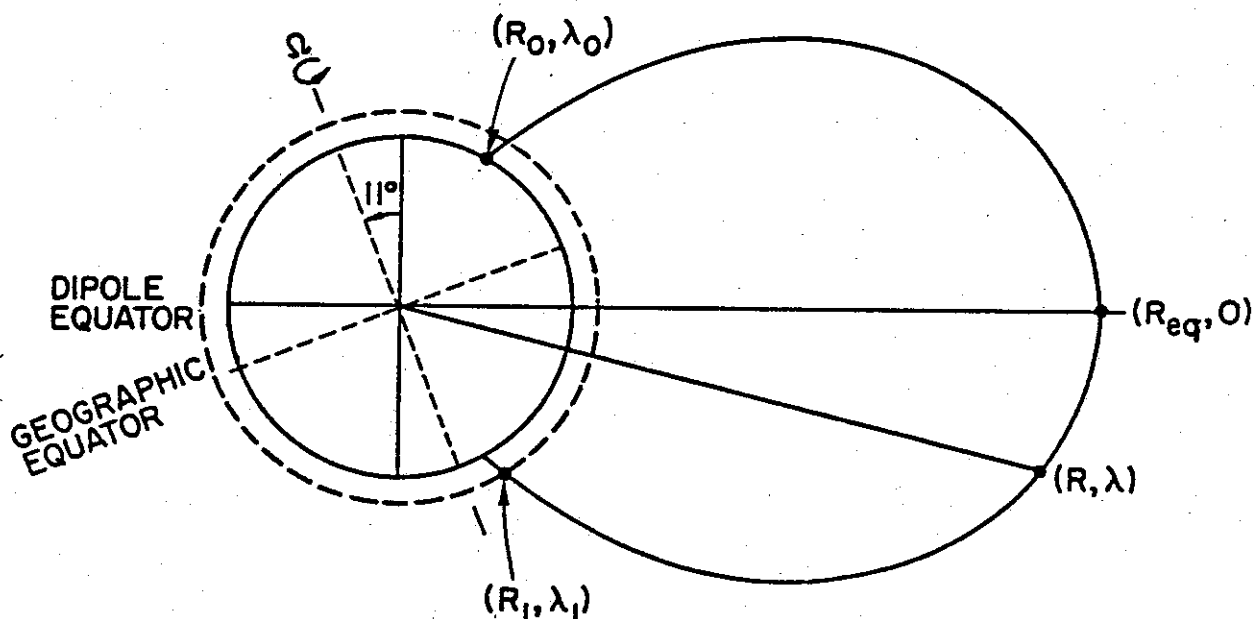


FIGURE 2.1 COORDINATE SYSTEM FOR THE DIPOLE FIELD GEOMETRY.

the early 1960's [Carpenter, 1963, 1966]. At the plasmapause the electron density often drops suddenly by roughly two orders of magnitude within a couple of tenths of an earth radius. The location of the plasmapause can vary from $L=3$ to $L=7$, depending on magnetic activities, but is often near $L=4 \sim 5$ during geomagnetic quiet conditions. The region inside the plasmapause is called the plasmasphere [Carpenter and Park, 1973].

The distribution of the cold plasma within the plasmapause is often modeled as a neutral isothermal mixture of electrons and positive ions (H^+ with some He^+ and O^+) in diffusive equilibrium along the geomagnetic field lines under the influence of the earth's gravitational and centrifugal forces [Angerami and Thomas, 1964]. The cold plasma densities around the geomagnetic equator at the inner edge of the plasmapause are typically in the range of from ~ 300 to ~ 1000 particles/cm³ [Park et al., 1978]. Outside the plasmapause, where the electron densities are quite low, the cold plasma distribution is better approximated by a collisionless model [Angerami, 1966]. The collisionless model can be very closely approximated by the R^{-4} model, in which the electron density is proportional to R^{-4} , R being radial distance [Park, 1972]. In so far as the modeling of interactions with field-aligned propagating waves

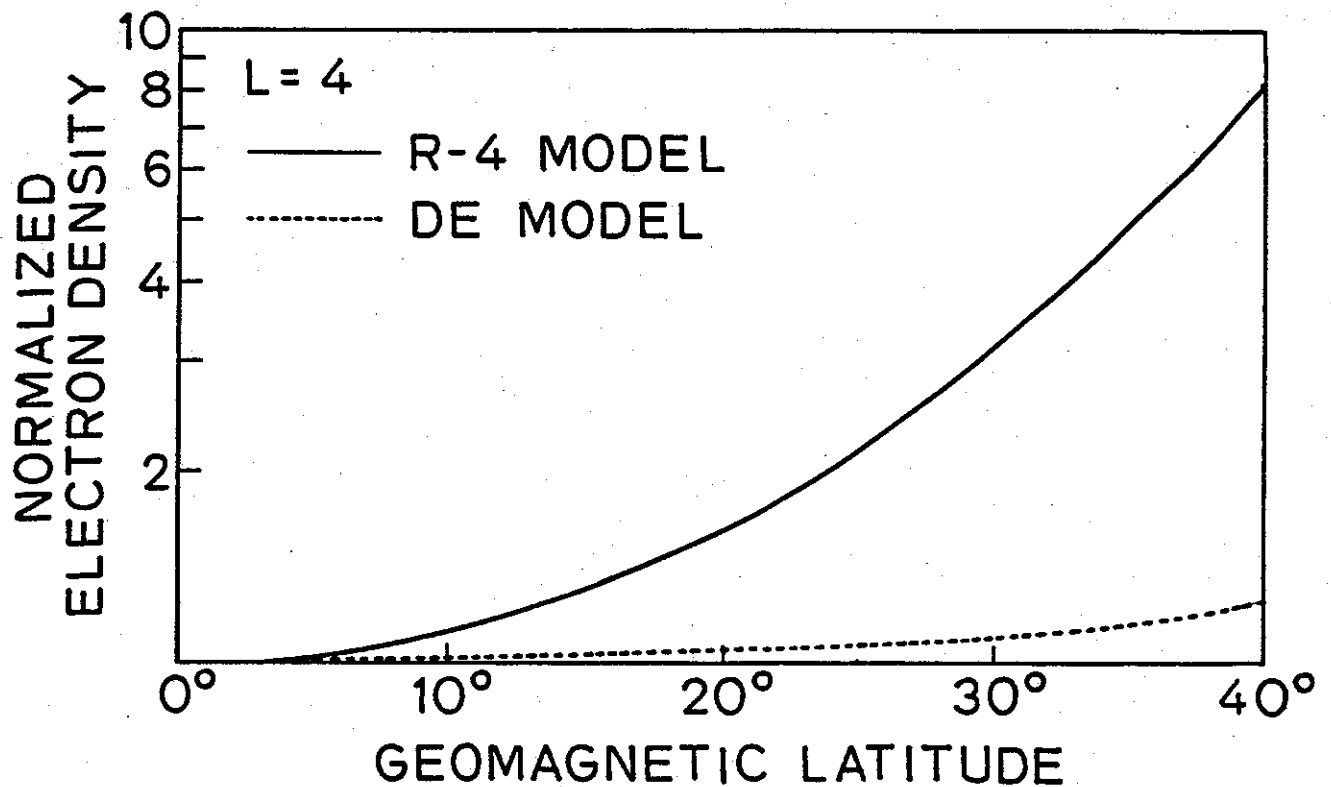


FIGURE 2.2 NORMALIZED ELECTRON DENSITY VERSUS GEOMAGNETIC LATITUDE AT $L=4$ FOR DIFFUSIVE EQUILIBRIUM AND COLLISIONLESS MODELS. The electron density is normalized to the equatorial value.

is concerned, the collisionless model differs from the diffusive equilibrium model in that its electron density varies much faster, particularly near the equator. Figure 2.2 shows the variation of the cold plasma density with geomagnetic latitude along the $L=4$ field line for the diffusive equilibrium (DE) and R-4 models.

B. VLF WHISTLER MODE WAVES IN THE MAGNETOSPHERE

As a magnetoplasma, the magnetosphere can support a variety of waves of frequencies from less than one Hz up to one MHz. In non-magnetized isotropic plasma, there exists a stop band for propagating waves below the electron plasma frequency defined by

$$\omega_P = \sqrt{\frac{n_c e^2}{m \epsilon_0}} \quad (2.5)$$

with n_c being the cold plasma density and ϵ_0 being the permittivity of free space. However, in the presence of a static magnetic field, there exists among others a lower frequency pass band below the electron gyrofrequency ω_H . The earth's magnetic field then 'opens' the magnetosphere to low frequencies. Propagation in this band is referred to as the 'whistler mode' [Helliwell, 1965].

For frequencies in the whistler mode range (i.e., $\omega < \omega_H$), the magnetosphere is a highly dispersive and anisotropic medium. In other words, the refractive index, and therefore the phase and group velocities, depend strongly on the angle between the wave normal \mathbf{k} and the static magnetic field \mathbf{B}_0 . These properties can be explained with the aid of the magneto-ionic theory, described in detail by Ratcliffe [1959]. In this theory it is assumed that the medium is homogeneous. The magnetosphere is an inhomogeneous medium in which the parameters of the medium vary in space. However, for whistler mode waves these parameters are believed to vary sufficiently slowly in the space of one wavelength that the WKB approximation [Budden, 1961] can be used. The whistler mode is in general elliptically polarized. For propagation parallel to \mathbf{B}_0 , the wave polarization is circular with the sense of rotation being the same as that of the electrons.

The whistler mode waves propagating in the inner magnetosphere generally have frequencies from a few tens of Hz up to the electron gyrofrequency ($\sim \leq 1$ MHz), which includes the VLF band. These waves can be generally classified as ducted and nonducted. 'Ducted' waves are believed to propagate in tube-like field-aligned electron density enhancements called 'ducts', which are thought to terminate above the F layer of the ionosphere [Bernhardt and Park, 1977]. The ducts can trap whistler mode waves and confine the wave normals to small angles from the static magnetic field [Smith, 1961]. These waves can penetrate the lower ionosphere in the conjugate hemisphere. Most VLF signals propagating through the magnetosphere and received on the ground are believed to be in this ducted mode. Trapping in an enhancement duct is possible only for wave frequencies less than half the local gyrofrequency [Helliwell, 1965].

Only a small part of the inner magnetosphere is thought to be occupied by ducts. Most of the whistler mode signals travel in the nonducted mode in which the propagation of wave does not generally follow the magnetic field lines. Nonducted waves are not generally received on the ground, although they have been seen on various satellites [Edgar, 1972; Bell et al., 1981; Inan and Helliwell, 1982 and references therein]. Most features of ducted and nonducted wave propagation are well explained by cold plasma theory.

In this report we consider wave-particle interactions involving longitudinally propagating waves so that the wave number vector \mathbf{k} is parallel to the static magnetic field \mathbf{B}_0 . This is a reasonably good approximation to the whistler mode wave propagation within a duct [Smith, 1961]. For this case, the whistler mode refractive index in a cold magnetoplasma is given by

$$\mu(z) = \left[1 + \frac{\omega_P(z)^2}{\omega(\omega_H(z) - \omega)} \right]^{1/2}, \quad (2.6)$$

where ω is the angular wave frequency, z is the coordinate along \mathbf{B}_0 , and $\omega_P(z)$ and $\omega_H(z)$ are local plasma frequency and gyrofrequency, respectively. Within the inner magnetosphere, ω_P^2 is appreciably greater than ω_H^2 and the 1 on the right of (2.6) can often be dropped since $\omega < \omega_H$.

Using the WKB approximation, the wave magnetic field intensity vector of a circularly polarized monochromatic whistler mode signal propagating longitudinally along \mathbf{B}_0 in the slowly varying magnetospheric medium can be expressed as

$$\mathbf{B}_w(z, t) = B_w(z) \left[\mathbf{a}_x \cos\left(\omega t - \int_0^z k(z) dz\right) + \mathbf{a}_y \sin\left(\omega t - \int_0^z k(z) dz\right) \right], \quad (2.7)$$

where $B_w(z)$ is the magnitude of $\mathbf{B}_w(z, t)$ and is slowly varying according to the square root of the local refractive index, $k(z)$ is the wave number and \mathbf{a}_x and \mathbf{a}_y are the unit vectors in the x and y directions, respectively. The wave number $k(z)$ is equal to $\mu(z)\omega/c$, c being the speed of light. (2.7) indicates that the wave is right hand polarized.

The wave magnetic field intensity changes due to the changing refractive index. Also for ducted wave propagation considered here, the cross-sectional area of the duct varies along the field line, being inversely proportional to the static magnetic field intensity B_0 . The intensity of a ducted VLF wave will also vary as the duct cross section changes if the whistler mode wave is assumed to be the superposition of a large number of rays that fill the duct. Including both of these effects, the amplitude $B_w(z)$ of the wave magnetic field can be expressed as

$$B_w(z) = B_{weq}(\omega_H(z)k(z)/\omega_{Heq}k_{eq})^{1/2}, \quad (2.8)$$

where B_{weq} , ω_{Heq} , and k_{eq} are equatorial values. Equivalently, we assume that the total power flow of the wave in the duct is constant. Since B_w , ω_P , ω_H , and k are

all slowly varying quantities, in the rest of this report we drop (z) for the sake of convenience.

From (2.6) and the definition of the group refractive index $\mu' = d(\mu\omega)/d\omega$, we find the phase velocity v_p and group velocity v_g for longitudinal propagation are given respectively by

$$v_p = \frac{c}{\mu} = c \frac{\omega^{1/2}(\omega_H - \omega)^{1/2}}{\omega_P}, \quad (2.9)$$

$$v_g = \frac{c}{\mu'} = 2c \frac{\omega^{1/2}(\omega_H - \omega)^{3/2}}{\omega_P \omega_H}. \quad (2.10)$$

In a slowly varying medium, v_p and v_g are both functions of position z .

C. DYNAMICS OF TRAPPED RADIATION BELT PARTICLES

In addition to the particles which constitute the magnetospheric cold plasma and support the propagation of the whistler mode waves as discussed above, a relatively small number of particles of higher kinetic energies, extending up to hundreds of MeV, are also present in the magnetosphere. These energetic particles, mainly electrons and protons, constitute the earth's radiation belts and are magnetically trapped in the static magnetic field [Roederer, 1970].

A charged particle in a uniform magnetic field executes a helical motion. This motion is a combination of circular motion around a field line and linear motion along the field line. In the case of slowly varying magnetic field in space and time, the motion can still be described as composed of a near-circular motion around a field line and a linear motion along a field line. This helical motion is generally accompanied by an additional drift across field lines [Hess, 1968].

In the earth's dipole magnetic field a charged particle performs a motion that can be broken down into three components. It rotates rapidly around a field line, bounces back and forth between its two mirror points along a line, and slowly drifts in longitude around the earth. The speed of these three motions are so different that they can be separately treated [Hess, 1968].

We denote the parallel and perpendicular components to the field line of the particle velocity \mathbf{v} by v_{\parallel} and v_{\perp} , respectively. By definition the relation between the total momentum \mathbf{p} and the total velocity \mathbf{v} is given as

$$\mathbf{p} = M\gamma\mathbf{v}, \quad (2.11)$$

where M is the rest mass of the particle and $\gamma=(1-v^2/c^2)^{-1/2}$ is the relativistic factor. The parallel and perpendicular components of \mathbf{p} are represented by p_{\parallel} and p_{\perp} , respectively. The angle between the field line and \mathbf{v} or \mathbf{p} , i.e., the pitch angle, is given by $\alpha=\tan^{-1}(v_{\perp}/v_{\parallel})=\tan^{-1}(p_{\perp}/p_{\parallel})$. The kinetic energy (referred to as energy henceforth in this report) of the particle is

$$E = Mc^2(\gamma - 1),$$

where Mc^2 is the rest energy of the particle, being 511 keV for electrons.

Electrons and protons gyrate in opposite directions around a field line. The gyrofrequency ω_{H_M} and the radius of rotation R_{H_M} for a particle of rest mass M are given by

$$\begin{aligned}\omega_{H_M} &= \frac{qB_0}{M\gamma}, \\ R_{H_M} &= \frac{M\gamma v_{\perp}}{qB_0} = \frac{M\gamma v \sin \alpha}{qB_0} = \frac{p \sin \alpha}{qB_0},\end{aligned}\tag{2.12}$$

where q is the charge of the particle and B_0 is the local magnetic field.

The magnetic force $\mathbf{v} \times B_0$ on the particles changes the direction of the particle momentum without doing work on the particle. The total energy of the particle is therefore conserved along its trajectory. It can be shown (e.g., *Alfvén and Fälthammar, 1963*) that when the change in the magnetic field during one gyro period is small enough, the quantity p_{\perp}^2/B_0 is constant to the first order. It is thus an 'adiabatic invariant', meaning that its variation due to a given change in B_0 can be made *arbitrarily* small by letting the change in B_0 take place *sufficiently slowly* in space and time. This approximation is well satisfied in the inner magnetosphere. Using the conservation of energy, i.e., $p=\text{constant}$, and $p_{\perp}^2/B_0=\text{constant}$, we have

$$\frac{\sin^2 \alpha}{B_0} = \text{constant}.\tag{2.13}$$

According to (2.13), the particle pitch angle α increases as B_0 increases along the particle's trajectory. When B_0 is large enough such that the local $\alpha=90^\circ$ (i.e., $p_{\parallel}=0$), the particle is said to have mirrored back and spirals back up the field line. The point at which this turn-around occurs is called the 'mirror point'. Figure 2.3 shows a particle trajectory along the earth's dipole field line. There are two mirror points near the conjugate ends of the field line. The particle is 'trapped' in the sense

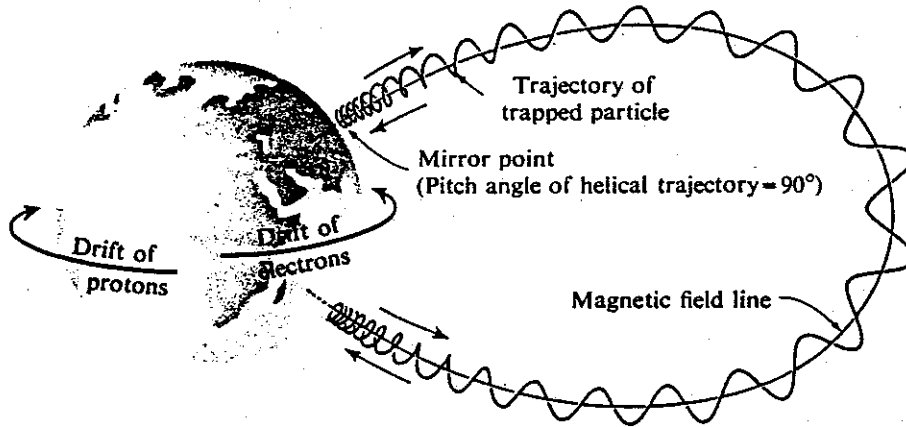


FIGURE 2.3 TRAJECTORY OF AN ENERGETIC PARTICLE IN THE EARTH'S DIPOLE FIELD. The motion is composed of three components: (1) spiraling along field lines, (2) bouncing back and forth between mirror points along field lines, and (3) drifting slowly in longitude around the earth. The electrons drift east and the protons drift west. (From Hess [1968].)

that it spirals back and forth between the conjugate mirror points. The position of the mirror point depends on the equatorial pitch angle α_{eq} of the particle. From (2.13) α_{eq} associated with a mirror point of field strength B_m is given by

$$\sin^2 \alpha_{eq} = \frac{B_{eq}}{B_m}, \quad (2.14)$$

where B_{eq} is the equatorial magnetic field. The particle travel time from one mirror point to the other and back again is known as the 'bounce period'. In the inner magnetosphere the typical bounce periods for particles trapped in the radiation belts range from a fraction of a second to a few seconds [Liemohn, 1961].

In addition to the gyro and bounce motions a charged particle in the magnetosphere undergoes a drift motion across the magnetic field lines. The direction of drift motion is perpendicular to the static magnetic field and may be in either the azimuthal or the radial direction. The azimuthal motion is caused by the gradient ∇B_0 of the earth's dipole field which causes electrons to drift eastward and protons to drift westward, as indicated in Figure 2.3 [Hess, 1968]. The drift periods generally range from minutes to days and are much greater than the gyro and bounce periods. The radial motion is mainly $\mathbf{E} \times \mathbf{B}$ drift caused by azimuthal

electric fields [Carpenter and Seely, 1976] and is usually slower than the azimuthal motion. The dynamics of charged particles in a dipole field including cross field drifts are discussed in details by Hess [1968] and Roederer [1970].

In this report we focus our attention on the phenomenon of 'precipitation' of trapped energetic particles out of the magnetosphere. From the discussion in connection with (2.14) it can be seen that particles with smaller equatorial pitch angles have lower mirror heights. If the mirror point is located in the denser regions of the lower ionosphere, the particle collides with the atmospheric constituents and may be absorbed. Such a particle is said to be 'precipitated' out of the radiation belts since it does not travel back up the field line, but is deposited in the ionosphere.

It can be shown that the equatorial pitch angle of a particle gyrating around a dipole field line on L -shell with a mirror height of h_m is given by [Inan, 1977]

$$\sin \alpha_{eq} = \left[\frac{H_m^3}{L^2 \sqrt{4L^2 - 3H_m L}} \right]^{1/2}, \quad (2.15)$$

where $H_m = (R_0 + h_m)/R_0$. Corresponding to a given mirror height h_m , an equatorial 'loss cone' can be defined using the associated α_{eq} in (2.15) as its half angle. This half angle is denoted as α_{eq}^{lc} and is known as the equatorial loss cone angle. The atmospheric altitudes where a significant number of particles are removed from the trapped population are generally about 100 ~ 300 km [Berger et al., 1974]. The loss cone angle defined by (2.15) does not significantly depend on h_m in this range. For our purposes we choose to define the equatorial loss cone angle (α_{eq}^{lc}) as the equatorial pitch angle associated with an $h_m = 100$ km and we assume that any particle with h_m smaller than 100 km (i.e., $\alpha_{eq} < \alpha_{eq}^{lc}$) is precipitated.

Although in the content of the ideal dipole model we consider the mirror heights in the two conjugate hemispheres for a given α_{eq} to be the same, for the earth's magnetic field significant asymmetries along some field lines do exist [Barish and Wiley, 1970]. In such cases the loss cone corresponding to one hemisphere is different from that corresponding to the conjugate hemisphere.

One of the major processes for precipitating trapped particles out of the radiation belts is the 'scattering' of particles during wave-particle interactions in the magnetosphere. 'Scattering' in this context refers to the particles' pitch angles being altered from their adiabatic values as a result of wave-induced perturbations. The particle may thus be lost to the atmosphere if its α_{eq} is lowered below α_{eq}^{lc} .

during either one or more encounters with a given wave. Specifically, in this report we study such precipitation of energetic electrons induced by cyclotron resonant wave-particle interactions involving coherent whistler mode waves.

D. CYCLOTRON RESONANT WAVE-PARTICLE INTERACTIONS

We now discuss the equations of motion of an energetic electron in a longitudinally propagating whistler mode wave. As will be discussed later, for an electron to interact with the wave in the cyclotron resonance sense, it must travel in a direction opposite to that of the wave, as shown in Figure 2.4.

In the absence of the wave the electrons are adiabatically trapped in the earth's magnetic field. Using the first adiabatic invariant (i.e., $p_{\perp}^2/B_0 = \text{constant}$) their motion, neglecting the small longitudinal drift across the field line, can be described by the following equations

$$\begin{aligned}\frac{dp_{\parallel}}{dt} &= -\frac{p_{\perp}^2}{2B_0 m \gamma} \frac{\partial B_0}{\partial z} \\ \frac{dp_{\perp}}{dt} &= +\frac{p_{\perp} p_{\parallel}}{2B_0 m \gamma} \frac{\partial B_0}{\partial z},\end{aligned}\quad (2.16)$$

where the coordinate system and the variables are defined in Figure 2.4. From the Lorentz force equation and Newton's second law, the wave-induced acceleration of the particle can be described in the laboratory frame as

$$\begin{aligned}\left(\frac{dp_{\parallel}}{dt}\right)_{\text{wave}} &= \frac{eB_w}{m\gamma} p_{\perp} \sin \phi \\ \left(\frac{dp_{\perp}}{dt}\right)_{\text{wave}} &= -eE_w \sin \phi - \frac{eB_w}{m\gamma} p_{\parallel} \sin \phi,\end{aligned}\quad (2.17)$$

where ϕ is the angle between the electron's perpendicular momentum vector \mathbf{p}_{\perp} and $-\mathbf{B}_w$, and E_w is the wave electric field intensity. Note that for plane wave as is assumed here, $E_w = (\omega/k)B_w$. Superimposing the adiabatic motion of the electrons as given by (2.16) on the wave-induced perturbations, we obtain the complete equations of motion for the cyclotron resonance wave-particle interaction with electrons:

$$\frac{dp_{\parallel}}{dt} = \frac{eB_w}{m\gamma} p_{\perp} \sin \phi - \frac{p_{\perp}^2}{2\omega_H m \gamma} \frac{\partial \omega_H}{\partial z} \quad (2.18a)$$

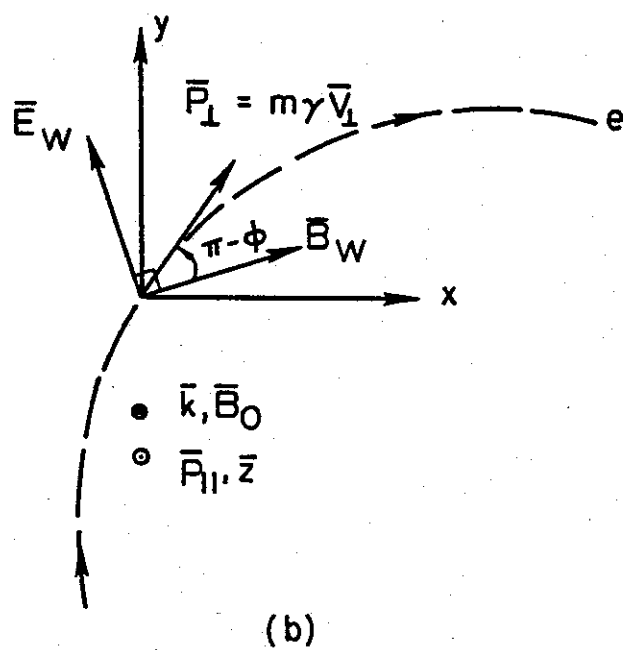
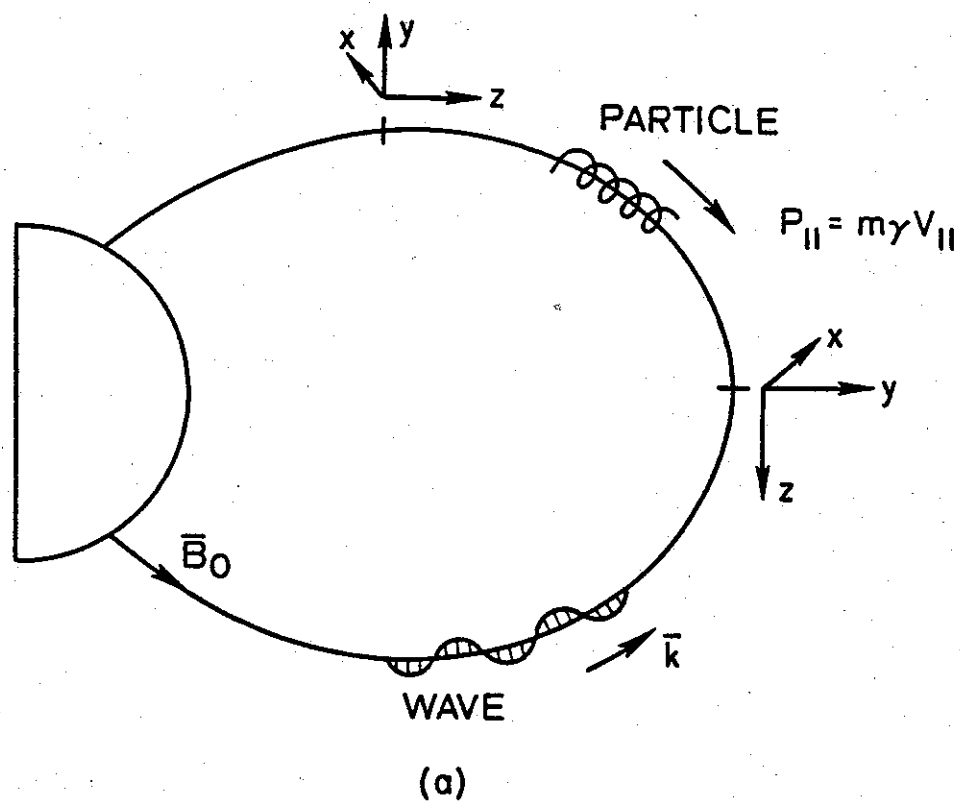


FIGURE 2.4 COORDINATE SYSTEM FOR THE EQUATIONS OF MOTION. The particle and the wave are traveling in opposite directions. The z axis is everywhere aligned with the magnetic field line. Dashed line indicates the orbit of the electrons in the x - y plane.

$$\frac{dp_{\perp}}{dt} = -\frac{eB_w}{m\gamma}(p_{\parallel} + \frac{\omega}{k}m\gamma)\sin\phi + \frac{p_{\perp}p_{\parallel}}{2\omega_H m\gamma} \frac{\partial\omega_H}{\partial z}, \quad (2.18b)$$

where $\omega_H \equiv eB_0/m$ has been used. Also the rate of change of ϕ , which controls the cumulative change in p_{\parallel} and p_{\perp} , is given by

$$\frac{d\phi}{dt} = \frac{\omega_H}{\gamma} - \omega - k \frac{p_{\parallel}}{m\gamma} - \frac{eB_w}{m\gamma}(p_{\parallel} + \frac{\omega}{k}m\gamma) \frac{\cos\phi}{p_{\perp}}. \quad (2.18c)$$

Equations (2.18) are written in the laboratory frame, with the coordinate system as shown in Figure 2.4. The quantities ω_H and k are functions of z , the coordinate along the field line.

Although (2.18) describes the particle momentum, the velocity components can be obtained from (2.11) with γ given by

$$\gamma = \sqrt{p^2 c^2 + m^2 c^4} / mc^2. \quad (2.19)$$

Note that (2.18) are the general form of the equations of motion valid also for relativistic energies. For the nonrelativistic case, $\gamma=1$, and (2.18) reduces to the nonrelativistic equations of motion which are often written in terms of velocity components:

$$\frac{dv_{\parallel}}{dt} = \frac{eB_w}{m} v_{\perp} \sin\phi - \frac{v_{\perp}^2}{2\omega_H} \frac{\partial\omega_H}{\partial z} \quad (2.20a)$$

$$\frac{dv_{\perp}}{dt} = -\frac{eB_w}{m}(v_{\parallel} + \frac{\omega}{k})\sin\phi + \frac{v_{\perp}v_{\parallel}}{2\omega_H} \frac{\partial\omega_H}{\partial z} \quad (2.20b)$$

$$\frac{d\phi}{dt} = \omega_H - \omega - kv_{\parallel} - \frac{eB_w}{m}(v_{\parallel} + \frac{\omega}{k}) \frac{\cos\phi}{v_{\perp}}. \quad (2.20c)$$

Equations (2.20) in whole or in part have been used to study VLF wave-particle interactions by many authors [Dysthe, 1971; Inan et al., 1978 and references therein]. It has been suggested [Chang and Inan, 1983] that the exact equations (2.18) be used for particle energies higher than 50 keV, corresponding to a 10% correction in average pitch angle scattering with respect to the nonrelativistic formulation.

Cyclotron Resonance Condition

Since the first terms on the right hand side in (2.18a) and (2.18b) are proportional to $\sin\phi$, cumulative changes in p_{\parallel} and p_{\perp} will only result when $\phi \rightarrow 0$. For most magnetospheric parameters, the last term on the right hand side in (2.18c) is

negligible unless $v_{\perp} \rightarrow 0$ [Inan, 1977]. Neglecting this term, (2.18c) can be rewritten as

$$\frac{d\phi}{dt} = k \left[\frac{\omega_H/\gamma - \omega}{k} - v_{\parallel} \right] = k(v_R - v_{\parallel}), \quad (2.21)$$

where $v_R = (\omega_H/\gamma - \omega)/k$ is commonly designated as the 'cyclotron resonance velocity'. From (2.18a), (2.18b), and (2.21) it is clear that the wave-induced perturbations in the particle trajectory are negligible unless the following condition holds between the wave and the electron:

$$v_{\parallel} \simeq v_R = (\frac{\omega_H}{\gamma} - \omega)/k$$

$$\text{or } \omega + kv_{\parallel} \simeq \omega_H/\gamma. \quad (2.22)$$

Equation (2.22) is known as the (fundamental) relativistic cyclotron resonance condition and represents the case when the Doppler shifted wave frequency experienced by the electron is approximately equal to the gyrofrequency of the electron as observed in the laboratory frame. Note that $\gamma = (1 - v_{\parallel}^2/c^2 \cos^2 \alpha)^{-1/2}$, where α is the pitch angle of the resonant electron. The parameter γ accounts for the heavier mass and reduced gyrofrequency of the electron in the relativistic sense. When $\gamma=1$, (2.22) reduces to

$$\omega + kv_{\parallel} \simeq \omega_H, \quad (2.23)$$

which is the nonrelativistic cyclotron resonance condition and is often used in the literature for the study of lower resonant energies (e.g., $E < 10$ keV).

The wave vectors seen by an electron that is in cyclotron resonance with a whistler mode wave are approximately stationary. When the resonance lasts (i.e., (2.22) is satisfied) for a significant length of time, cumulative energy and/or momentum changes of the electron can occur.

Given local values of ω_H , k , and ω , there always exists a positive solution for v_{\parallel} of (2.22) for any specified value of the local pitch angle α , given by

$$v_{\parallel} \simeq v_R = \frac{-\omega k + [\omega^2 k^2 + (\omega_H^2 - \omega^2)(k^2 + \omega_H^2/c^2 \cos^2 \alpha)]^{1/2}}{k^2 + \omega_H^2/c^2 \cos^2 \alpha}. \quad (2.24)$$

It can be shown that for $\mu \cos \alpha > 1$, where μ is the refractive index, the above solution is the only one which satisfies (2.22). However, for $\mu \cos \alpha < 1$, there exist two

solutions: one is positive and is given by (2.24), the other is negative and corresponds to $\gamma > \omega_H/\omega$. Negative v_{\parallel} represents electrons traveling in the same direction as the wave. For typical magnetospheric parameters, $\mu \cos \alpha < 1$ requires a very high pitch angle. For example, for $\mu=10$, α should at least be 84.3° . In this report we shall consider only electrons with v_{\parallel} as described by (2.22). In this case, $\omega < \omega_H/\gamma$, and the resonant electrons and the wave travel in opposite directions.

Unlike the nonrelativistic case (2.23), the cyclotron resonant parallel velocity for relativistic electrons is a function of pitch angle α . Figure 2.5 shows the equatorial resonance velocity as a function of α for different values of $\Lambda = \omega/\omega_{Heq}$ for interactions at the geomagnetic equator at $L=2$, with $f_{Heq} = \omega_{Heq}/2\pi = 109.2$ kHz, and for cold plasma density of 800 el/cm^3 . The resonance velocity is higher at lower pitch angle and decreases with increasing α . At lower frequencies the decrease is much faster since the total velocity of the electron cannot exceed the speed of light. It is observed from (2.22) that γ approaches ω_H/ω as v_{\parallel} approaches zero or α approaches 90° . Therefore, the asymptotic behavior of the resonance velocity near 90° pitch angle is given by

$$v_R \rightarrow c \sqrt{1 - \omega^2/\omega_H^2} \cos \alpha \quad \alpha \rightarrow 90^\circ.$$

Figure 2.6 shows the energy of the resonant electrons as a function of the pitch angle for the corresponding cases in Figure 2.5. Since γ approaches ω_H/ω , the energy at resonance approaches $mc^2(\omega_H/\omega - 1)$ as α approaches 90° .

For resonant interactions in the inner radiation belt and for cases when the cold plasma density and/or the wave frequency is low, e.g., propagation outside the plasmopause, the energies of the resonant electrons are in the quasi-relativistic range (energies in the range of several tens up to several hundreds of keV). Figure 2.7 shows the equatorial resonance energy as a function of the equatorial cold plasma density for different frequencies at $L=5$ and for $\alpha=3.87^\circ$, the half width of the equatorial loss cone at $L=5$. This particular value of α is chosen since in the rest of this report we study the wave-induced scattering and precipitation of near-loss-cone electrons. Note for example that for $n_{eq} < 20 \text{ el/cm}^3$, typical of the region outside the plasmopause, waves with frequency less than 700 Hz can interact with electrons of energy higher than 100 keV.

Method of Study

Since the equations of motion (2.18) are highly nonlinear, it is generally difficult to solve them using analytical methods. For our study, we employ a test particle

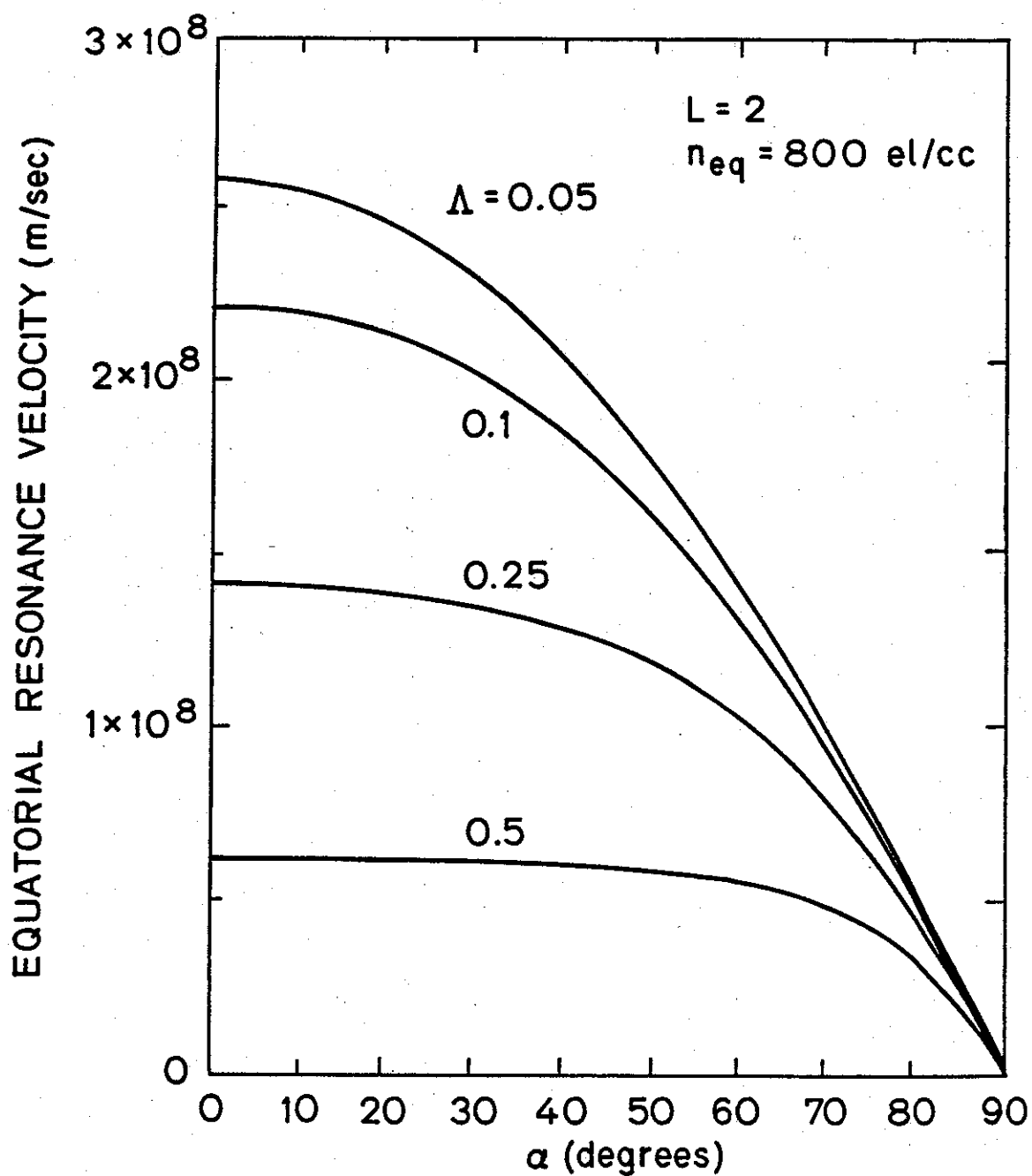


FIGURE 2.5 EQUATORIAL RESONANCE VELOCITY VS. EQUATORIAL PITCH ANGLE FOR DIFFERENT NORMALIZED FREQUENCIES $\Lambda = \omega / \omega_{Heq}$. The result shown is for $L=2$ and $n_{eq}=800$ el/cm³.

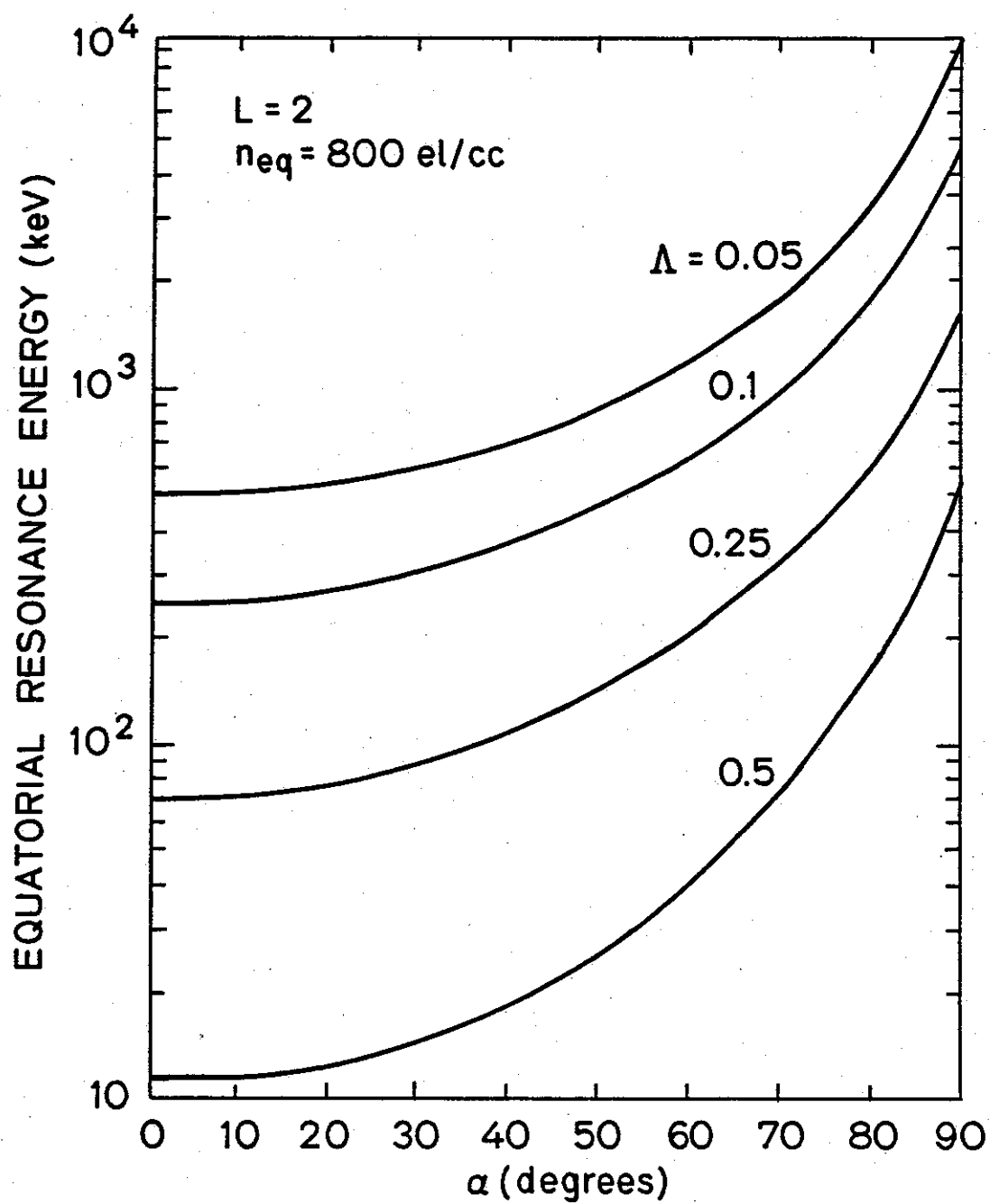


FIGURE 2.6 EQUATORIAL RESONANCE ENERGY VERSUS EQUATORIAL PITCH ANGLE FOR THE SAME PARAMETERS AS IN FIGURE 2.5.

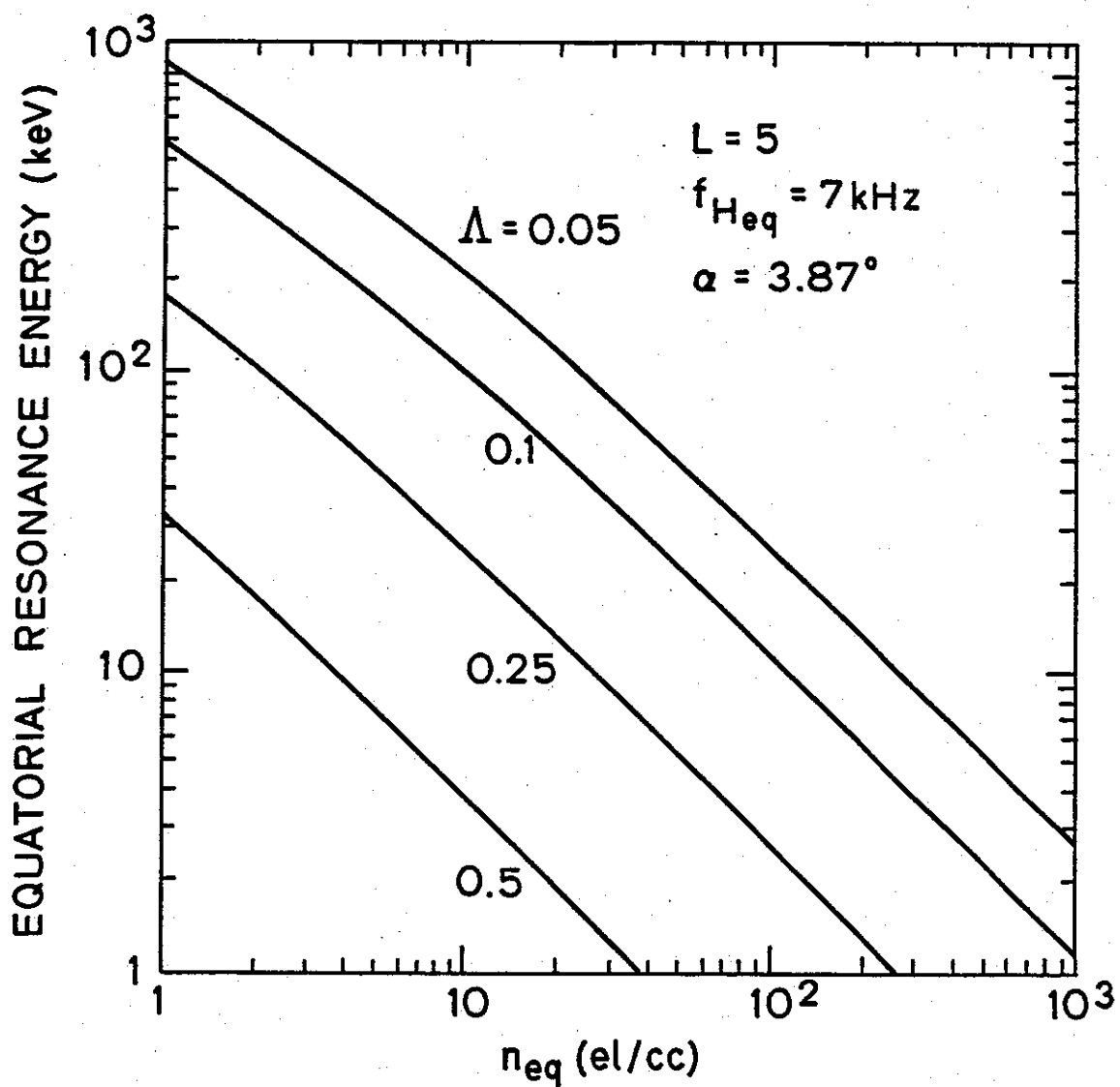


FIGURE 2.7 EQUATORIAL RESONANCE ENERGY VERSUS EQUATORIAL COLD PLASMA DENSITY FOR DIFFERENT NORMALIZED FREQUENCIES Λ . The result shown is for $L=5$ with an equatorial gyrofrequency of 7 kHz and a half angle of the equatorial loss cone of 3.78° .

simulation method for computing the individual particle trajectories. This method is similar to and is an extension of the one used by *Inan* [1977] and *Inan et al.* [1978]. The method of solution is described in details in the above references. Basically it employs a centered dipole model for the static magnetic field and a diffusive equilibrium model or a collisionless model for the background cold plasma. Then by integrating the full equations of motion (2.20), the effect of the wave on individual test particles, i.e., deviation from their adiabatic trajectories, can be obtained. By considering a sufficient number of test particles that are appropriately distributed in ϕ , v_{\parallel} , and v_{\perp} , the wave-induced perturbation of the full particle distribution is inferred.

For our particular application we have employed the relativistic equations of motion (2.18) and the relativistic cyclotron resonance condition (2.22) and have thus extended the computer model to relativistic energies. The equations of motion (2.18) written in terms of the particle momentum components instead of velocity components are utilized. The velocity space trajectories followed by particles at various pitch angles during cyclotron resonance interactions under various magnetospheric conditions has been described in detail by *Inan* [1977]. The importance of phase trapping of particles in the wave's potential well was emphasized. In this report we are particularly interested in the wave-induced perturbation of the near-loss-cone particles and their contribution to the particle precipitation. In the next section we give some examples of the cyclotron resonant scattering of near-loss-cone quasi-relativistic particles by monochromatic VLF waves.

E. SCATTERING OF NEAR-LOSS-CONE PARTICLES

In this section we shall determine the efficiency of scattering of the near-loss-cone quasi-relativistic particles by moderate intensity VLF waves. In this context, 'near-loss-cone' represents the particles with pitch angles very close to the edge of the bounce loss cone. We consider the case of $L=2$, representing the outer boundary of the inner radiation belt, and an equatorial cold plasma electron density of 800 el/cm³. For a dipole model of the static magnetic field line the equatorial half angle of the loss cone corresponding to a mirror altitude at 100 km is found to be $\alpha_{eq}=16.77^{\circ}$. We consider a monochromatic wave at $f=5.46$ kHz $=0.05 f_{Heq}$, where f_{Heq} is the equatorial gyrofrequency. Its intensity is taken to be $B_w=7.5$ pT so that the wave power density would be the same as a wave at $f=0.5 f_{Heq}$ and $B_w=5$ pT.

Figure 2.8 shows the trajectory of a test particle having an initial Larmor phase (ϕ_0) of 120° and a pitch angle equal to the half angle of the loss cone. The particle

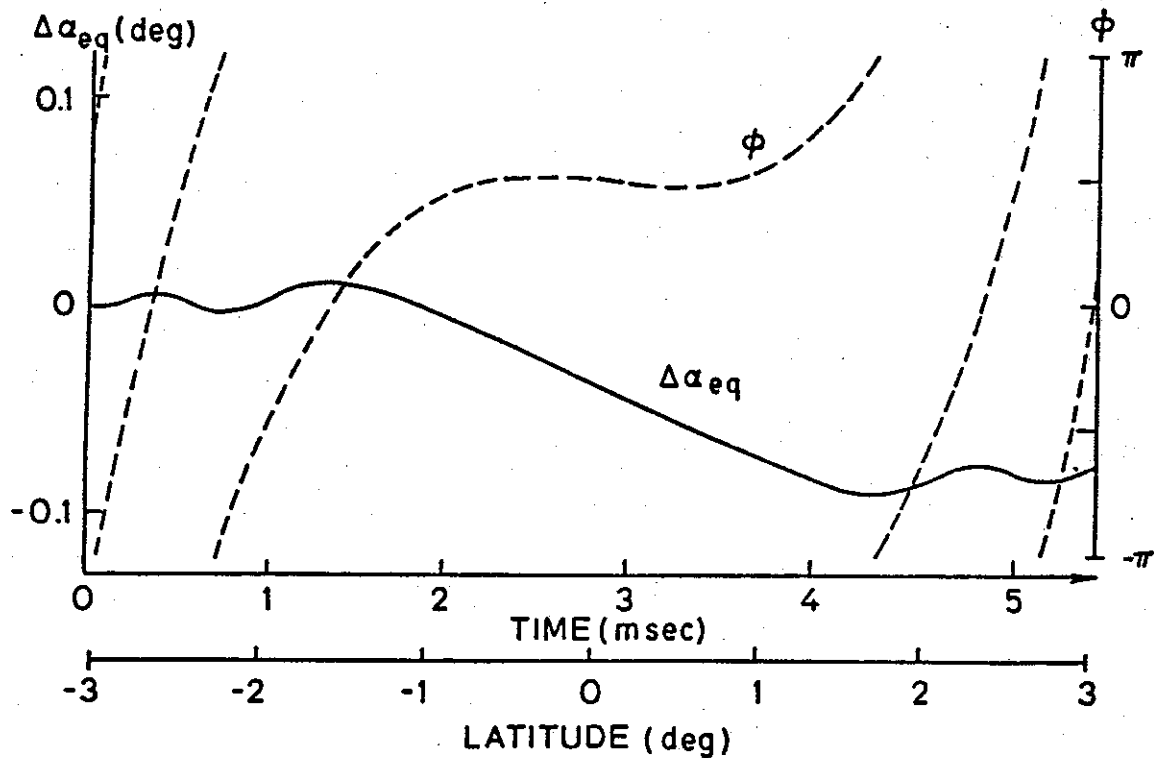


FIGURE 2.8 TRAJECTORY OF A RELATIVISTIC TEST PARTICLE UNDER THE INFLUENCE OF A MONOCHROMATIC WAVE OF 5.46 KHZ HAVING $B_w=7.5$ pT AT $L=2$. Both the total scattering $\Delta\alpha_{eq}$ (solid line) and the phase ϕ (dashed lines) are shown as functions of time. The equations of motion are integrated over the time when the particle parallel velocity is within $\pm 2\%$ of the local resonance velocity. The test particle has an energy of 523 keV and an equatorial pitch angle of 16.77° . The initial Larmor phase was taken to be 120° .

resonates with the wave at the geomagnetic equator and has an initial energy of 523 keV. The equations of motion are integrated over the time when the particle's parallel velocity is within 2% of the local resonance velocity. For the parameter ranges used in this case we have found that the wave-induced perturbations can then be estimated to within an error of 10% at most. It can be seen in this case that the particle's equatorial pitch angle is changed by $\sim 0.9^\circ$ during its resonance encounter with the wave.

Figure 2.9a shows the total scattering $\Delta\alpha_{eq}$ as a function of ϕ_0 for equatorial resonant particles of the same energy and pitch angle. The sinusoidal variation of $\Delta\alpha_{eq}$ with ϕ_0 reveals the linearity of the scattering for the parameters considered,

due mainly to the relatively low L shell, and thus its high inhomogeneity [Inan, 1977]. This is also demonstrated by Figure 2.9b which shows the root mean square (rms) scattering of the same particles as a function of wave intensity. It indicates that the rms scattering is proportional to the wave intensity at least up to 45 pT. It is noticed in Figure 2.8 that for particles with the initial parameters used here, the interaction region, which can be roughly defined as that part of the field line within which the particles go through a 180° phase variation about the resonance point [Helliwell, 1967], is within $\pm 1.6^\circ$ in latitude around the equator. We have computed ρ , which is the ratio of the wave and inhomogeneity terms as defined in Inan *et al.* [1978] for this case and it was found that ρ varies from 0.01 at 0.16° latitude up to only 0.16 at 0.01° latitude. This confirms the linearity property since the ρ values within the interaction region are much smaller than $\rho=1$ which has been defined as a threshold of linearity [Inan *et al.*, 1978].

To demonstrate the efficiency of scattering for particles that resonate with the wave at points off the equator, we plot in Figure 2.10 the rms scattering as a function of the particle energy. For each energy we have considered particles uniformly distributed in initial phase and having the same unperturbed pitch angle, i.e., $\alpha_{eq}^0 = 16.77^\circ$. In general, particles with given initial energy higher than 523 keV resonate with the wave in the vicinity of two points on both sides of the equator. According to the linear theory the total scattering $\Delta\alpha$ due to one resonance depends on the initial phase of the particle and is a sinusoidal function as shown in Figure 2.9a [Inan, 1977]. The quasi-periodic variation of the scattering shown in Figure 2.10 is due to the phasing between these two resonance points. A similar result was obtained by using a linearized solution of the equations of motion [Ashour-Abdalla, 1972]. The decrease in period as particle energy increases in Figure 2.10 is attributed mainly to the faster phase variation experienced by the higher energy particles. Note that the maximum scattering, which is represented by the peak of the main lobe, occurs when the resonance points are located slightly away from the equator and the strength of scattering decreases rapidly for particles with energy below the equatorial resonance energy. This causes the asymmetrical behavior of the scattering with respect to the strongest interaction. On top of Figure 2.10 is shown the latitude of resonance as a function of energy. It indicates that the maximum scattering results from interactions within 2° latitude around the equator in this particular case.

The dashed curve in Figure 2.10 shows the envelope of the rms scattering pattern. This envelope is important since it reveals the relative magnitude of the scattering

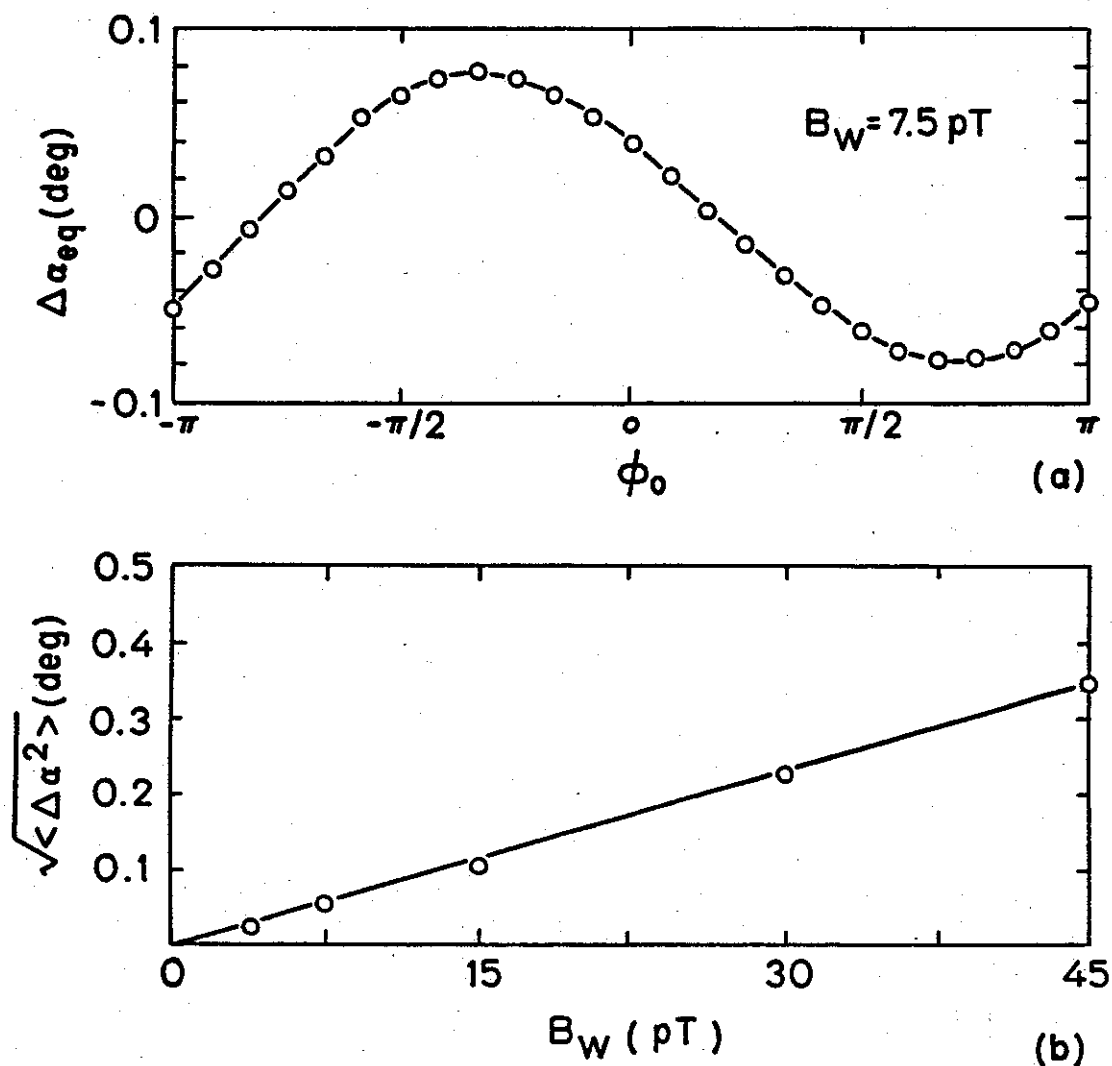


FIGURE 2.9 DEPENDENCE OF PARTICLE SCATTERING ON THE INITIAL LARMOR PHASE AND THE WAVE INTENSITY. (a) Total scattering $\Delta\alpha_{eq}$ versus initial phase ϕ_0 for equatorial resonance particles. All other parameters have the same values as in Figure 2.8. (b) The root mean square (rms) scattering as a function of wave intensity for the same resonant particles in (a).

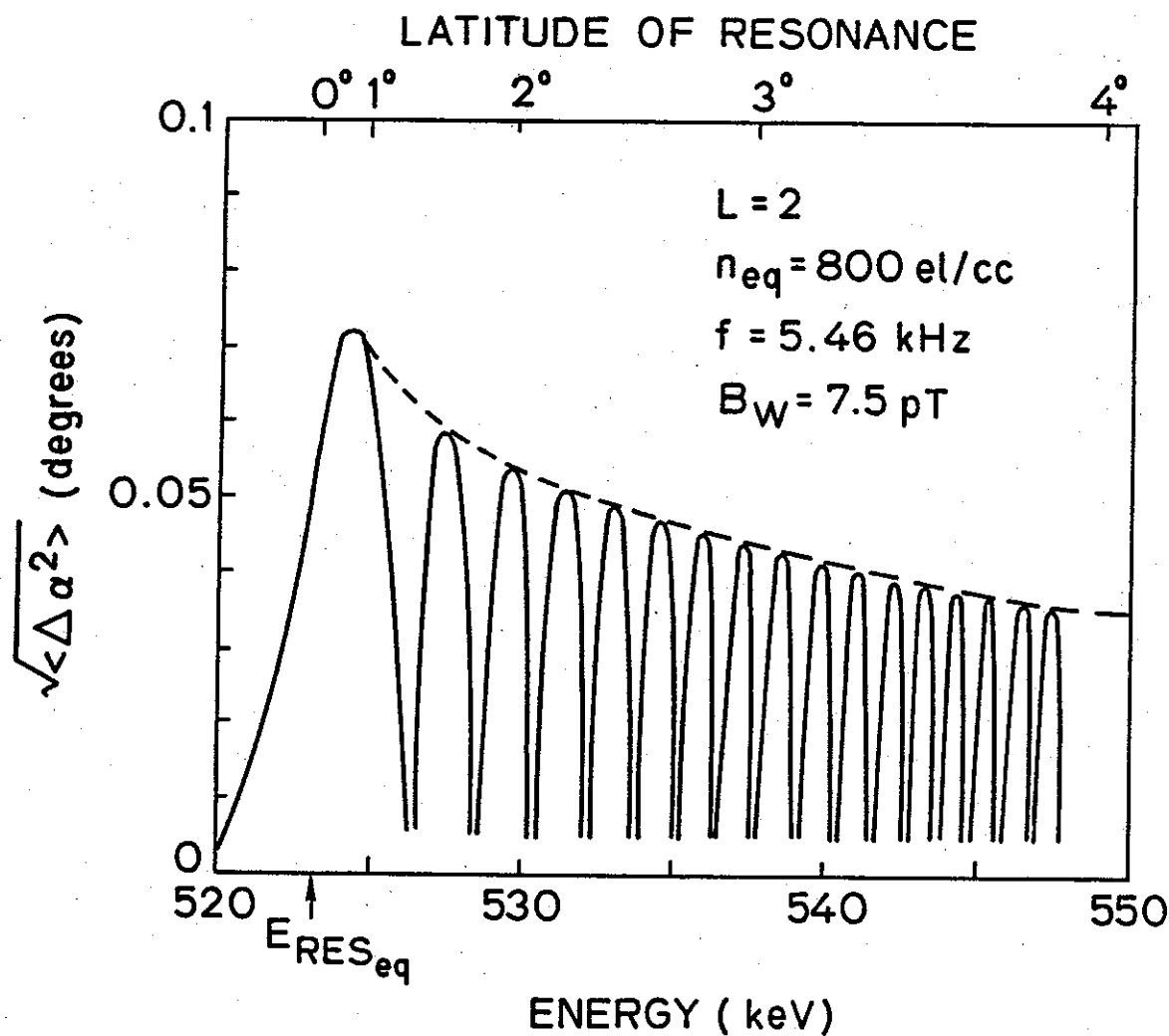


FIGURE 2.10 THE RMS SCATTERING VERSUS THE PARTICLE ENERGY FOR THE SAME MAGNETOPLASMA AND WAVE PARAMETERS AS IN FIGURE 2.8. For each energy, particles uniformly distributed in initial phase and having the same unperturbed pitch angle $\alpha_{eq}^0 = 16.77^\circ$ are considered. The dashed curve shows the envelope of the scattering pattern. Also indicated is the latitude of resonance corresponding to different particle energy.

as a function of the location of the resonance point. In the following discussion we use this envelope for the purpose of comparing the wave-induced pitch angle changes for different cases.

Up to now we have considered a wave structure which is symmetrically distributed on both sides of the equator; the scattering differs if the wave intensity is taken to be zero on the down stream side of the particles. Such a model may represent a wave which has been amplified due to the wave-particle interactions near the equator [Helliwell, 1967]. Since this amplification can typically be 30 db or more [Helliwell and Katsufakis, 1974], we take the wave intensity to be 7.5 pT on the upstream side of the particles and negligibly small on the other side. Figure 2.11 shows the rms scattering of the test particles in the same energy range as in Figure 2.10 due to this half-sided wave structure. The total pitch angle scattering is less than that of the full wave case since the effective interaction length has been halved. Within the interaction region the pitch angle change of a particle, and thus the rms scattering of a sheet of particles, usually undergo a quasi-sinusoidal variation with respect to distance. The relative phase of the quasi-sinusoidal oscillation observed at the equator is then dependent on the distance from the equator of the resonance point. This results in the sinusoidal-like variation in the rms pitch angle scattering versus energy curve in Figure 2.11, since the location of the resonance point is a function of energy. Although the details of the rms scattering patterns for the half-wave and full-wave distributions are different, both patterns show the same dependence on particle energy.

Figure 2.12 shows the envelope of rms scattering for wave frequencies of 5.46 kHz, 10.9 kHz, and 21.8 kHz, corresponding to equatorial resonance energies of 523, 265, and 107 keV, respectively. The wave power density at the equator was taken to be the same for all cases, resulting in different equatorial wave amplitudes, namely, 7.5 pT, 6.4 pT, and 5.6 pT, respectively, due to different refractive indices. For waves at half the equatorial gyrofrequency the amplitude corresponding to this power density would be 5 pT. The result for 5.46 kHz is the same as that shown in Figure 2.10 and is repeated here for comparison. The initial equatorial pitch angle was taken to be 16.77° in all cases. The peak rms scattering is larger for higher wave frequencies (lower resonance energies) due to the longer interaction times. The dashed curves in Figure 2.12 show the latitude of resonance as a function of particle energy. For the same percentage deviation above the equatorial resonance energy, the latitude of resonance is further away from the equator for the higher frequency case, resulting in the narrower peak of the rms scattering curve.

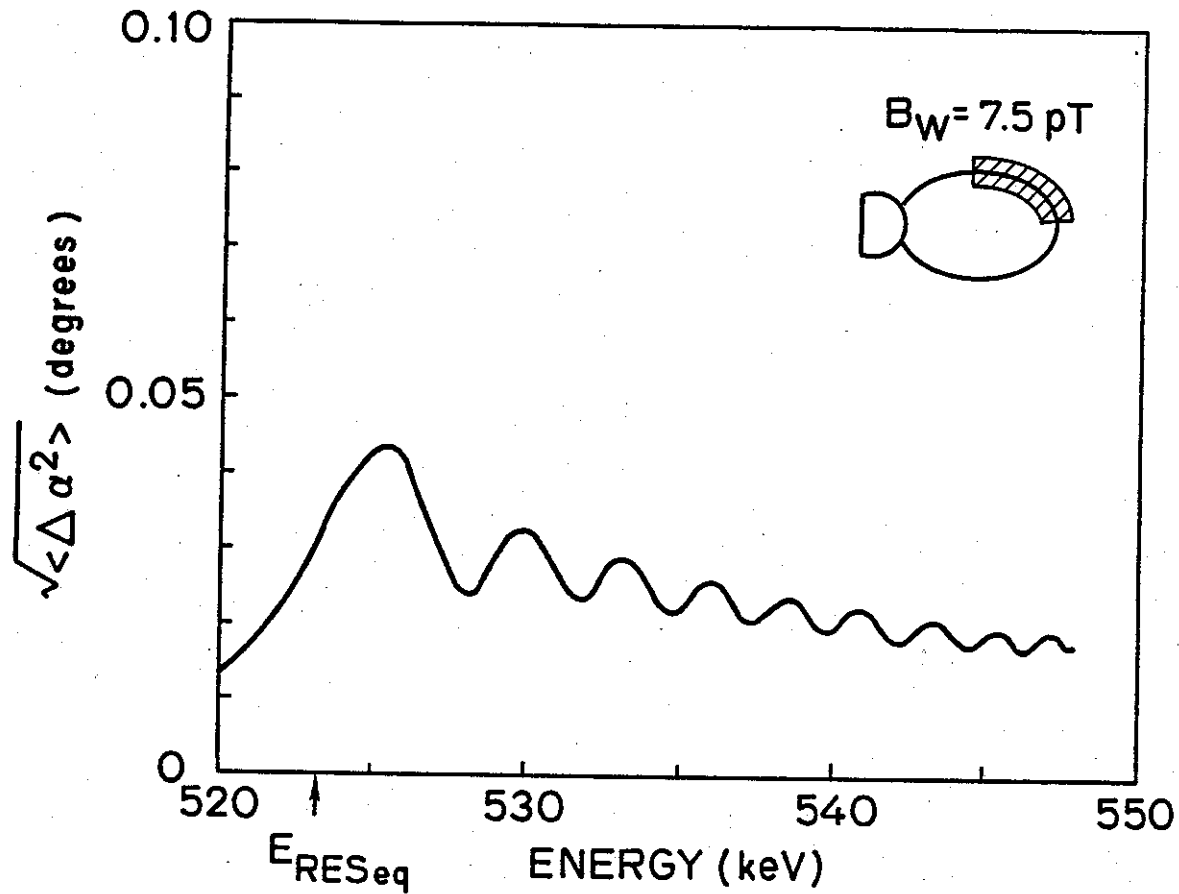


FIGURE 2.11 THE RMS SCATTERING VERSUS PARTICLE ENERGY FOR A HALF-SIDED WAVE STRUCTURE. The wave is turned off in the southern part of the field line. All other parameters are the same as in Figure 2.10.

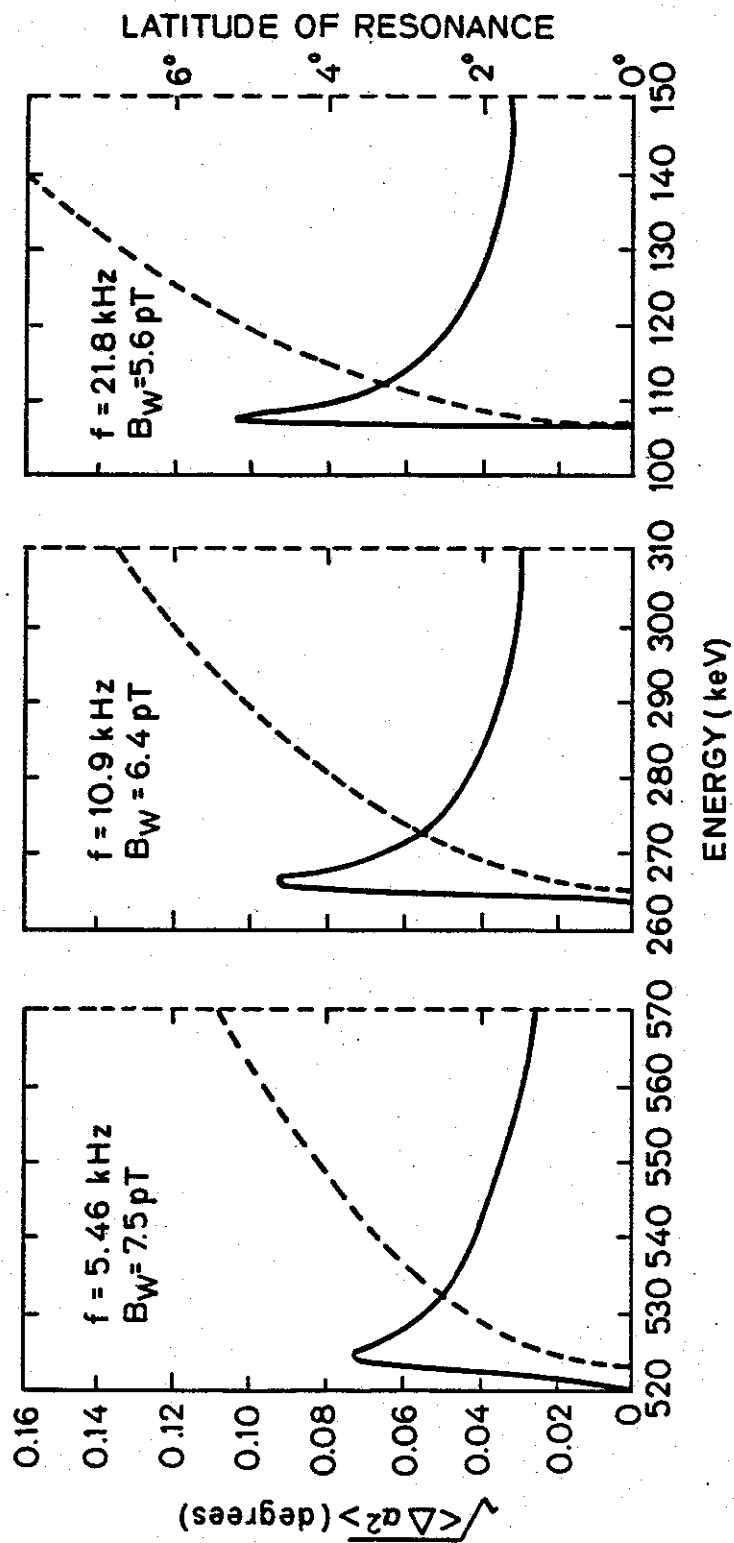


FIGURE 2.12 THE ENVELOPE OF RMS SCATTERING PATTERN VERSUS PARTICLE ENERGY FOR THREE DIFFERENT WAVE FREQUENCIES AT $L=2$. The wave power density at the equator has been taken to be the same for all cases, resulting in slight variations in the equatorial wave amplitude. The $f=5.46$ kHz case is identical to the one shown in Figure 2.10. The dashed curves show the latitude of resonance as a function of particle energy.

F. ENERGETIC ELECTRON DISTRIBUTION FUNCTIONS

In the rest of this report we shall consider wave-induced perturbations of a distribution of energetic electrons trapped along the earth's magnetic field line. Perturbation of trapped distribution near the loss cone causes the scattering of electrons into the loss cone and results in their precipitation into the ionosphere.

Using the adiabatic invariant, the parallel velocity and pitch angle of trapped particles can be inferred at each point along the field line for specified values of these parameters at the geomagnetic equator. Therefore, the energetic electron population in a magnetic flux tube can be represented by a distribution function defined at the equator [Inan *et al.*, 1978].

The particle distribution function used in our analysis is the velocity space distribution which when integrated over the velocity space volume gives the number density (el/cm³) of electrons. When the velocity space is specified by using the spherical coordinates v , α , and ϕ , the volume element becomes $v^2 \sin \alpha dv d\alpha d\phi$, where ϕ is the Larmor phase angle. In the case of cyclotron resonance interactions, the resonance condition (2.22) is written in terms of the particle's parallel velocity v_{\parallel} . It is therefore more convenient to use the v_{\parallel} , α , and ϕ as the independent variables in velocity space in our test particle simulation. It can be shown that in these coordinates the velocity space volume element is $v_{\parallel}^2 (\sin \alpha / \cos^3 \alpha) dv_{\parallel} d\alpha d\phi$ [Inan, 1977].

We denote the (equatorial) distribution function as $f(E, \alpha)$, where E is the energy and α is the equatorial pitch angle of the electron. In this report the α employed in the distribution function or in the manipulation related to distribution function will implicitly represent the *equatorial* pitch angle. Since $E = mc^2 [(1 - v_{\parallel}^2/c^2 \cos^2 \alpha)^{-1/2} - 1]$, $f(E, \alpha)$ is a function of v_{\parallel} and α and would be defined such that the number density of electrons within $v_{\parallel} \pm \frac{\Delta v_{\parallel}}{2}$ and $\alpha \pm \frac{\Delta \alpha}{2}$ in velocity space, when Δv_{\parallel} and $\Delta \alpha$ are sufficiently small, is given by

$$\Delta N = 2\pi f(E, \alpha) v_{\parallel}^2 \frac{\sin \alpha}{\cos^3 \alpha} \Delta v_{\parallel} \Delta \alpha, \quad (2.25)$$

where we have assumed a uniform distribution in ϕ , and 2π is due to the integration over ϕ .

Assuming that electrons with equatorial pitch angle less than α_{eq}^{lc} are precipitated at the ionosphere, the total number density of such precipitated electrons in the

energy range of E_1 to E_2 is given by

$$N_T = 2\pi \int_0^{\alpha_{eq}^{lc}} \int_{v_{||1}}^{v_{||2}} f(E, \alpha) \left[\frac{\cos \alpha}{\cos \alpha_i} \frac{B_i}{B_{eq}} \right] v_{||}^2 \frac{\sin \alpha}{\cos^3 \alpha} dv_{||} d\alpha, \quad (2.26)$$

where $v_{||1}$ and $v_{||2}$ are given by $E_1 = mc^2[(1 - v_{||1}^2/c^2 \cos^2 \alpha)^{-1/2} - 1]$ and $E_2 = mc^2[(1 - v_{||2}^2/c^2 \cos^2 \alpha)^{-1/2} - 1]$, respectively, and B_i and α_i are the magnetic field strength and the pitch angle, respectively, at the ionospheric height. The variables α and α_i are related by the adiabatic mirror equation $\sin^2 \alpha / B_{eq} = \sin^2 \alpha_i / B_i$. The factor $[(\cos \alpha / \cos \alpha_i)(B_i / B_{eq})]$ in (2.26), which can be obtained from the above mirror equation, accounts for the reduced volume element of the flux tube at the ionosphere compared to that at the equator due to the convergence of the field lines.

The precipitated energy flux, or the energy deposition rate (in units of energy per area per second) associated with (2.26) is obtained by integrating the quantity $Ev \cos \alpha_i f(E, \alpha)$ over the velocity space and is given by

$$Q = 2\pi \int_0^{\alpha_{eq}^{lc}} \int_{v_{||1}}^{v_{||2}} Ev \cos \alpha_i f(E, \alpha) \left[\frac{\cos \alpha}{\cos \alpha_i} \frac{B_i}{B_{eq}} \right] v_{||}^2 \frac{\sin \alpha}{\cos^3 \alpha} dv_{||} d\alpha,$$

where v is the total velocity of the electron with energy E . From (2.3) B_i/B_{eq} can be expressed as $L^3(1 + 3 \sin^2 \lambda_i)^{1/2}$, where λ_i represents the latitude at which the field line on L -shell crosses ionospheric altitude where the precipitation takes place. Substituting this for B_i/B_{eq} and $v_{||}$ for $v \cos \alpha$, the expression for Q can be rewritten as

$$Q = 2\pi \int_0^{\alpha_{eq}^{lc}} \int_{v_{||1}}^{v_{||2}} Ev_{||} f(E, \alpha) v_{||}^2 \frac{\sin \alpha}{\cos^3 \alpha} dv_{||} d\alpha [L^3(1 + 3 \sin^2 \lambda_i)^{1/2}]. \quad (2.27)$$

In this report we consider unperturbed trapped energetic electron distribution functions of the form

$$f(E, \alpha) = \begin{cases} AE^{-n/2} g(\alpha), & \text{if } \alpha \geq \alpha_{eq}^{lc}; \\ 0, & \text{if } \alpha < \alpha_{eq}^{lc}, \end{cases} \quad (2.28)$$

where A is a constant, $n/2$ is an exponent that can be adjusted to obtain a fit with observed distributions, and $g(\alpha)$ represents the pitch angle dependence. The function $g(\alpha)$ determines the isotropy or anisotropy of the distribution, with $g(\alpha) = 1$

representing an isotropic one. For the purpose of comparing with observed distributions conventionally described in terms of the 'differential energy spectrum' in $\text{el/cm}^2 \text{ s sr keV}$, the constant A can be related to the differential energy spectrum Φ_{E_0} of electrons at a given energy E_0 (keV) and with $\alpha=90^\circ$ pitch angle as

$$A = \Phi_{E_0} \left(\frac{m^2}{mc^2} \right) \left(\frac{\gamma_0^5}{\gamma_0^2 - 1} \right) E_0^{n/2}, \quad (2.29)$$

where mc^2 is the rest energy of the electron and γ_0 is the relativistic factor associated with the energy E_0 (in keV). The relationships between A and Φ_{E_0} and between $f(E, \alpha)$ and Φ_E are derived in Appendix A. It can be seen from (2.29) that A is proportional to Φ_{E_0} and thus the absolute values of the precipitated fluxes shown in the later sections of this report are directly proportional to the trapped electron differential energy spectrum Φ_{E_0} .

The energy spectrum of the precipitating electrons in $\text{el/cm}^2 \text{ s keV}$ can also be calculated by simply integrating $(1/\Delta E)v_{\parallel}f(E, \alpha)$ over the loss cone in the velocity space, where ΔE is the differential energy corresponding to a given energy E . Figure 2.13 shows the calculated energy spectrum of precipitating electrons for the case of Figure 2.10. The energetic electron distribution was taken to be as given by (2.28) or (2.29), with $g(\alpha)=1$ (isotropic), $n=4$ and $\Phi_{E_0}=4.5 \times 10^5 \text{ el/cm}^2 \text{ s sr keV}$ for $E_0=100 \text{ keV}$. Note that if we assume the energy dependence of the energetic electron distribution to be E^{-2} , then this gives Φ_{E_0} of $10^8 \text{ el/cm}^2 \text{ s sr keV}$ for $E_0=1 \text{ keV}$, which was the reference flux level used in previous work [Inan *et al.*, 1978] and will be adopted in most cases in this report.

The energy spectrum of the flux exhibits a pattern similar to that of the rms scattering. The small irregularities result from the finite bin width used in the numerical calculations. By comparing Figures 2.10 and 2.13 it can be noted that the maxima and minima in the energy spectrum show a one-to-one correspondence to those in the rms scattering pattern with negligible shift in energy. This in turn indicates that the energy change suffered by the electrons is negligibly small compared to the pitch angle change, since Figure 2.10 is plotted as a function of initial resonance energy while Figure 2.13 is in terms of the precipitated or scattered energy. Also note that the rms scattering pattern is not dependent on $f(E, \alpha)$ while the precipitated energy spectrum which results from the integration of $v_{\parallel}f(E, \alpha)$ strongly depends on the assumed distribution function.

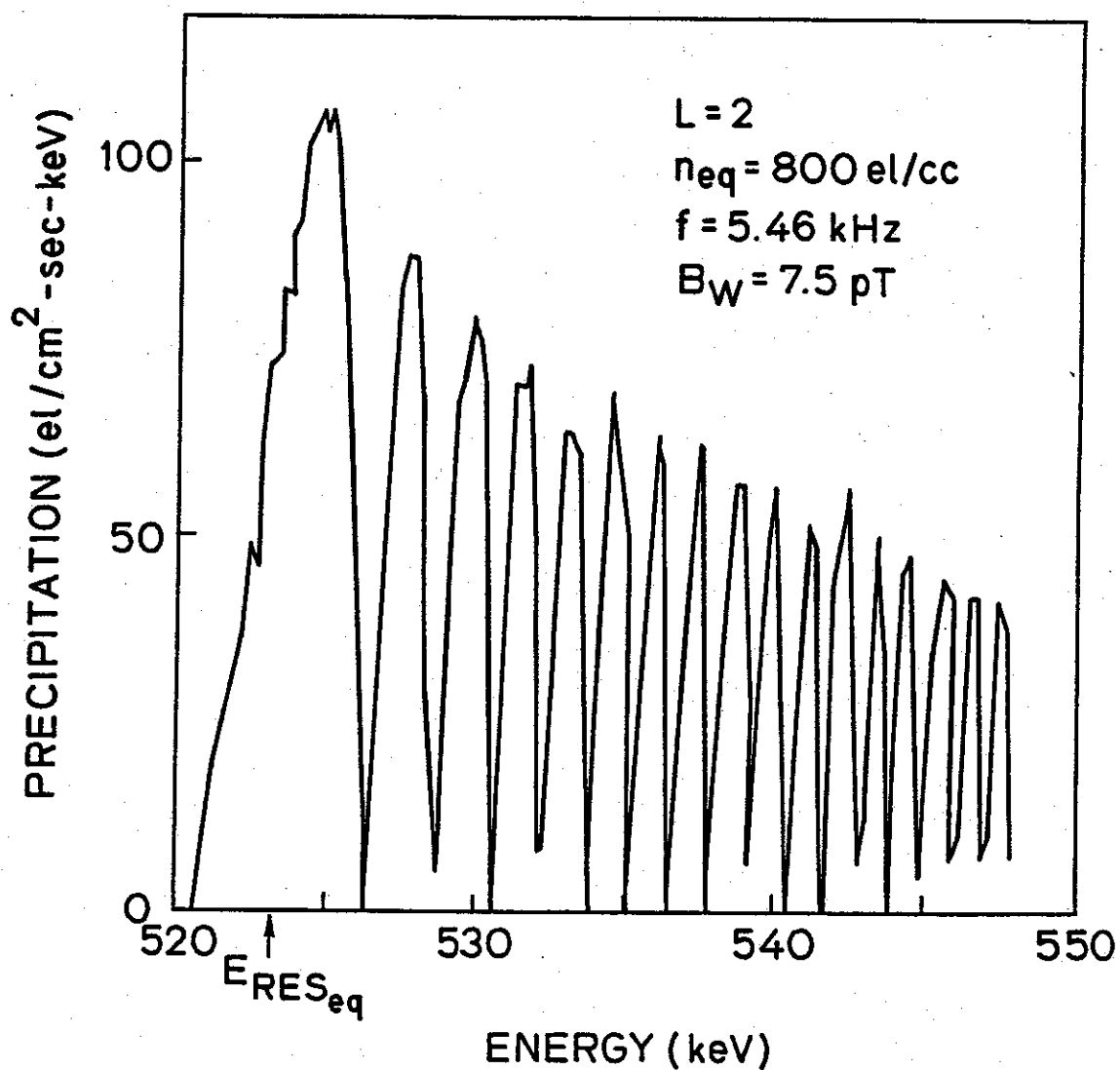


FIGURE 2.13 THE ENERGY SPECTRUM OF PRECIPITATING PARTICLES FOR THE CASE OF FIGURE 2.10. The energetic particle distribution is given by equations (2.28) and (2.29), with $g(\alpha)=1$, $n=4$, and $\Phi_{E_0}=4.5 \times 10^5 \text{ el/cm}^2 \text{ s sr keV}$ for $E_0=100 \text{ keV}$ at 90° pitch angle.

The spectral details of the result shown in Figure 2.13 cannot be detected with presently available particle detectors due to lack of sufficiently high resolution [Imhof *et al.*, 1981a]. However, the envelope of the energy spectrum represents measurable information. The variation of the envelope is determined by the relative strength of scattering given by Figure 2.10 and the relative population of particles at different energies. The decrease of envelope as energy increases in Figure 2.13 is faster than that in Figure 2.10 since we assume an E^{-2} variation of the electron distribution. If we define the equivalent width of the energy spectrum as the full width in energy at half maximum of the flux (FWHM), then the width seen in Figure 2.13 is ~ 20 keV. By using the same definition the equivalent width of the rms scattering in Figure 2.10 is more than 20 keV. The width of the energy spectrum would be smaller for initial trapped distributions that have steeper falloffs in energy.

In the present calculation we have assumed a sharp loss cone edge and an otherwise isotropic initial trapped electron distribution. The maximum pitch angle scattering at a given energy determines the range in pitch angle above the loss cone of the trapped electrons which contribute to the precipitation at that energy during a single encounter with the wave. For energies near the equatorial resonance energy the maximum pitch angle change is larger and thus the contributing range in pitch angle is wider. Due to this factor, an electron distribution with a smoother loss cone edge, e.g., a linear or an exponential increase with pitch angle (rather than a step), will result in a narrower width in the precipitated energy spectrum. Assumption of a smoother edge of the loss cone might be more realistic since the particle distributions in the magnetosphere tend to have this property [Lyons and Williams, 1975].

Although the energy spectrum of the precipitated flux is strongly dependent on the assumed trapped electron distribution, the equivalent width of the rms scattering pattern of the near-loss-cone electrons can give us an upper bound to the equivalent width of the energy spectrum due to a full distribution of electrons. In chapter IV we compare the experimentally observed peaks in energy spectrum of precipitating electrons with the widths predicted by our results.

III. TRANSIENT ENERGETIC ELECTRON PRECIPITATION INDUCED BY VLF WAVE PACKETS IN THE MAGNETOSPHERE

A. INTRODUCTION

In this chapter we calculate the precipitation of energetic electrons into the ionosphere due to the interaction of these electrons with short-duration VLF waves in the magnetosphere. A previous test particle simulation model [*Inan et al.*, 1978], which was used to study the steady-state case of the interaction of a continuous VLF wave (CW) with the trapped electrons, is extended to the transient case. It is used to compute the detailed temporal variation of the precipitated energy flux induced by VLF wave packets for various wave parameters and for different trapped energetic electron distribution functions.

Precipitation of the radiation belt electrons is one result of the gyroresonance wave-particle interactions in the magnetosphere. The waves involved in these interactions are (1) natural whistlers and chorus emissions, and (2) signals from ground based sources, such as VLF transmitters and large-scale power grids, and emissions triggered by these signals. Most of these signals are frequency-varying in nature. In this chapter we shall consider both monochromatic and variable frequency signals.

During its propagation between the two hemispheres a VLF wave pulse can interact with electrons of different energy and pitch angle as determined by the cyclotron resonance condition (2.22). The precipitated energy flux thus consists of electrons that have encountered and interacted with the wave at different locations along the field line and that therefore arrive at the ionosphere at different times. We take into account the full nonlinear interaction of all test particles with the wave as well as the wave group travel time and the particle travel times. The result obtained is the precipitated energy flux as a function of time after the injection of the wave into the magnetosphere. The energy of the downcoming electrons is also given as a function of time, since this determines the ionospheric altitude at which the flux is deposited [*Rees*, 1963; *Walt et al.*, 1968; *Banks et al.*, 1974] and is therefore important for assessing the detectability of the computed fluxes by using ground based instruments.

In the next section we comparatively discuss the resonance locations of monochromatic as well as variable frequency waves. The formulation for the problem for computing the transient electron precipitation is described in section C. Following

that, typical results of transient precipitation due to fixed and variable frequency wave packets are presented.

B. CYCLOTRON RESONANCE VELOCITY CURVES

We first demonstrate the differences in the resonance locations along the field line between monochromatic waves and waves with slowly varying frequency. We consider a longitudinally propagating whistler mode wave whose amplitude B_w , wave number k , and frequency ω all vary slowly within 2π period of the wave phase (i.e., $\Delta\omega/\omega < 1\%$ within one wave cycle). The variation of the Larmor phase ϕ is given by (2.20c), again with ω being a slowly varying quantity. In the following discussion we use the nonrelativistic equations for simplicity. The cyclotron resonance velocity is then given by $v_R = (\omega_H - \omega)/k$. For typical magnetospheric conditions, $B_w/B_0 \ll 1$, and the wave-induced perturbations in the adiabatic trajectory of the particle are cumulative only as long as the resonance condition $v_{\parallel} \simeq v_R$ is satisfied. The directions of \mathbf{v}_{\parallel} and \mathbf{k} are as shown in Figure 3.1a.

In Figure 3.1b we plot the resonance velocity v_R as the dashed curve, assuming a continuous wave of constant frequency f_2 along the field line. For this case, v_R is symmetric around the equator due to the symmetry of the local ω_H and k for the assumed dipole model of the magnetic field and diffusive equilibrium model for the cold plasma. Also shown as a dotted line in Figure 3.1b is the adiabatic parallel velocity v_{\parallel} of a particle, also symmetric around the equator. Note that the latter is a function of the particle energy and pitch angle as determined by the first adiabatic invariant. For the case when the v_R and v_{\parallel} curves are tangent to each other, the particle resonates with the wave at the equator. For other particles there exist two intersection points as indicated in Figure 3.1b, since the cyclotron resonance condition is satisfied in the vicinity of two conjugate locations along the field line. The strongest interaction takes place when the interaction point is at the equator in which case $\phi \simeq 0$ [Helliwell, 1967; Inan et al., 1978].

We now consider the case of a short fixed frequency pulse. As shown in Figure 3.1a a short pulse of duration t_{PL} and fixed frequency f_2 is taken to be propagating from south (negative latitudes) to north along the field line. The two boxes in Figure 3.1a represent the portions of the field line occupied by the wave packet at times t_1 and t_2 . Here we neglect the possible stretching and distortion of the front and tail ends of the pulse [Chang and Helliwell, 1980], since the amount of such stretching is much shorter than the pulse durations being considered in this paper. The corresponding

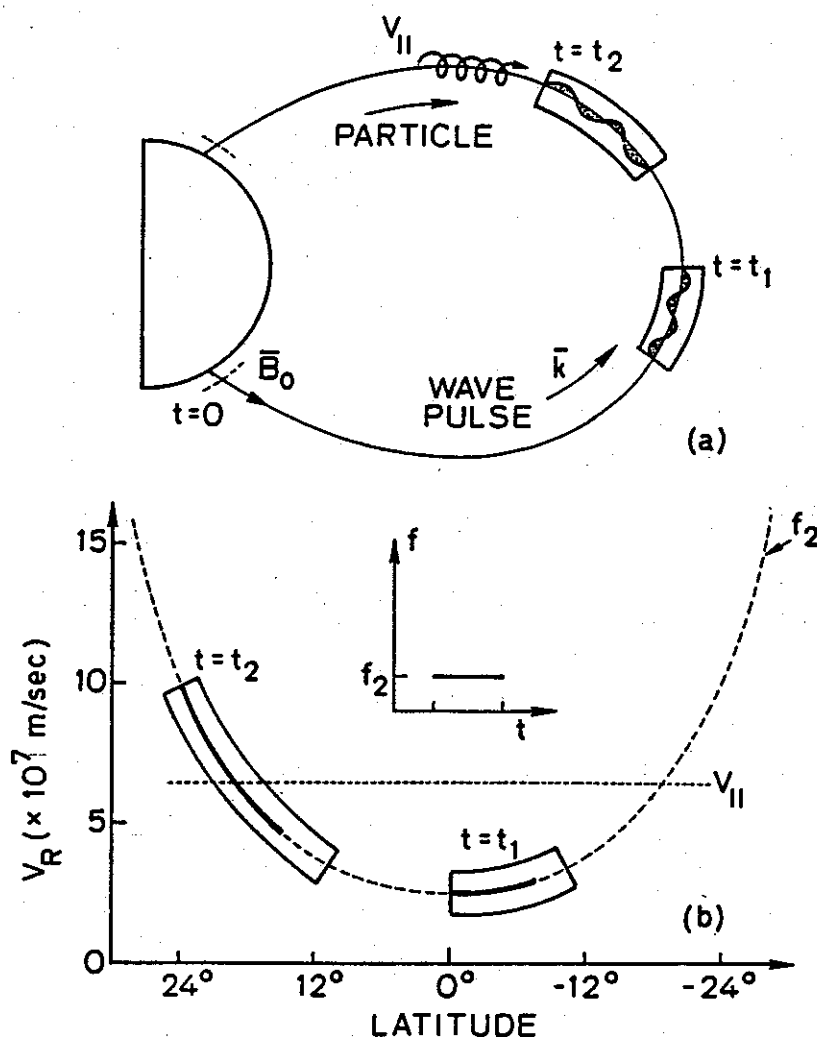


FIGURE 3.1 RESONANT INTERACTION BETWEEN A PARTICLE AND A MONOCHROMATIC WAVE PULSE. (a) Schematic describing the motion of the particle and a wave pulse. The two boxes represent the portions of the field line occupied by the wave packet at times t_1 and t_2 . (b) The dashed curve shows the resonance velocity v_R for a constant frequency f_2 . The dotted curve gives the adiabatic parallel velocity of a particle. The solid segments represent the v_R curves as observed by the particle as it encounters the front end of the wave packet at time t_1 and t_2 , respectively.

portions of the resonance velocity curve as defined by the locations of the pulse front and tail at times t_1 and t_2 , respectively, are shown by the two boxes in Figure 3.1b.

Now consider a particle which encounters the front end of the wave packet at the equator and at time t_1 . The solid segment which starts at the equator and ends

at the point at which the particle exits the wave packet represents the resonance velocity curve as 'observed' by this particle. Note that the exit point is different from the location of the tail end of the pulse at time t_1 , due to the relative motion of the particle and the wave. The point of resonance for a given particle is the intersection (if any) of the adiabatic parallel velocity curve for that particle and this solid segment. The other solid curve in Figure 3.1b is the resonance velocity variation 'seen' by another particle which encounters the wave packet at time t_2 .

Note that for a monochromatic wave the v_R variation observed by any particle that travels through the wave packet always lies on the dashed line in Figure 3.1b. Thus for that particle whose adiabatic $v_{||}$ is shown in Figure 3.1b, the point of intersection between the $v_{||}$ curve and the v_R segment determines the point of resonance for the case when this particle encounters the front end of the pulse at time t_2 . However, the cumulative scattering experienced by this particle will be negligible if this particle encounters the pulse front at time t_1 , since at that point it is far from being close to resonance.

We now apply these concepts to the more complicated cases of interactions with wave pulses having slowly varying frequency. Figure 3.2 shows two such cases, a riser and a faller. Both signals have the same initial pulse duration t_{PL} and the same upper and lower frequencies with an input $f - t$ format that varies linearly in frequency when observed at the injection point into the magnetosphere. Note that the $f - t$ format varies along the field line due to the dispersion of the signal. This variation has been taken into account in the following.

The two dashed curves in Figures 3.2a and 3.2b show v_R for constant frequency waves with frequencies f_1 and f_2 , respectively. Each segment in Figure 3.2b represents the characteristic resonance velocity curve seen by a particular particle that enters the wave packet at time t_i ($i = 1, 2, \dots, 5$) at the corresponding latitude along the field line. The segments start at the f_1 curve and end at the f_2 curve, since f_1 and f_2 are the frequencies of the front and tail ends of the wave pulse, respectively. Particles of different velocities encounter a specific frequency component of the wave pulse at different positions during their relative motion with respect to the wave packet. Thus v_R , which is determined by the wave frequency variation experienced by the particle along the field line, is different for different particles that encounter the wave at a given time. In Figure 3.2c we show v_R for the case of a faller. Note that the resonance velocity segments start at f_2 and end at f_1 in this case.

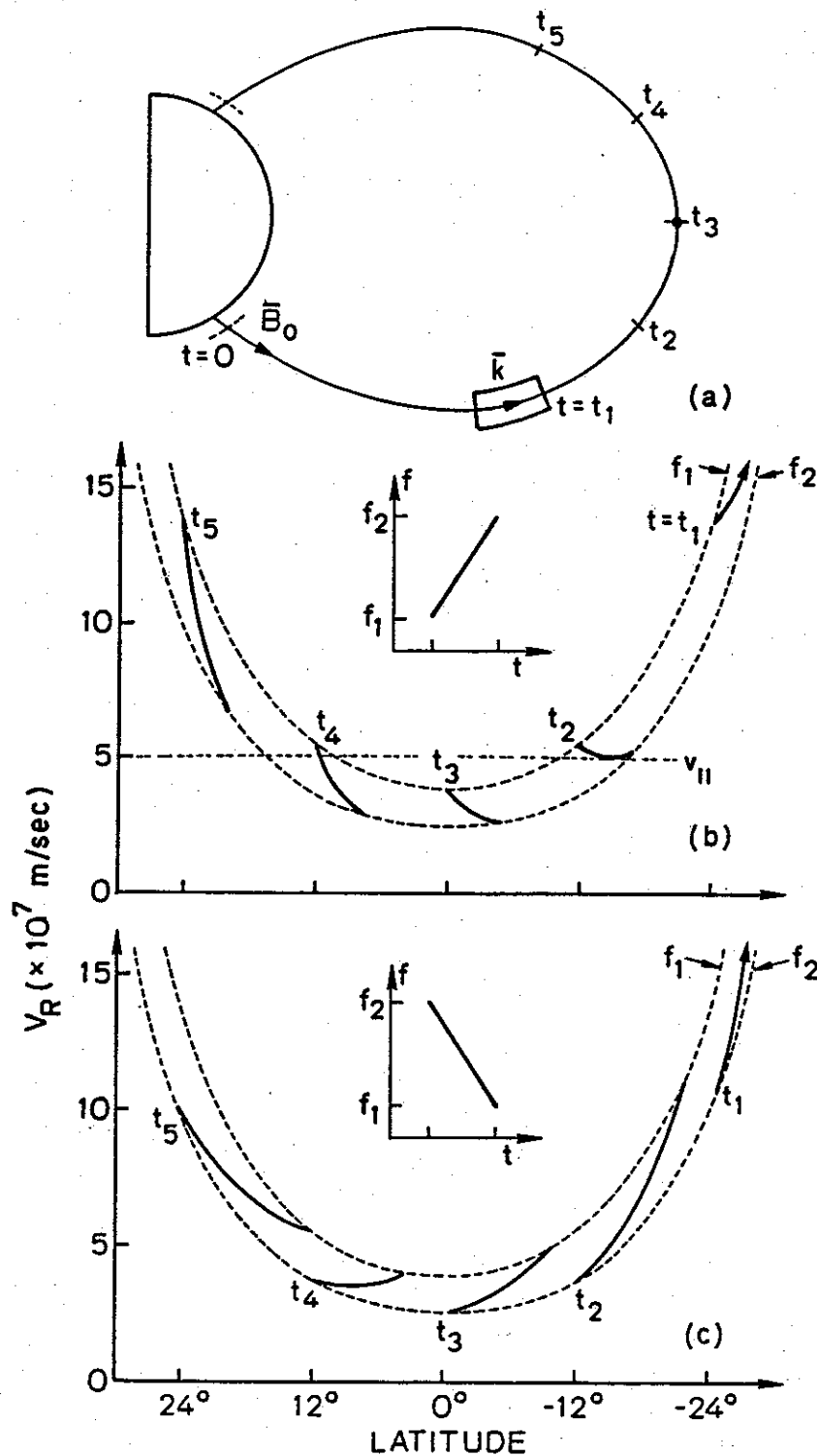


FIGURE 3.2 RESONANCE VELOCITY CURVES FOR THE CASES OF VARIABLE FREQUENCY WAVES. (a) Locations along the field line of the front end of a variable-frequency wave packet at times t_i , $i=1, \dots, 5$. (b) and (c) Typical v_R curves for the case of a linear ramp with rising frequency from f_1 to f_2 and for the case of a linear ramp with falling frequency from f_2 to f_1 , respectively. The dashed curves are the v_R curves for constant frequencies f_1 and f_2 . In (b) is shown an adiabatic parallel velocity curve of a particle tangent to one v_R curve.

The strongest interaction between the wave and the particles takes place when the resonance point is located in the neighborhood of the point where the gradient of the resonance velocity vanishes. This occurs at the geomagnetic equator for a constant frequency wave. *Helliwell* [1970] has shown that the strongest resonance point for a variable frequency wave is located off the equator at a position (termed the 'phase equator') where the spatial variation of the electron gyrofrequency is matched to the spatial variation of the doppler-shifted wave frequency seen by the particle. In the context of Figure 3.2 this is represented by the point of tangency between v_{\parallel} (dotted curve) and v_R curves and (especially for the low pitch angle particles) is located very close to the zero gradient point of the v_R curve. Although the resonance velocity is different for different particles, this point of strongest interaction can be roughly defined by some representative v_R curves. For example, in Figure 3.2b the resonance point will be located between the positions of the leading edge of the pulse at times t_1 and t_2 , since the v_R curve of a particle which meets the pulse front at $t = t_2$ shows a local minimum. On the other hand, for the faller as shown in Figure 3.2c this point is located on the other side of the equator. The neighborhood of this point will hereinafter be called the 'principal interaction region,' within which the variations of local gyrofrequency and wave frequency as seen by the resonant particle are roughly balanced, and the particle experiences an unperturbed phase variation similar to that of a particle resonating with a monochromatic wave near the geomagnetic equator [*Helliwell*, 1970].

C. FORMULATION OF THE TRANSIENT PROBLEM

In this section we review and summarize the main aspects of the formulation described in detail by *Inan et al.* [1982]. In that paper a VLF wave pulse of finite duration and of either fixed or variable frequency originating in a model magnetosphere at 1000 km altitude and at time $t=0$ was considered. The pulse duration was assumed to be at least hundreds of wave periods, so that the pulse can be treated as a narrow band coherent signal. The wave packet was assumed to propagate in a whistler mode duct along a specific field line with the wave number vector $\mathbf{k} \parallel \mathbf{B}_0$. For the background magnetosphere, a centered dipole model of the earth's magnetic field and either a diffusive equilibrium model or a collisionless model for the cold plasma distribution was employed. The wave magnetic field variation was taken to be as given by (2.7) and (2.8). As the input wave packet propagates along the field line it interacts with electrons for which the resonance condition (2.22) is locally satisfied. In general (2.22) is satisfied for electrons that travel in a direction opposite

to that of the whistler mode wave as is depicted in Figure 3.1a. Cumulative energy exchange between the wave and electron can occur only if (2.22) is satisfied for an extended time period.

In the formulation described by *Inan et al.* [1982], the initial unperturbed electron distribution was represented by an equatorial distribution function $f(E, \alpha)$ as defined by (2.28). It was assumed that the initial distribution of electrons that interact with the wave remains the same as the wave travels between the two hemispheres. This should be a good assumption, since the resonant electrons travel in the opposite direction; those that are perturbed by the wave do not come back to the equator before a time equal to their bounce period. Hence a fresh distribution of electrons continually enters its leading edge as the wave packet propagates up the field line. Using Figure 3.1a as an example, at a time t_2 , for the wave packet position shown, a distribution of electrons represented in velocity space encounter the wave front. Of these electrons only those corresponding to the shaded region, as shown in Figure 3.3a, are expected to contribute to the precipitated flux. That is, only a portion of resonant electrons in a limited range of parallel velocity and a narrow range of pitch angle near the edge of the loss cone are scattered into the loss cone after the interaction. The α_{min} is determined by the loss cone, whereas α_{max} is determined by the maximum individual electron scattering for the given wave and at that point. The $v_{||min}$ and $v_{||max}$ are determined by the equatorial parallel velocity of electrons that would go through a resonance with the wave at some time after t_2 , as is shown in Figure 3.3a, where the location of the wave pulse at time t_2 and the corresponding v_R curve are identical to those plotted in Figure 3.1b. These ranges would depend on the position of the wave front, pulse duration, group velocity and the electron travel time, as can be understood from the variation of the v_R curves in Figures 3.1 and 3.2.

The shaded region shown in Figure 3.3a is automatically determined by the computer program, based on the criterion that all test particles that would be scattered in pitch angle by more than a specified amount be considered. A typical value used below would be $\Delta\alpha > 0.1^\circ$ for a 5 pT wave intensity. In the simulation model this shaded region is divided into mesh points in the $v_{||} - \alpha$ domain as shown in Figure 3.3b. The population in each mesh point is represented by a number of test particles distributed in Larmor phase ϕ . The group of electrons that encounter the wave front at time t_2 is then modeled by inputting all test particles to the leading edge of the wave pulse at time t_2 . Each test particle has initial pitch angle of α_0 and parallel velocity of $v_{||0}$. The interaction of the wave with the test particle is governed

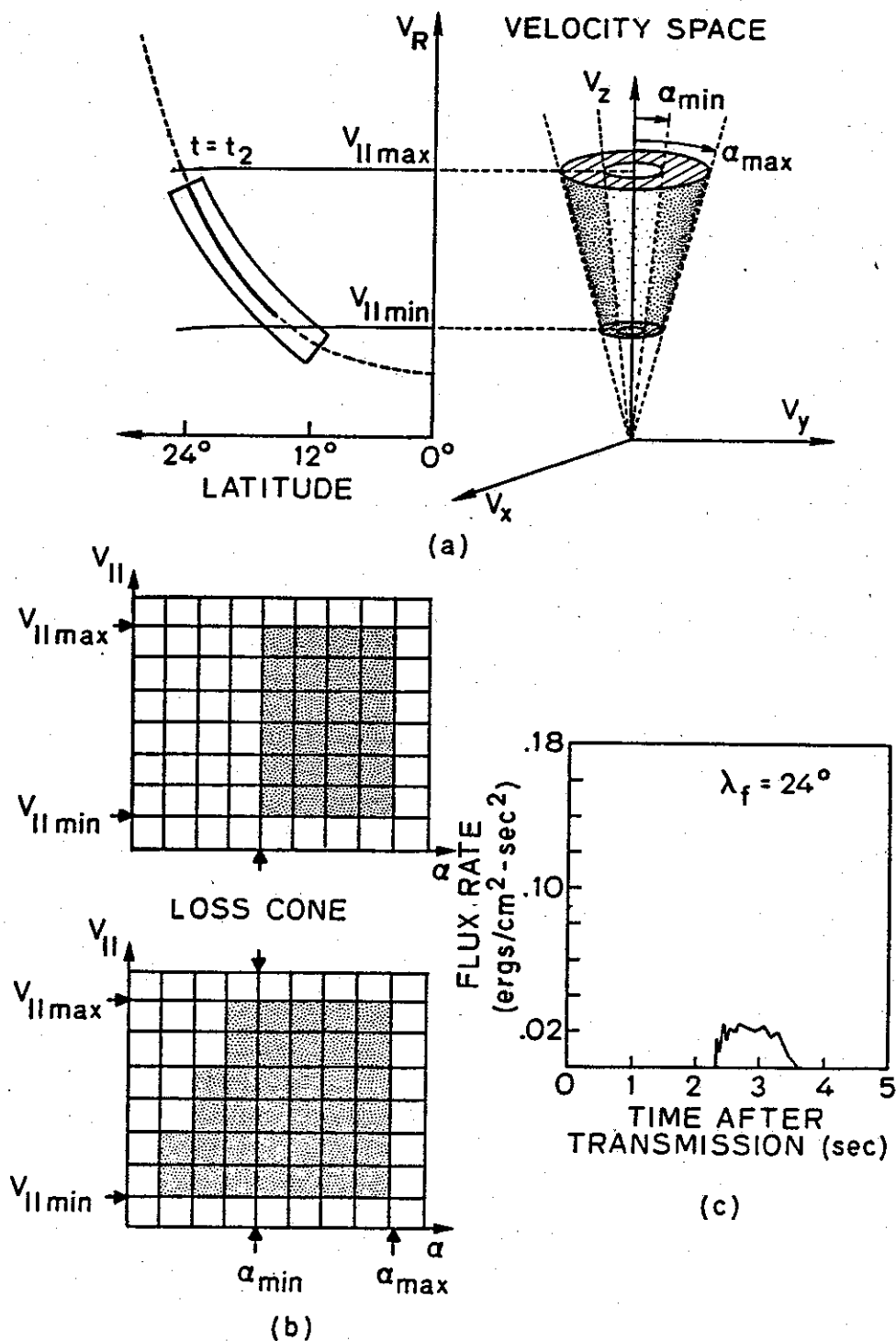


FIGURE 3.3 SCHEMATICS DESCRIBING THE WAVE-PARTICLE INTERACTIONS AND THE CALCULATION OF THE INDIVIDUAL RESPONSES. The response shown is caused by the electrons that encounter the wave front at time t_2 . Each such response is obtained by computing the perturbations of a full distribution of electrons represented by a large number of test particles with different equatorial parallel velocities, pitch angle, and Larmor phase. Note that the width of the response is determined by the range of parallel velocities that corresponds to precipitated electrons; the arrival time depends on the wave group velocity and the electron travel time.

by the equations of motion (2.18). The effect of the wave on the particle motion is then obtained by integrating these equations for each test particle until either the time when the particle exits from the wave tail or the time when the particle moves away from gyroresonance enough so that the wave perturbations becomes negligible.

After the individual test particle trajectories are determined, the perturbed distribution function is obtained, with some electrons scattered into the loss cone, as shown in the lower panel of Figure 3.3b. The electrons that are scattered into the loss cone have a range of parallel velocities, and thus energies. Consequently, they are precipitated into ionosphere below 1000-km altitude at different times. In the case of Figure 3.3, the arrival time of an electron at the precipitation region is obtained by adding t_2 to the travel time of this electron from the position of the pulse at time t_2 to the ionospheric height. After taking into account these arrival times and the contribution to the energy flux of different electrons, a precipitated energy flux rate in ergs/cm² s² can be obtained. The result is the energy flux per unit time versus time, as shown in Figure 3.3c. The energy flux in ergs/cm² s due to those electrons that meet the wave front between the times $t_2 \pm \frac{1}{2}d\tau$ can be obtained by multiplying this precipitated energy flux rate by $d\tau$. The contribution due to those electrons that encounter the wave front in the next $d\tau$ interval can be calculated in the same way by computing the precipitated flux rate corresponding to the next position of the wave front at time $t_2 + d\tau$. The response corresponding to this new position of the wave front will however be slightly different since the interaction conditions, due to the inhomogeneity of the medium, are a function of latitude.

The cold plasma density and the static magnetic field intensity both change along the field line; therefore the energy and pitch angle range of the resonant electrons varies as well as the efficiency of the wave-particle interaction. Also the effective pulse length as well as the interaction length seen by each electron is also different and have been taken into account in the computer model. Each energy flux rate response is expressed as $h[t, \tau(\lambda_f)]$, where λ_f is the geomagnetic latitude of the wave front and is related to the time τ by

$$\tau(\lambda_f) = \int_{-\lambda_1}^{\lambda_f} \frac{dz}{v_g(\lambda)d\lambda} d\lambda, \quad (3.1)$$

where z is the distance along the field line, $v_g(\lambda)$ is the local group velocity of the whistler mode wave, and λ_1 is the latitude at 1000-km altitude. With this definition,

$h(t, \tau)d\tau$ is the precipitated energy flux in ergs/cm² s at the precipitation region versus time t due to those electrons that meet the leading edge of the propagating wave packet between times $t=\tau - \frac{1}{2}d\tau$ and $t=\tau + \frac{1}{2}d\tau$. Thus, $h(t, \tau)$ is equivalent to the response at time t due to an external excitation applied to a system at time τ . The total system response, or the total precipitated energy flux as a function of time due to all downcoming electrons that encounter the wave packet at different latitudes and times, is then the integral of $h(t, \tau)d\tau$. In other words,

$$r(t) = \int_0^{\infty} h(t, \tau)d\tau, \quad (3.2)$$

where $r(t)$ is the precipitated energy flux in the precipitation region as a function of time after the wave injection.

Since by assumption the energetic electron motions do not affect one another, $h(t, \tau)$ for different τ 's due to interaction with different incoming distribution of fresh electrons can be calculated separately. Figure 3.4 illustrates the variation of the responses $h(t, \tau)$ as a function of time τ (or λ_f) for a wave pulse of 0.4-s duration propagating along the $L=4$ field line. The wave frequency is taken to be equal to half the equatorial gyrofrequency, or 6.83 kHz, and the equatorial wave intensity is taken to be 5 pT. A diffusive equilibrium model and an equatorial cold plasma density $n_{eq}=400$ el/cm³ corresponding to a plasma frequency of 180 kHz are used.

The top panel shows the response due to the electrons that encounter the wave at -12° latitude at time τ_1 . The precipitated electrons arrive at the 1000-km ionosphere altitude at $t=1-2$ s after the injection of the wave at the same point. The second panel shows the response due to electrons that encounter the wave front at the equator, i.e., 0° latitude. The electrons arrive at the ionosphere at $t=3.3-3.7$ s, indicating that the range of parallel velocities of electrons that enter the wave at τ_2 (and are able to resonate with it) is narrower. This result is due to the fact that the variation of the cold plasma parameters and hence that of the cyclotron resonant velocity of electrons in the magnetosphere less at lower latitudes, as is clearly shown in Figure 3.1b. The third panel shows the response due to electrons that encounter the wave front at $+12^\circ$ latitude and at a later time τ_3 . The precipitated electrons reach the ionosphere at $t=3.2-4.2$ s after transmission of the wave. The range of arrival times of precipitating electrons involved in this case overlaps with that in the second panel. An effect similar to this 'arrival time convergence' effect has been previously reported [Helliwell et al., 1980a] and can be roughly described by using

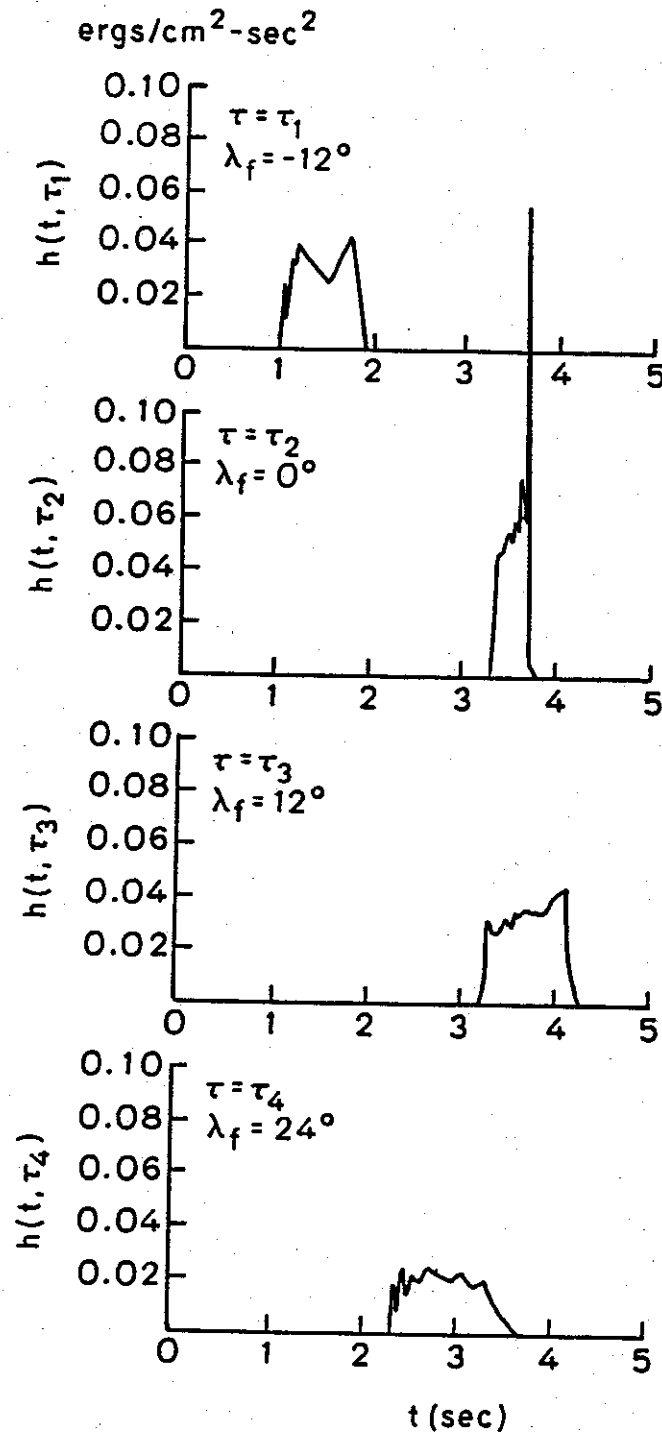


FIGURE 3.4 THE RESPONSES DUE TO FOUR DIFFERENT POSITIONS OF THE WAVE FRONT AS IT PROPAGATES ALONG THE FIELD LINE. The arrival time of the pulse for the bottom panel is shorter compared to those for the middle two panels even though this response is due to those electrons that meet the wave at a later time. This is due to the fact that the energies of the resonant electrons are higher for the former case.

approximate analytical expressions for wave group velocity and the unperturbed parallel velocity of the resonant electrons [Doolittle, 1982]. It results from the fact that the near-resonance electrons interacting with the wave at higher latitudes beyond the equator are at a higher energy and therefore can overtake the lower-energy electrons that are near-resonant at lower latitudes. The bottom panel shows the response due to electrons that encounter the wave front at time τ_4 at $+24^\circ$ latitude. The resonant electrons have even higher energies such that they arrive at the precipitation region earlier than those in the second and third panels.

The responses $h(t, \tau)$ corresponding to a number of latitudinal positions of the wave front are computed by choosing the number of steps empirically as a function of the L value and pulse length. As an example, for $L=4$ and a 400-ms wave pulse, latitudinal steps separated by 4° were taken. Since the medium is slowly varying, the responses due to the in-between wave front positions can then be calculated by using linear interpolation. The total response, i.e., the total precipitated energy flux as a function of time, is then obtained from (3.2). For the case in hand, the energy flux versus time is given in the top panel of Figure 3.5. Flux in $\text{ergs/cm}^2 \text{ s}$ is shown as a function of time after the injection of the input wave packet. The result shown is for an energetic electron distribution given by (2.28) or (2.29) with $g(\alpha)=1$ (isotropic), $n=6$, and $\Phi_E=10^8 \text{ el/cm}^2 \text{ s sr keV}$ for $E=1 \text{ keV}$. The increase in the flux after approximately $t=2.5 \text{ s}$ is due to the arrival time convergence effect mentioned above. The exact shape of this curve depends on the wave pulse length, frequency, and the electron distribution function [Inan *et al.*, 1982].

The lower panel in Figure 3.5 gives the energy range of the downcoming precipitated flux as a function of time. In calculating $h(t, \tau)$ for a given τ , only a limited range of electron energies will contribute to the energy flux. For different electron energies the arrival times are different, and we can therefore plot an energy versus arrival time curve for each τ . We have plotted the energy versus arrival time for each of the responses corresponding to the τ steps used to compute $r(t)$. In this case the τ 's are for latitudes of the leading edge of the wave pulse ranging from $\lambda_f=-16^\circ$ (the curve to the very left) to $\lambda_f=44^\circ$ in steps of 4° . The curves progress from lower left to lower right and then to upper right. The diagram thus gives the energy range of the downcoming precipitated flux as a function of time. For example, it can be seen that the flux at $t=4 \text{ s}$ consists of electrons from much narrower ranges of energies (0.4–0.6 keV) than that at $t=3 \text{ s}$ (0.4–5 keV). The shaded area of this diagram then represents the region in the time-energy domain where we expect to observe the precipitated flux after the injection of the input wave pulse at $t=0$.

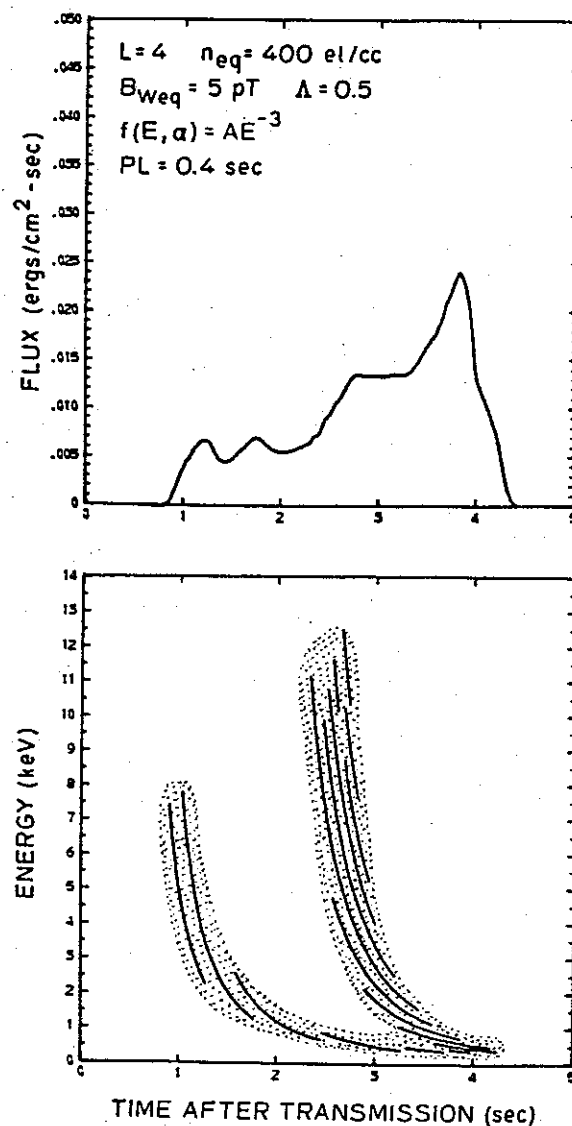


FIGURE 3.5 TRANSIENT PRECIPITATED ENERGY FLUX INDUCED BY A WAVE PULSE AT $L=4$. The top panel shows the precipitated energy flux versus time after injection of the wave into the magnetosphere at 1000-km altitude. The bottom panel shows the energy of the electrons that constitute the flux. Each separate segment shows the energy versus arrival time for one of the responses corresponding to one of the positions of the wave front. In this case the individual responses were computed for $\lambda_f = 16^\circ$ to 44° with steps of 4° .

The formulation described above has been applied to compute the transient electron flux precipitated out of the magnetosphere by relatively short VLF wave pulses under a broad range of magnetospheric conditions. The dependence of the

results on the energetic electron distribution function, the normalized wave frequency $\Lambda = \omega/\omega_{Heq}$, L value of the path of propagation, cold plasma density n_{eq} , and wave intensity B_w was reported in detail by *Inan et al.* [1982]. These results have further been used to study the potential precipitation zones around major ground based VLF transmitters [*Inan et al.*, 1983]. In the following we summarize the main results reported by *Inan et al.*, [1982] about the roles of several magnetospheric parameters which are essential in establishing the applicability of our model results.

It was shown that the total and peak precipitated energy fluxes are linearly proportional to the wave magnetic field intensity B_w for moderate wave intensities (e.g., $B_w \leq 10$ pT at $L=4$). Also these quantities are proportional to the reference differential energy spectrum Φ_{E_0} assumed in (2.29). Therefore the results of our computations can be scaled up or down to obtain the flux values at other values of Φ_{E_0} and B_w .

It was also demonstrated that the flux level and shape of the precipitation pulse are strongly dependent on the spectral composition of the trapped electron distribution, for instance, the falloff in energy, or the n value in (2.28), of $f(E, \alpha)$. This fact has important implications in the diagnostics of the energetic electron distribution near the loss cone from experimental observations and will be used when we discuss the application of the theoretical model to the explanation of observed data in chapter IV. One interesting finding by *Inan et al.* was that for $\Lambda \leq 0.5$ at $L=4$, the precipitated energy flux is proportional to approximately $E^{(5-n)/2}$. In other words, when $n \simeq 5$ in (2.28), the flux would be roughly independent of wave frequency and thus resonant energy.

For most of the results presented in this report we shall be using an isotropic energetic electron distribution with $g(\alpha)=1$ with an abrupt loss cone. For an anisotropic distribution peaked around $\alpha=90^\circ$, the precipitated flux values can be obtained from those given by simple scaling as long as $g(\alpha)$ is flat for a few degrees above the loss cone [*Inan et al.*, 1978]. In this case the flux values would be reduced by a factor of $[g(90^\circ)/g(\alpha_{lc})]$, where α_{lc} is the half angle of the loss cone.

In cases of strong anisotropy in the vicinity of the loss cone, such scaling would not be valid and it was shown that further reduction in flux would result depending on the variation of $g(\alpha)$ near the edge of the loss cone.

D. PRECIPITATION INDUCED BY VARIABLE FREQUENCY SIGNALS

We now consider two input wave pulses with linearly rising and falling frequencies, the formats of which are shown in the upper panels of Figure 3.6. Both pulses have the same initial duration of 0.3 s and upper and lower frequencies of 4.0 kHz and 2.5 kHz, respectively. Again we consider interactions on the $L=4$ field line with an equatorial electron density of 400 el/cm^3 and a diffusive equilibrium model for the cold plasma distribution. The wave pulses are normalized to have an input power density of $1.67 \times 10^{-8} \text{ W/m}^2$ corresponding to that of a fixed frequency wave at half the equatorial gyrofrequency (6.83 kHz at $L=4$) with magnetic field intensity of 5 pT at the equatorial plane.

Owing to the dispersive nature of the magnetospheric medium, the temporal duration of a variable frequency wave packet changes as it propagates along the field line. Assuming no dissipation of wave energy, the power density and the magnetic field intensity of a propagating wave pulse will vary along the field line in accordance with the variation of the instantaneous pulse duration, the local cross-sectional area of the duct to which the energy is assumed to be confined, and the local refractive index. Details of these properties are discussed in Appendix B. In our calculations we have taken full account of these pulse duration and wave amplitude variation effects. Indeed, these effects are found to be essential in the correct interpretation of the following results.

The upper panels of Figure 3.6 show the precipitated energy fluxes versus time induced by the riser and faller, assuming $n=6$ in (2.28). The lower panels, termed 'energy diagrams', show the energy ranges and arrival times at the ionosphere of the particles constituting these downcoming fluxes. In the case of the riser, the leftmost curve corresponds to the case where the pulse front is at -20° latitude ($\lambda = -20^\circ$) and each following curve accounts for a 4° increase in latitude until the pulse front reaches $\lambda = 24^\circ$. As the pulse travels up the field line, the curve shifts to the right in the diagram due to the increased group delay of the wave packet and the travel time for particles. The energy curves for the faller in the lower right panel of Figure 3.6 are shown from $\lambda = -16^\circ$ to 32° latitude with a 4° step.

The shortest segments in the energy diagram, marked $\lambda = -12^\circ$ for the riser and $\lambda = +12^\circ$ for the faller, represent the steps when the front end of the pulse is within the principal interaction region as defined in section B. The fact that it has the narrowest energy range can be understood from Figure 3.2; the range in particle parallel velocity of the v_{\parallel} curves which could have points of intersection with the v_R curve is the smallest for the step around the principal interaction region.

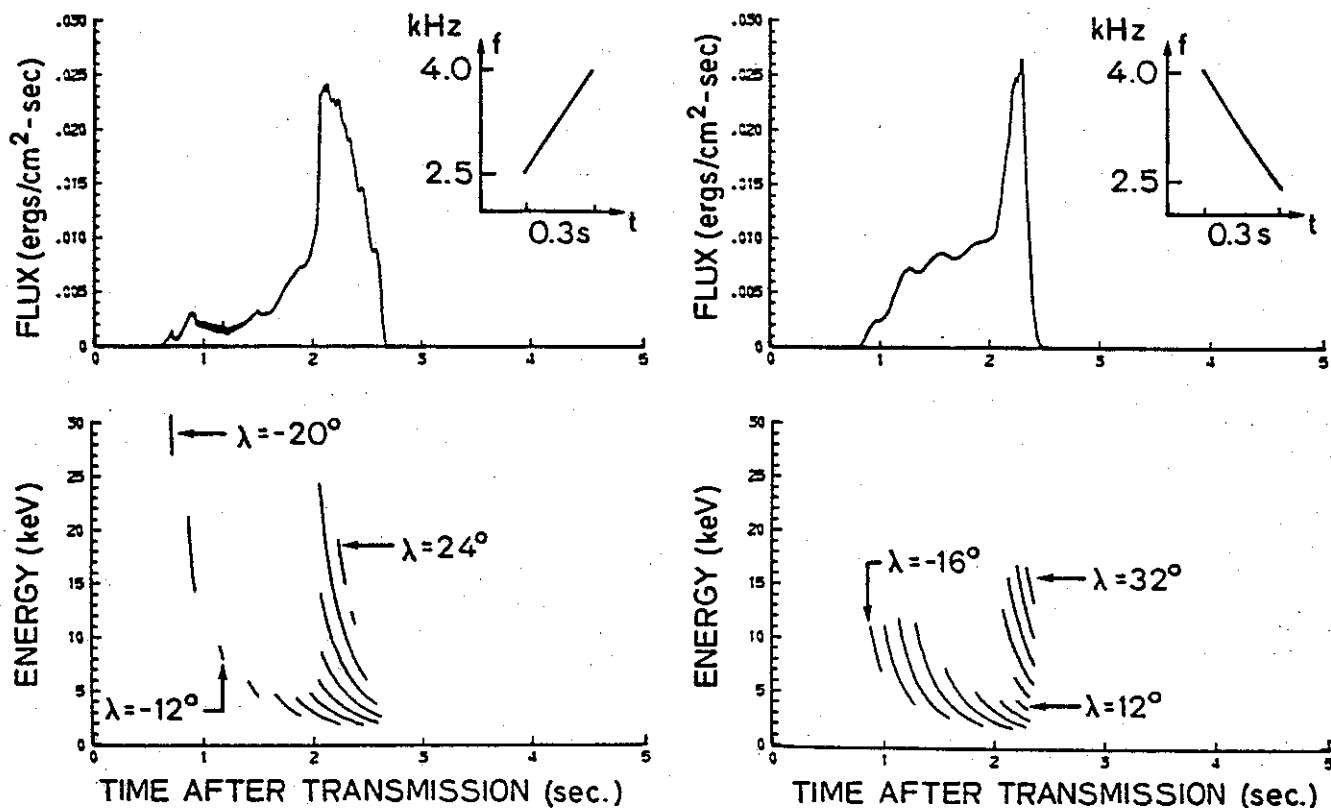


FIGURE 3.6 PRECIPITATED ENERGY FLUXES INDUCED BY VARIABLE FREQUENCY WAVES. The top panels show the transient precipitated energy fluxes versus time after the injection of the wave into the magnetosphere at 1000 km altitude for a riser and faller, respectively, with their input formats given in the $f - t$ domain. The bottom panels show the energy of the particles that constitute the corresponding fluxes.

We can infer from Figure 3.6 how particles interacting with the wave at different locations contribute to the time evolution of the precipitated fluxes. Both of the responses are composed of two parts, a high-flux region around the peak and a lower flux region which arrives earlier. The occurrence of a high-flux or peak portion is due to the accumulation of downcoming particles in a relatively wide energy range, as can be understood from the energy curves. In the case of the faller the energy range corresponding to the lower flux portion is narrower than that corresponding to the peak part. This range is even smaller for the case of the riser, thus accounting for the low flux level in the leading part of the precipitation pulse.

The total precipitated energy density obtained by integrating the flux over time is the same for the two cases shown in Figure 3.6. This can be understood on the basis

of the fact that both pulses have the same input energy and the same frequency range, so that they interact with the same ranges of energetic electrons along the field line. It should be noted that this result would not have been obtained if we had not included the wave amplitude variation due to the dispersion of the wave pulse, as discussed in Appendix B.

We have already discussed the locations of the principal interaction regions for variable frequency cases. Referring to Figure 3.6, for the riser the precipitation flux resulting from the interactions near the principal interaction region is significantly lower than that of the main portion of the precipitation pulse. However, for the faller the interactions near the principal interaction region constitute part of the peak flux.

The results of Figure 3.6 were obtained by assuming that the total energy of the propagating pulse is constant everywhere on the field line, i.e., that there is neither wave damping nor growth. It is generally believed that the amplification or growth of monochromatic VLF waves takes place near the geomagnetic equatorial plane. By employing the same physical reasoning, the amplification of variable frequency signals would take place around the phase equator or the principal interaction region [Helliwell and Inan, 1982]. As long as the pulse is long enough (300 ms in this case) such that there is time for the particles to be phase bunched, the input wave might be amplified up to 30 dB as it traverses the principal interaction region [Helliwell and Katsufurakis, 1974]. To study these cases we have computed the precipitation due to amplified waves, and the results are shown in Figure 3.7. The parameters and assumptions used are the same as those used in Figure 3.6 except that the wave intensity is assumed to be 20 dB lower prior to the wave's traversal of the principal interaction region. Thus the energy in the pulses in Figures 3.6 and 3.7 is the same after they pass the principal interaction region, while the input power is 20 dB lower in Figure 3.7 than that assumed in Figure 3.6.

For the riser case given in the left panel in Figure 3.7, only a small portion in the leading edge of the transient precipitation pulse is reduced from that given in Figure 3.6. However, for the faller in the right panel, both the peak flux level and the width in time of the response are significantly reduced in comparison with that in Figure 3.6. The response of the faller between $t = 1$ s and $t = 2$ s is seen to be zero because the pitch angle scattering induced by the 20 dB lower signal is smaller than the resolution ($\Delta\alpha_{eq} = 0.1^\circ$) employed in the computer calculations.

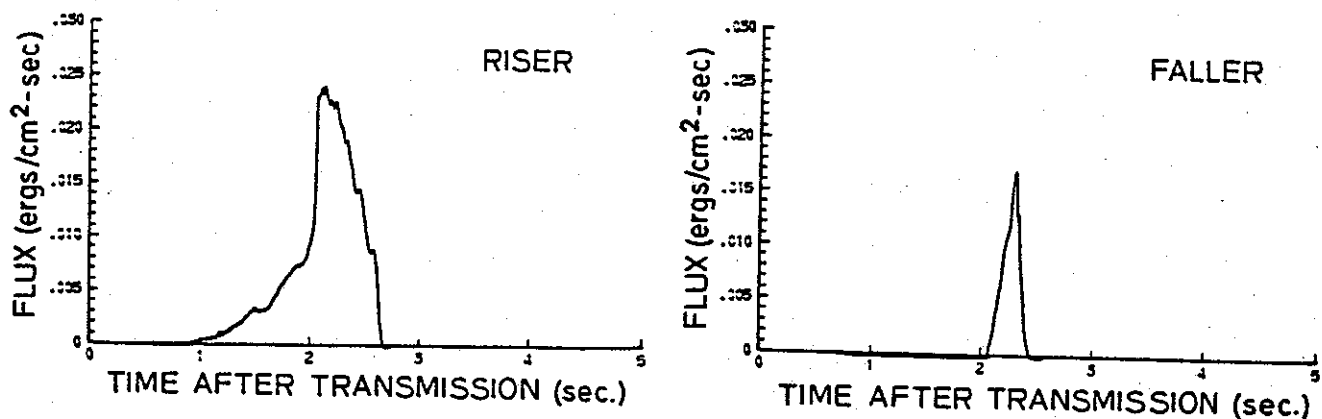


FIGURE 3.7 THE PRECIPITATED ENERGY FLUXES FOR THE SAME INPUT SIGNAL FORMATS AS IN FIGURE 4.3 EXCEPT THAT A 20 DB WAVE GROWTH NEAR THE PRINCIPAL INTERACTION REGION IS TAKEN INTO ACCOUNT.

The results of Figure 3.7 imply that a signal with rising frequency would be more efficient than one with falling frequency in inducing particle precipitation in situations in which signal growth might be present. Note that the same would apply in cases of natural chorus emissions that may be spontaneously generated in the vicinity of the principal interaction region.

The effect of the frequency-time slope df/dt of the input signal on the precipitated flux has been analyzed by *Chang et al.* [1983]. The results showed that under conditions of moderate wave intensities ($B_w < 10$ pT at $L=4$), slowly varying frequencies, and the assumptions that the wave energy is conserved during propagation between the two hemispheres, the total deposited energy density E_T is the same at least to first order for coherent wave pulses having the same input energy and frequency range. Thus for coherent slowly varying signals, E_T is not strongly dependent on the $f-t$ format of the input signal, although the temporal evolution and the peak value of the precipitation flux may vary due to the different combinations of the wave and particle travel times. It was also concluded that for $n \simeq 5$ in (2.28), F_P and E_T become independent of the frequency range of the input wave, being consistent with the result given in the end of the last section that for $f < 0.5f_H$, the energy flux is approximately proportional to $E^{(5-n)/2}$.

IV. APPLICATION OF THE THEORETICAL MODEL

A. INTRODUCTION

When penetrating the lower ionosphere, the precipitated electrons can cause ionization and conductivity enhancements, heating and the emission of X rays and light. Recent experiments have shown an association between isolated bursts of precipitating electrons at middle-latitudes ($L < 6$) and whistlers and triggered emissions. The first observed correlation between discrete VLF waves (propagating at $L \simeq 4.2$) and bursts of bremsstrahlung X rays (> 30 keV) observed at balloon altitudes was reported by *Rosenberg et al.* [1971]. *Helliwell et al.* [1973] reported correlations between whistlers and perturbations in the intensity of fixed-frequency VLF signals propagating in the nighttime earth-ionosphere waveguide. The observed perturbations were attributed to whistler-induced precipitation of energetic (> 30 keV) electrons that cause a transient enhancement of the electron population in the D region and thus perturb VLF propagation in the waveguide. Other related reports include those of *Foster and Rosenberg* [1976], *Rosenberg et al.* [1981], *Lohrey and Kaiser* [1979], *Dingle and Carpenter* [1981], and *Carpenter and LaBelle* [1982]. The work of *Rosenberg et al.* [1981] established a correspondence between VLF chorus at Siple and electron precipitation microbursts at the conjugate Roberval station.

In addition to the X ray and sub-ionospheric VLF techniques, photometric measurements of light emission caused by precipitated electrons have also been employed to explore VLF wave-induced precipitation events. This method provides better spatial resolution of the precipitating particles and is suitable for investigating the effects due to the lower range of the electron energies. *Helliwell et al.* [1980] found one-to-one correlations between bursts of $\lambda \simeq 4278$ Å light emissions and quasi-coherent ducted VLF waves observed at Siple station, Antarctica. *Doolittle and Carpenter* [1983] reported a case of one-to-one correlations between optical emissions and whistler-induced noise events recorded at Roberval.

All of the above mentioned observations of correlation events were attributed to a cyclotron resonance interaction between energetic electrons and whistler-mode wave packets travelling along the earth's magnetic field lines. The interpretation was often based on comparing the measured time lag between the wave and precipitation bursts with the estimated travel times of the wave and the particles from the interaction region to the observation site. The models used have been steadily refined; for example, *Doolittle* [1982] explored the distinction between the effects of

scattered particles that mirror in one hemisphere before precipitation and those that precipitate 'directly'. The previous models also revealed features such as arrival time focusing of particles of different energies and included off-equatorial interactions [Helliwell *et al.*, 1980].

The previous studies and models were largely based on analytical formulations of varying complexity. In general it was not possible to estimate the amplitude or the structure of the precipitation pulse that would be induced by a given wave. The effects of changing frequency or full nonlinear scattering involving relativistic energies were not considered. Although the previous calculations constitute a first order test of the assumed process of cyclotron resonance interactions, in this chapter we apply the test particle computer model of the gyroresonant wave-particle interaction, developed in the previous chapter, for the purpose of computing the precipitation flux level, pulse shape and associated time relationships and comparing these with the reported data.

In addition, recent satellite measurements have shown that electrons in the drift loss cone precipitate from the slot region between the inner and outer radiation zones ($L \sim 2$ to ~ 3.5) and from the outer edge ($L \sim 1.5$ to ~ 1.8) of the inner radiation zone [Imhof *et al.*, 1974, 1981a, b; Vampola and Kuck, 1978; Koons *et al.*, 1981]. The energies of the observed precipitating electrons in these experiments are generally in the quasi-relativistic range of 100 to 500 keV. Detailed study of the spectral characteristics of the precipitating electrons has suggested that these electrons were precipitated by first-order cyclotron resonance interactions with nearly monochromatic waves, possibly from ground based VLF transmitters. In this chapter the theoretical results obtained using the method outlined in chapter II will be compared with the narrow peaks observed in the energy spectra of electrons precipitating from inner radiation belt.

B. APPLICATION TO A LIGHTNING-GENERATED WHISTLER

In this section we apply our formulation to estimate the precipitation induced by a lightning-generated whistler. We consider the case of a whistler originating in the southern hemisphere and propagating northward along the $L=4$ field line. We calculate the transient precipitated flux induced by this simulated one-hop whistler. For simplicity, only that portion of the lightning stroke in the frequency range of 3.5 kHz to 1.0 kHz is considered, as shown in Figure 4.1. The frequency of the leading edge of the propagating whistler packet will always be 3.5 kHz since the

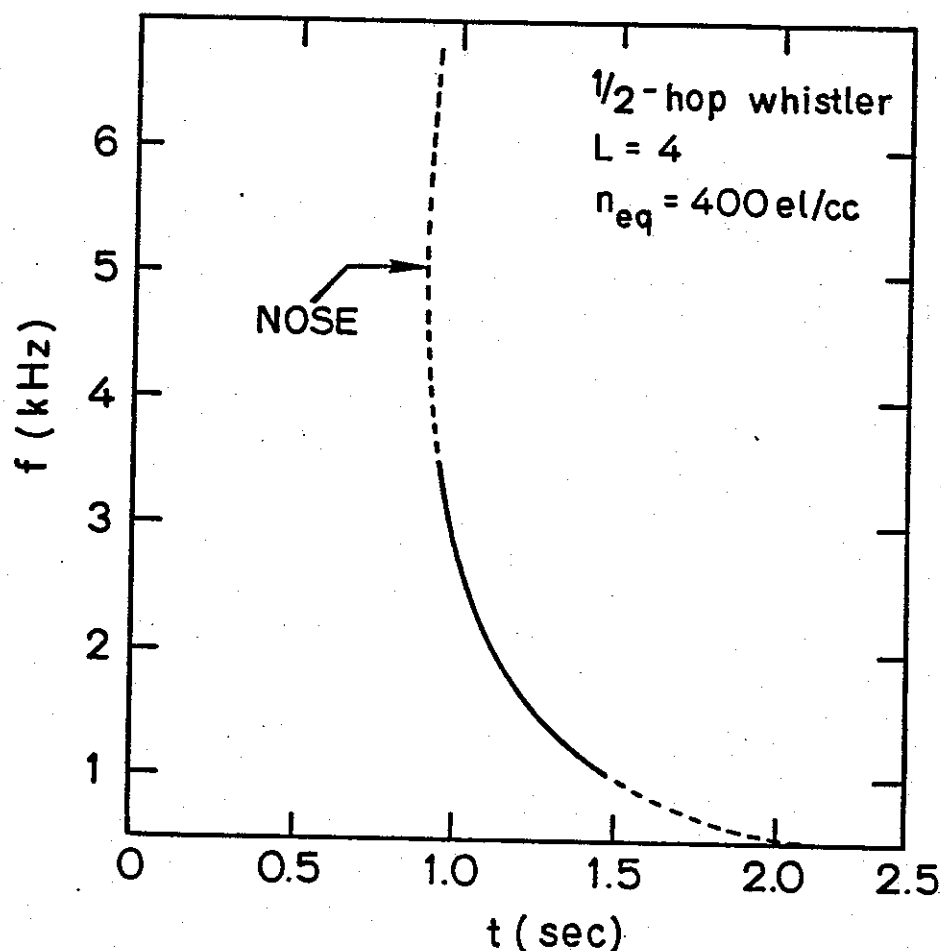


FIGURE 4.1 THE FREQUENCY-TIME FORMAT OBSERVED AT THE EQUATORIAL PLANE OF A LIGHTNING-GENERATED SIGNAL PROPAGATING ON THE $L=4$ FIELD LINE, TERMED A HALF-HOP WHISTLER. The solid segment represent that portion considered in the calculation of particle precipitation.

assumed frequency range is below the nose frequency of 5.05 kHz in our model. The magnetospheric parameters along the $L=4$ line were taken to be the same as in the previous chapter.

The input energy of the lightning impulse is taken as equivalent to that contained in a 0.5-s constant frequency wave pulse at half the equatorial gyrofrequency and having an equatorial wave intensity of 5 pT. As the input lightning-generated wave travels along the field line, the signal is dispersed and the wave magnetic field intensity varies accordingly (see Appendix B). If we observe this whistler at the geomagnetic equatorial plane, the signal format in the $f-t$ domain according to

our model magnetosphere will be that represented by the solid segment in Figure 4.1. The front and tail ends of the wave packet arrive at $t=0.96$ s and 1.49 s, respectively, so the equatorial pulse duration is 0.53 s. The dashed curve in Figure 4.1 shows the arrival times of frequency components other than those considered in our case up to half of the equatorial gyrofrequency. The arrow indicates the nose frequency.

Figure 4.2 shows the resonance velocity curves for a particular particle with equatorial parallel velocity of 1.2×10^8 m/s and at a pitch angle of $\alpha_{eq} = 5.5^\circ$ corresponding to an energy of 47 keV. The dashed curve shows the adiabatic parallel velocity along the field line. Each curve segment in Figure 4.2 starts at the latitude at which the given particle encounters the leading edge of the whistler and ends at the latitude at which this particle exits the whistler wave packet. As the whistler propagates toward the north, it continually meets particles of this given equatorial velocity and the corresponding resonance curve varies from step to step. It is noted that the envelope formed by the starting points of all the v_R curves is the resonance velocity curve corresponding to a constant-frequency wave at the leading frequency of the whistler or 3.5 kHz. Similarly, the v_R curve corresponding to the tail frequency can be obtained by forming the envelope of the end points of the v_R curves. Since the whistler has negative slope in the $f-t$ domain, it is expected that the resonance velocity curves will show zero gradients in some portion of the field line in the northern hemisphere [Helliwell, 1970], as is the case in Figure 4.1. As the whistler propagates and its front end reaches higher latitudes, the minimum in v_R is due to the lower frequency part of the whistler. Since the lower frequency portion has smaller slope, as can be seen from Figure 4.1, the minimum is gradually shifted toward the equator.

Since the resonance point is determined by the intersection of the v_R curve and the $v_{||}$ curve, the particle shown in Figure 4.2 will interact with the whistler between 15° and 25° latitudes. But since v_R varies rapidly in this region, the cumulative pitch angle scattering of the particle is not large in comparison to the interaction at locations where the gradients of the v_R curves are smaller. This has been confirmed by our computation and in fact the parallel velocity and the corresponding energy of this particle, which suffers an equatorial pitch angle scattering less than 0.1° , have been used as the upper limit of the test particle distribution in our calculation. For particles of lower energy, each v_R curve will span a shorter range of latitude due to the smaller parallel velocities; however, its shape will remain qualitatively similar.

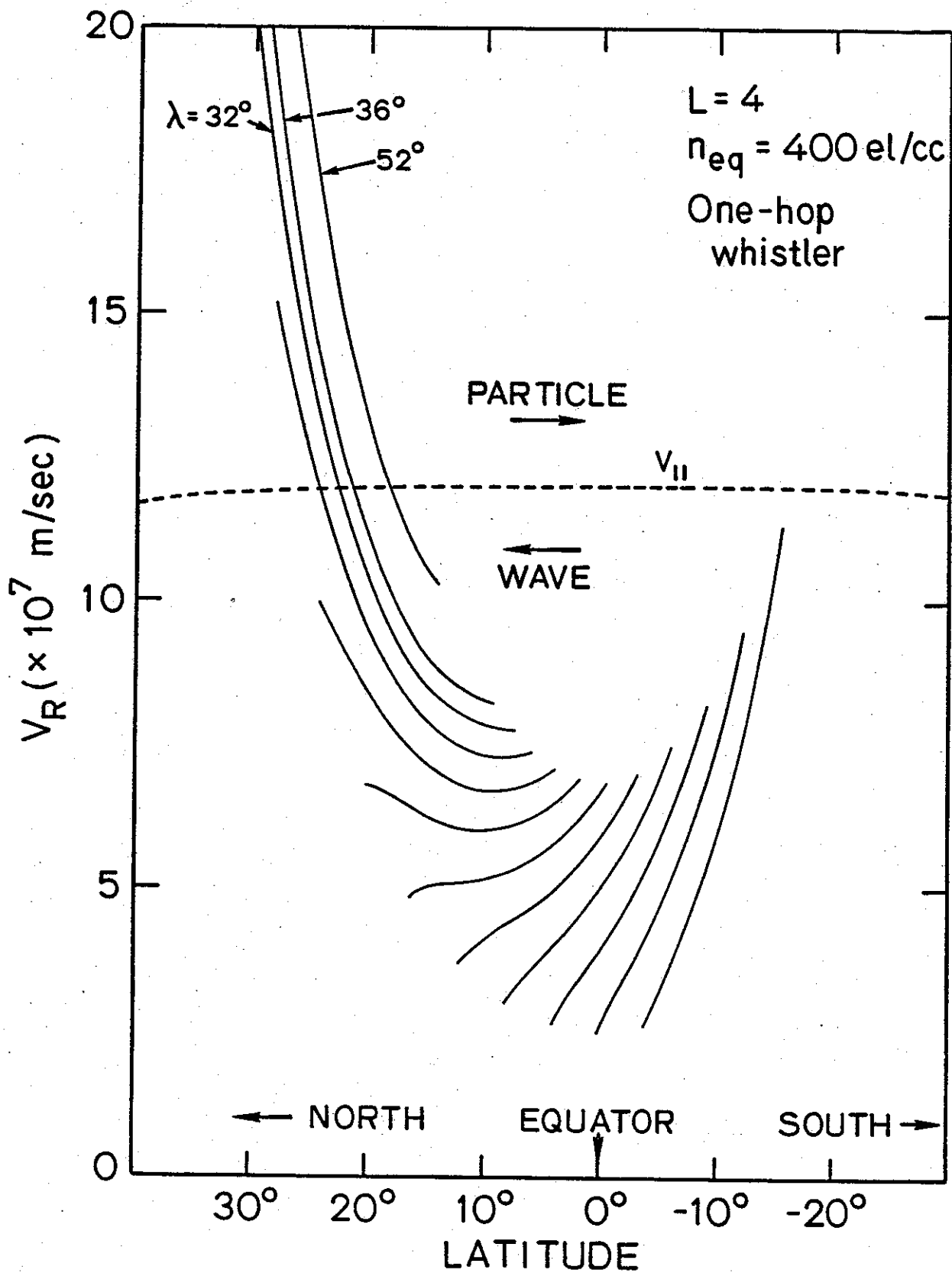


FIGURE 4.2 THE v_R CURVES FOR A PARTICLE WHOSE ADIABATIC PARALLEL VELOCITY IS GIVEN BY THE DASHED CURVE AND THE PROPAGATING WHISTLER SIGNAL DESCRIBED IN FIGURE 4.1.

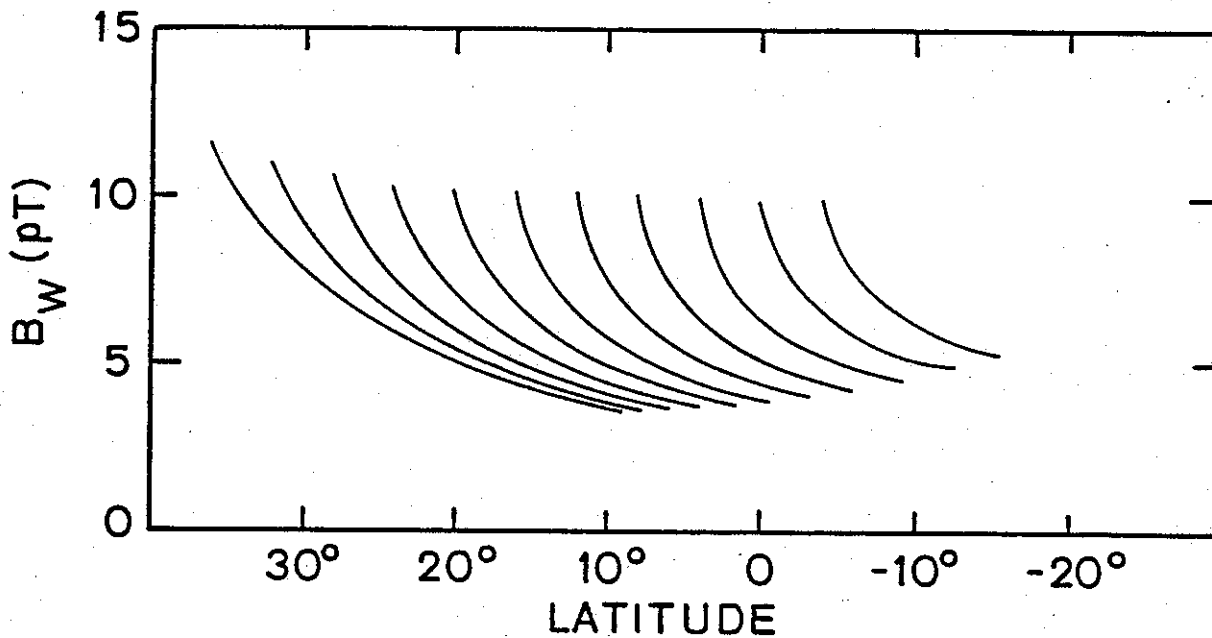


FIGURE 4.3 THE WAVE AMPLITUDE VARIATION VERSUS LATITUDE EXPERIENCED BY THE TEST PARTICLE SHOWN IN FIGURE 4.2 AS IT TRAVELS WITHIN THE WHISTLER WAVE PACKET. Each curve corresponds to a v_R curve in Figure 4.2.

Thus we conclude from Figure 4.2 that particles with parallel velocity (energy) between 5×10^7 (7.3 keV) and 8×10^7 m/s (19.4 keV) will interact strongly with the whistler in the vicinity of 10° latitude in the northern hemisphere and consequently play a major role in the contribution to the precipitation as will be demonstrated later.

Figure 4.3 shows the wave amplitude variation experienced at each step by the test particle shown in Figure 4.2 as it travels within the wave packet. Since the input energy of the lightning impulse is assumed to be uniformly distributed over all frequency components, the lower frequencies have lower wave intensities because of greater dispersion.

The transient precipitation flux induced by this one-hop whistler is shown in Figure 4.4, assuming $n=6$ in (2.28). The energy diagram in the lower panel shows that the energy of the precipitated particles ranges from about 2 keV up to 45 keV. The upper panel indicates that the peak flux arrives about 2 s after the injection of the impulse energy and consists of particles at lower energies as shown in the lower panel. Those particles which were noted to have undergone strong interactions with

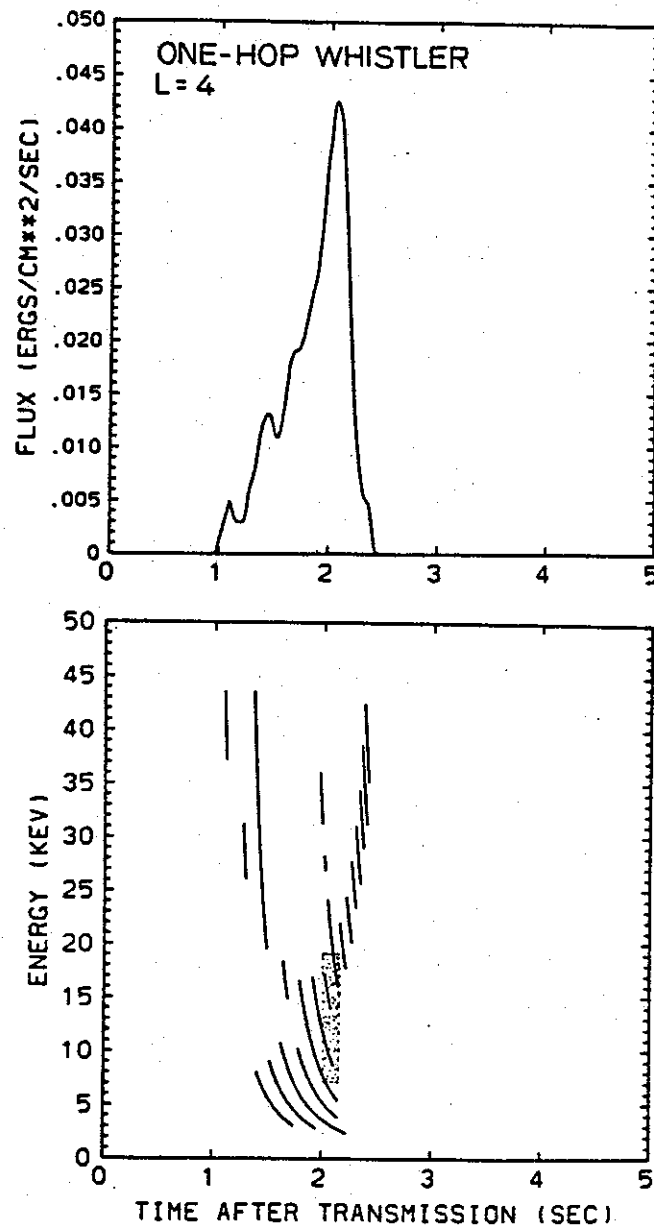


FIGURE 4.4 THE TRANSIENT PRECIPITATION FOR THE WHISTLER DESCRIBED IN FIGURE 4.1. The top panel shows the precipitated energy flux versus time. The bottom panel shows the energy versus arrival time at the wave injection point of the precipitating particles. The shaded region indicates the locations of those particles that undergo strong interactions with the whistler at around 10° latitude in the northern hemisphere.

the whistler at around 10° latitude in the northern hemisphere in the discussion of Figure 4.2 and whose locations in the energy diagram are indicated by the shaded region in Figure 4.4 clearly contribute to the main portion of the precipitated flux.

The integrated energy density E_T induced by this whistler is 0.023 ergs/cm^2 and was shown by *Chang et al.* [1983] to be comparable to that induced by a linear ramp with the same frequency range and the same input wave energy. This result clearly indicates that E_T is primarily determined by the input energy of the wave.

It is interesting to note that substantial leverage is involved in the transient wave-induced precipitation process. For example, in the whistler case the input wave energy is $8.3 \times 10^{-6} \text{ ergs/cm}^2$; comparing with $E_T = 0.023 \text{ ergs/cm}^2$, the leverage is ≈ 3000 . In other words, the energy of the precipitating signal can be and in most cases is much larger than the energy of the wave. This result illustrates the fact that the interacting wave essentially acts as a means for converting particle perpendicular energy into parallel energy (i.e., lowering the pitch angle) with relatively small energy exchange. The precipitated energy then is simply the existing kinetic energy of the radiation belt particles.

C. COMPARISON WITH GROUND BASED OBSERVATIONS

In this section we apply the transient precipitation model to observed correlations reported by *Rosenberg et al.* [1971], *Helliwell et al.* [1973] and *Helliwell et al.* [1980].

The Case of Sub-Ionospheric VLF Perturbations

Helliwell et al. [1973] reported the observation of sudden changes in the amplitude of long-distance sub-ionospheric VLF transmissions in association with whistlers. Sample observations at Eights station in Antarctica of Station NSS (Annapolis, Maryland) on 22.3 kHz showed increases in signal strength that averaged 3 dB. Coincident with every rise a mid-latitude ($L \simeq 2.5$) whistler originating in the northern hemisphere was observed. To explain the association between the whistlers and the changes in VLF signal strength, it was suggested that the whistler precipitates energetic (30–300 keV) electrons into the D region. The resulting ionization then alters the properties of the earth-ionosphere wave guide. The mechanism of precipitation was thought to be pitch angle scattering of trapped electrons that resonate with the whistler wave near the magnetic equator.

Figure 4.5 illustrates the model employed in our calculations. The $L=2.5$ field line with an equatorial electron density of 1800 el/cm^3 and a diffusive equilibrium

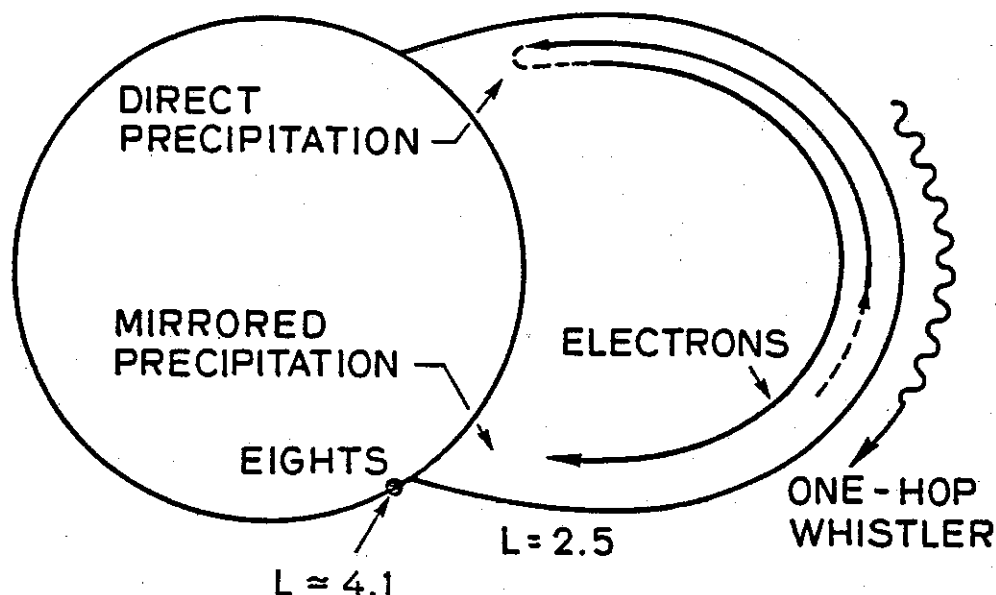


FIGURE 4.5 FIELD LINE MODEL SHOWING THE WHISTLER-INDUCED PRECIPITATION. The one-hop whistler could interact with north-going trapped electrons near the equatorial region and cause precipitation of electrons in the northern hemisphere. Due to the asymmetry in the conjugate mirror altitudes, some resonant electrons can mirror in the north and be precipitated in the south near Eights station.

model for the cold plasma is considered. These values correspond to the strongest whistler trace observed in the correlation events. The input signal in this case is a lightning stroke originating in the northern hemisphere, modeled as having entered the medium at 1000 km altitude at $t=0$. The signal arrives at the southern conjugate point (near the longitude of Eights station) as a one-hop whistler. The whistler interacts with northgoing trapped electrons near the equatorial region and can cause precipitation of some electrons into the loss cone. Due to the asymmetry in the conjugate mirror altitudes at this longitude [Barish and Wiley, 1970], some fraction of the resonant electrons would mirror in the north and thus precipitation in both northern and southern hemispheres is possible.

Frequency-time formats of the whistler propagating at $L=2.5$ are depicted in Figure 4.6. Only the 2–6 kHz portion is considered, being consistent with the observed event in that the strongest whistler signals appeared in this frequency band. The duration of the signal observed at the equator (termed half-hop whistler) is about 0.25 s and in the southern hemisphere (one-hop) is about 0.5 s. The total

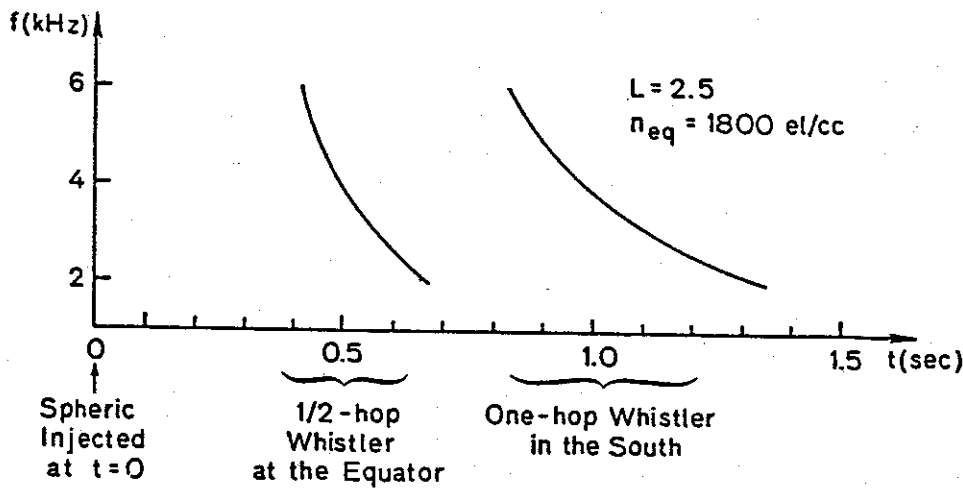


FIGURE 4.6 THE FREQUENCY-TIME FORMATS OF THE WHISTLER USED IN THE COMPUTER MODEL. Only the 2–6 kHz portion was considered, being consistent with the observed event. The duration of the signal observed at the equator (termed 1/2-hop whistler) is about 0.25 s and that of the one-hop whistler received in the southern hemisphere is about 0.5 s.

energy of the wave packet is taken to be that of a monochromatic pulse of duration 0.1 s and equatorial wave intensity of 5pT. The equatorial half angle of the loss cone at $L=2.5$ has been taken as 11.6° in our calculation. Equatorial parallel velocities of 2×10^8 km/s and 1×10^8 km/s are used as the upper and lower limits for the test particle distribution in this case, corresponding to electron energies of 187 keV and 31 keV, respectively.

The calculated transient precipitated energy fluxes induced by this one-hop whistler wave packet are shown in Figure 4.7. Left panels show the direct precipitation fluxes in the north that would be observed after the injection of the impulsive spheric at $t=0$, assuming that all precipitated particles precipitate in the north without either backscattering or mirroring back southward. Three different variations with energy of the trapped particle distributions, i.e., $n=6$, 4, and 2 in (2.28), are used. The differential energy spectrum Φ_E has been normalized to 1.78×10^6 el/cm² s sr keV for $E=40$ keV, corresponding to $\Phi_E = 10^8$ el/cm² s sr keV for $E=1$ keV when $n=4$. For smaller n values, particles with higher energy play a more dominant role. The bottom panel gives the energy range of the precipitating particles at different

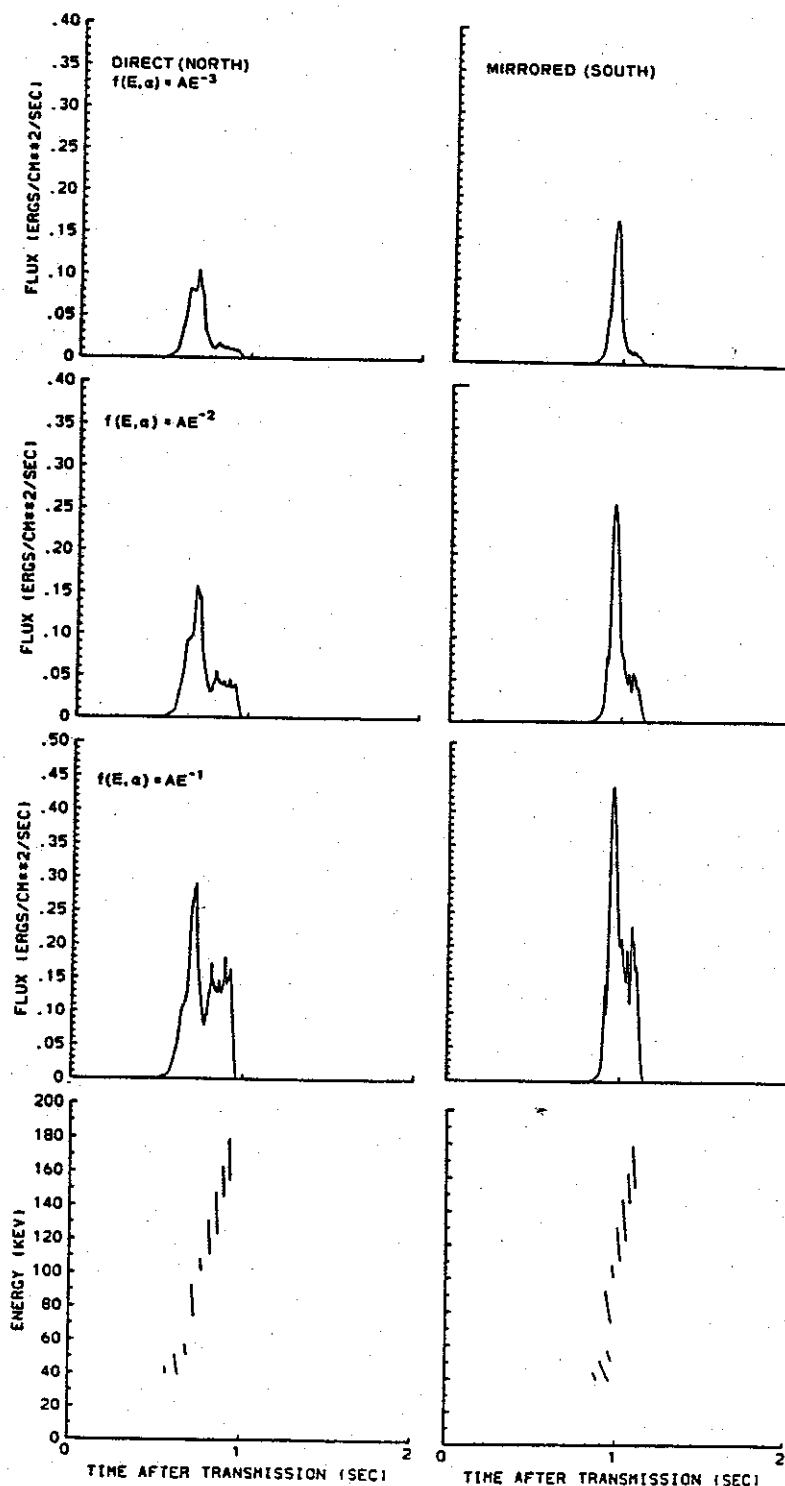


FIGURE 4.7 PRECIPITATION PULSES INDUCED BY THE ONE-HOP WHISTLER GIVEN IN FIGURE 4.6. Left panels show the direct precipitation pulses in the north for three different trapped distributions, assuming no mirrored particles. Right hand panels show the corresponding mirrored precipitation pulses assuming that all precipitated particles mirror back. The bottom panels give the energy versus arrival time curves.

times. One feature in this case is that the faster particles arrive later because they are scattered by the wave at later times.

The right panels of Figure 4.7 give the mirrored precipitation fluxes at the conjugate site assuming that all the scattered particles mirror in the north and precipitate in the south. The total precipitated energies in the direct and the mirrored precipitation cases for a given trapped distribution function are then the same. However, the peak flux of the mirrored case is at least 50 % higher. This is due to the fact that the faster particles catch up with the slower particles, illustrating arrival time focusing of particles with different energies. The energy versus time diagrams indicate that the precipitated electrons are sufficiently energetic ($E > 40$ keV) to penetrate below the normal ionospheric reflecting height for VLF propagation [Banks *et al.*, 1974].

According to Barish and Wiley [1970], a mirror height of 100 km in the south corresponds to a conjugate mirror height of about 500 km along the $L=2.5$ field for the longitude of Eights. This amounts to about 1.2° difference in the half angle of the equatorial loss cone α_{eq}^{lc} between the two hemispheres. It is found from individual test particle trajectories that for the wave intensity of $\simeq 5$ pT used in our model, $\Delta\alpha_{eq} < 1.2^\circ$. In fact, an equatorial wave intensity of > 20 pT would be required for a 2–6 kHz signal at $L=2.5$ to induce a $\Delta\alpha_{eq} > 1.2^\circ$ on at least some of the interacting particles. Therefore, most particles scattered in a single encounter with the wave would be outside the loss cone in the north and would thus mirror back to be deposited in the southern hemisphere. Tolstoy *et al.* [1982] used a propagation model to investigate the effect of localized ionospheric perturbations on the sub-ionospheric VLF wave propagation for the case reported by Helliwell *et al.* [1973]. Their calculations suggest that two ionization regions, one very near the transmitter and another near the receiver, may be needed in order to obtain amplitude increases of > 3 dB. It was suggested that the former was due to transmitter-induced electron precipitation. The one near the receiver would then be due to mirrored precipitation of the type indicated in Figure 4.7. From Figures 4.7 and 4.6 it is seen that the (mirrored) precipitation pulse (< 0.3 s) has a shorter duration than the one-hop whistler packet ($\simeq 0.5$ s), while their average arrival times are about the same.

The results of Figure 4.7 indicate that a precipitated flux of $> 10^{-1}$ ergs/cm² s could be obtained assuming Φ_E of $\simeq 10^6$ el/cm² s sr keV for $E=40$ keV and a wave intensity of $\simeq 5$ pT near the equatorial region. It should be noted that the calculated flux is directly proportional to Φ_E and thus can be scaled up or down

according to different Φ_E 's. Also, in the above calculation an isotropic distribution ($g(\alpha)=1$) has been assumed. For an anisotropic distribution ($g(\alpha) \neq 1$ in (2.28)) peaked around $\alpha=90^\circ$, as discussed in chapter III, another scaling ($g(90^\circ)/g(\alpha_{lc})$) is needed to account for the lower trapped flux level near the edge of the loss cone since we use Φ_E at 90° pitch angle as the reference. Although Φ_E is an unknown factor in the present case, we know that the observation took place under relatively quiet geomagnetic conditions and it is useful to estimate the possible precipitated flux level by using typical quiet time values for Φ_E . Under these conditions, according to Lyons and Williams [1975], $\Phi_E \simeq 10^5$ el/cm² s sr keV at 90° pitch angle and $g(90^\circ)/g(\alpha_{lc}) \simeq 10$ for $E=40$ keV and $L \simeq 3$. Then our computed flux level would be scaled down to $\sim 10^{-3}$ ergs/cm² s. Moreover, when strong anisotropy in the vicinity of the loss cone rather than a sharp-edged loss cone is considered, a further reduction in flux by an order of magnitude might be necessary as discussed in chapter III.

The X Ray Case

The first one-to-one correlation between short bursts of bremsstrahlung X rays ($E > 30$ keV) and bursts of VLF discrete emissions was obtained on January 2, 1971 during balloon-borne measurements at Siple station, Antarctica [Rosenberg et al., 1971]. This correlation was interpreted in terms of a cyclotron resonance interaction in the vicinity of the geomagnetic equator and suggested that the wave-induced energetic electron precipitation would create the observed X rays. From an examination of the ground based VLF recordings, it was determined that the waves led the arrival of the precipitating electrons by about 0.3 to 0.4 seconds.

It was found that every major burst of X rays was associated with VLF rising tones of duration $\simeq 0.5-3$ s. The rising emissions were deduced to be triggered by whistlers from lightning discharges in the northern hemisphere. The triggering region was presumed to be near the geomagnetic equator on the downstream side for the particles. Two possible situations could cause precipitation of particles at Siple station: a north-going wave could scatter south-going electrons into the loss cone and result in direct precipitation, while a south-going wave could also scatter north-going electrons which then mirror in the north and result in mirrored precipitation in the south. For the case in hand, the mirrored precipitation was found to provide a better explanation than direct precipitation based on the analysis of wave and particle travel times. [Rosenberg et al., 1971].

Figure 4.8 shows a schematic description of the reported correlation event of January 2, 1971. A south-going wave packet of VLF emissions triggered near the

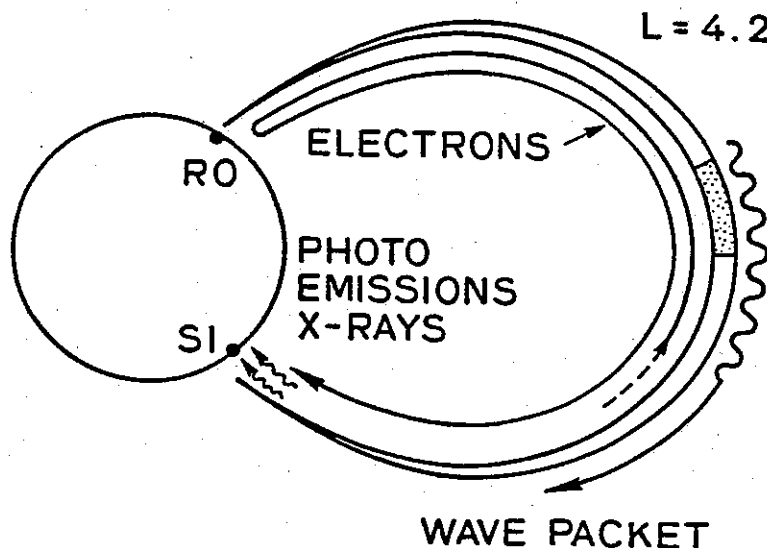


FIGURE 4.8 SCHEMATIC SHOWING THE PATHS OF SCATTERED ELECTRONS AND THEIR PRECIPITATION EFFECTS. VLF emission signals triggered near the equator along the Siple-Roberval field line can scatter north-going electrons which mirror above Roberval and then precipitate over Siple station where they cause X rays and photo emissions.

equator scatters north-going electrons which mirror above Roberval and precipitate above Siple station, generating bremsstrahlung X rays. Such mirrored precipitation is possible due to the asymmetry in the conjugate mirror altitudes for the Roberval-Siple field line.

In our model calculation, a rising ramp with frequency varying from 2 to 4 kHz is injected onto the $L=4.2$ field line above Roberval at 1000 km altitude at time $t=0$, such that the signal received at Siple would be a rising ramp with duration of 0.5 s. To account for the triggering of the observed emissions near the equator, the wave intensity of the input signal is assumed to be zero in the northern hemisphere along the field line, while it is taken to be that corresponding to a 5 pT equatorial intensity in the region to the south of the equator. The mirrored transient precipitation energy flux above Siple is then obtained as a function of time after the injection of the input signal, assuming that all the scattered particles would mirror above Roberval. Since the bursts of X rays that were correlated with the waves had energies >30 keV, and were mainly caused by electrons with energy >60 keV [Rosenberg et al., 1971; Foster and Rosenberg, 1976], we have calculated the fluxes due only to particles with $E > 60$ keV. On the Siple-Roberval field line a mirror height of 100 km in

the south corresponds to a conjugate mirror height of 280 km [Barish and Wiley, 1970]. In this case, our test particle calculations show that more than 95% of the precipitated particles mirror at the northern end, since $\Delta\alpha_{eq}$ experienced by most of these high energy ($E > 60$ keV) particles is smaller than the difference (about 0.2°) in the equatorial half angle of the two loss cones. The above assumption that all electrons mirror back is then a good approximation. It is worth noting, however, that this pitch angle difference due to mirror height asymmetry is easily overcome in the case of higher intensity waves, so that particles can be precipitated directly in the northern hemisphere. The saturation level of wave fields outside the plasmopause could be higher than that inside the plasmopause [Helliwell and Inan, 1982]. In fact, particle precipitation effects due to VLF signals propagating southward just outside the plasmopause have been observed using X ray detector [Rosenberg et al., 1981] and photometer [Doolittle and Carpenter, 1983] at Roberval, Canada. The wave intensity is less critical for the photometric detection since the photometer is sensitive to the effects of lower energy electrons that can suffer larger pitch angle changes.

The equatorial electron density n_{eq} on the $L=4.2$ field line at the time of the observed correlation was estimated through whistler scaling to be 25 ± 12 el/cm³. In this case we compute the precipitated fluxes for $n_{eq}=13, 25$ and 37 el/cm³. Although the above estimation was based on a collisionless model [D. L. Carpenter, private communication], both diffusive equilibrium and collisionless models of the cold plasma distribution along the field line have been considered in our calculation. In Figure 4.9 is plotted the time lag between the peak of the flux and the arrival of the wave front as a function of n_{eq} for both the diffusive equilibrium and collisionless models. The shaded area indicates the observed time lag in the experiment. Our theoretical results based on the collisionless model and $n_{eq} \simeq 25$ el/cm³ are in good agreement with the observations.

The Photoemission Case

One-to-one correlations were observed at $L \simeq 4.2$ between bursts of VLF noise in the $\simeq 2$ to 4 kHz range and optical emissions at $\lambda \simeq 4278$ Å at Siple station in the austral winter of 1977 [Helliwell et al., 1980]. The correlated VLF wave activity usually consisted of clusters of discrete rising tones or chorus. In the case of July 24, 1977 all of the correlated wave events involved whistlers and whistler-triggered emissions. In this particular case, the length of the wave train observed at Siple was estimated to be about 1.2 s, and the observed photometer pulse was found to occupy

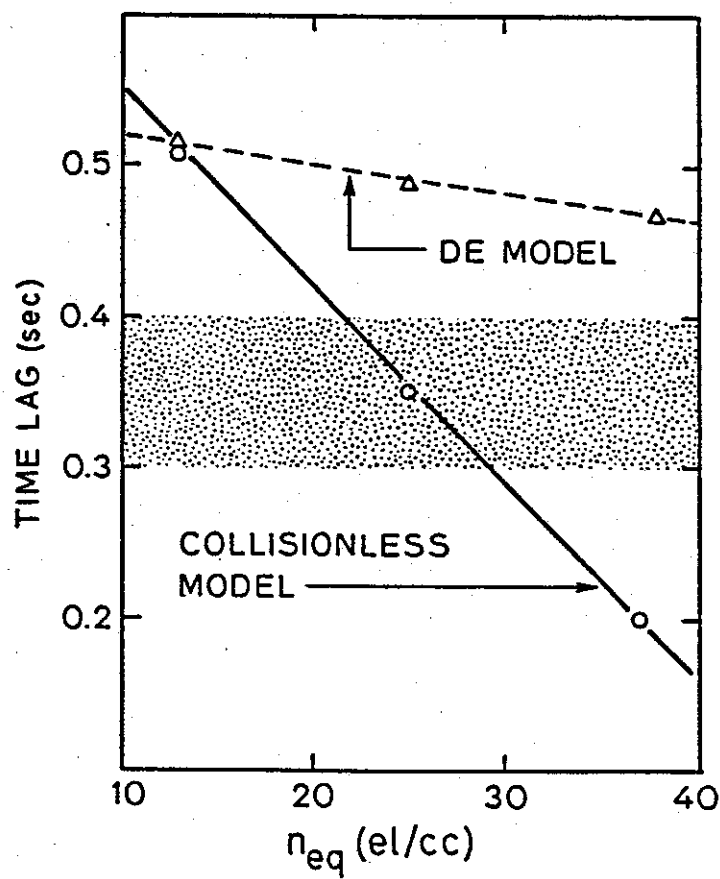


FIGURE 4.9 TIME LAG BETWEEN THE PEAK OF THE FLUX AND THE ARRIVAL OF THE WAVE AS FUNCTION OF n_{eq} FOR DE AND COLLISIONLESS MODELS. The shaded area indicates the observed time lag.

the time interval 2.6 to 4.3 s after the occurrence ($t=0$) of the lightning-generated spheric observed near Roberval. For propagation at $L \simeq 4.2$, the equatorial cold plasma density and the equatorial wave magnetic field were found to be $n_{eq}=100$ el/cm³ and $B_w \approx 8$ pT, respectively.

The field line model for this photometer case is the same as that depicted in Figure 4.8. As in the X ray case discussed in the previous subsection, both direct and mirrored precipitations are candidates that may account for the optical emissions over Siple station. The possible importance of direct precipitation is suggested by the fact that at the top of the ionosphere the field intensity of the north-going wave was estimated to be only 2 dB less than that of the south-going wave [Helliwell *et al.*, 1980], thus indicating re-triggering or efficient echoing of the wave back and forth between hemispheres.

We have calculated both the direct and mirrored precipitation fluxes induced by the wave event corresponding to the case of July 24, 1977. The signal received at Siple is modeled as a rising ramp with duration of 1.2 s and with frequency varying from 2 to 4 kHz. For the mirrored case in which the wave is south-going, the wave intensity in the northern hemisphere along the field line is taken to be zero to account for the fact that the whistler-induced emission was probably generated near the equator, while it is taken to be 8 pT to the south of the equator in accordance with the estimation from the data. However, for the case of the north-going wave that causes direct precipitation, the wave intensity is taken to be 8 pT on both sides of the equator. It should be noted that if the northgoing wave resulted from re-triggering near the equator, the wave intensity in the southern hemisphere should be taken to be zero. We have, however, found that this different choice of wave distribution does not change the main portion of the precipitation pulse. A diffusive equilibrium model is used for the cold plasma distribution along the $L=4.2$ field line with $n_{eq}=100$ el/cm³. Our results [Chang and Inan, 1983] show that the direct precipitation case gives a slightly better fit to the data based on the arrival time interval of the flux. However, the significant overlap in time between the two responses suggests that both the mirrored and direct precipitation may be contributing to the observed flux.

As mentioned in the introduction, in order to account for all the particles that could contribute to the observed photoemission, a wide range of particle energies needs to be considered. The pitch angle resolution in this case is $\Delta\alpha=0.05^\circ$ so that particles with energies up to $\simeq 180$ keV, which have the maximum scattering in this order, are included. The calculated flux level is a function of B_w and the assumed

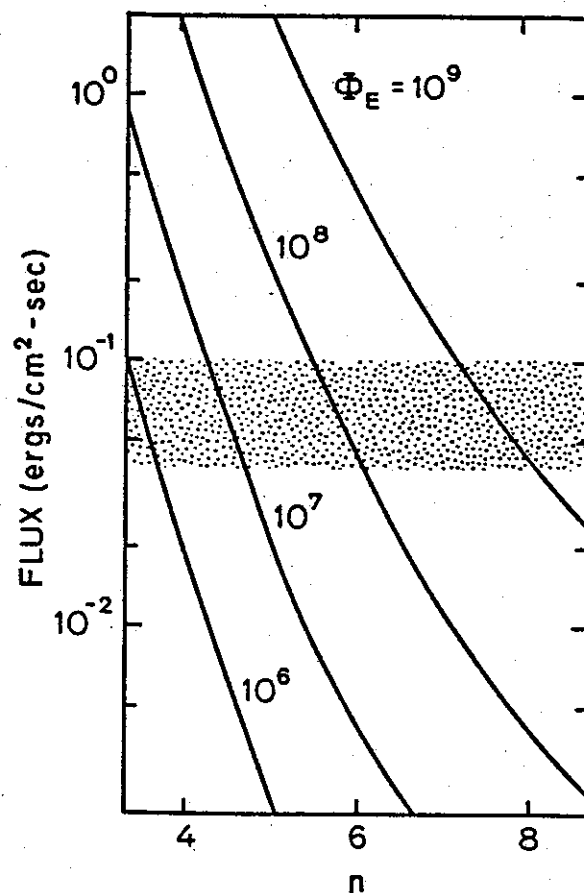


FIGURE 4.10 PEAK FLUX LEVEL VERSUS n IN EQUATION (2.28) WITH Φ_E AS A PARAMETER FOR THE CASE OF DIRECT PRECIPITATION FOR THE PHOTOMETER CASE. The shaded area indicates the range of the precipitated energy fluxes inferred from the data.

trapped particle distribution. In the present case, B_w has been inferred from the data. The assumed particle distribution is then the main factor that determines the computed flux level. For a case in which the particle energy covers a wide range as in this one, the value of n in (2.28) is the key parameter that affects the relative contributions to the flux of high and low energy particles. For fixed n , the energy flux level is proportional to Φ_E . In Figure 4.10, we plot the peak flux level versus n with Φ_E as a parameter for the case of direct precipitation. The shaded area indicates the range ($\simeq 0.04$ – 0.1 erg/cm² s) of the precipitated energy fluxes inferred from the photometric data [Helliwell *et al.*, 1980]. If $\Phi_E = 10^8$ el/cm² s sr keV for $E=1$ keV then $n \simeq 5.5$ – 6 would fit the observed downcoming flux. However, if Φ_E is reduced by two orders, n would be less than 4. Figure 4.10 implies that under typical flux levels of $\Phi_E = 10^6$ – 10^8 el/cm² s sr keV [Lyons and Williams, 1975] the value of n would fall in the range of $\simeq 3.5$ to 6 based on the observed precipitating fluxes. To the best of our knowledge, this constitutes a new method of remotely estimating the decrease with energy of the trapped particle distribution in the magnetosphere. Our estimated value of $n \simeq 3.5$ to 6 is in substantial agreement with published direct measurements [Schield and Frank, 1970]. Since the above results are obtained by assuming $g(\alpha)=1$ in (2.28), inclusion of any anisotropy would reduce the calculated fluxes as discussed in the case of sub-ionospheric VLF perturbations and therefore would result in smaller estimated n 's, or a less steep distribution with respect to E .

D. COMPARISON WITH SATELLITE OBSERVATIONS

In this section we adopt the method outlined in sections E and F of chapter II to compare our model results with satellite based observation of energetic electron precipitation.

Data for Comparison

Recent satellite experiments have shown that the energy spectra of electrons precipitating from the inner radiation belts contain peaks having central energies which decrease with increasing L value [Vampola and Kuck, 1978; Koons *et al.*, 1981; Imhof *et al.*, 1981a, b]. This observed characteristic suggests that the precipitation may be due to first-order cyclotron resonance interaction of the trapped electrons with monochromatic waves near the magnetic equator. The electrons involved in these interactions had to be precipitated into either the drift loss cone or the local bounce loss cone due to pitch angle scattering by the waves. The observed energies of the precipitating electrons were generally in the range of 100 to 500 keV.

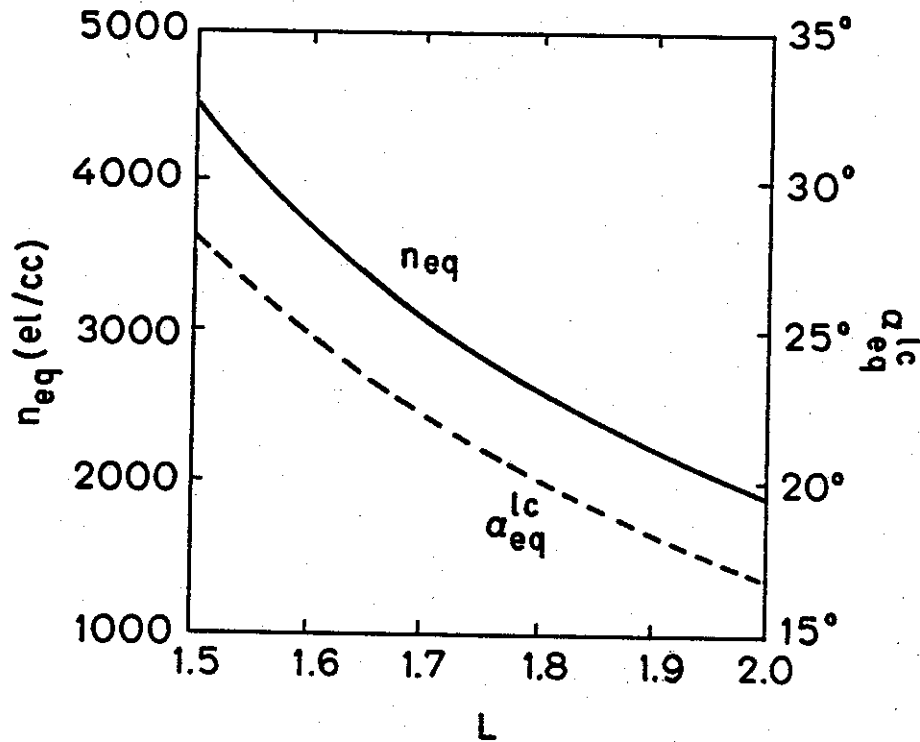


FIGURE 4.11 THE EQUATORIAL COLD PLASMA DENSITY AND THE EQUATORIAL BOUNCE LOSS CONE AS FUNCTIONS OF L VALUE USED FOR THE RESULTS SHOWN IN FIGURE 4.12. The equatorial cold plasma density is proportional to L^{-2} .

In the following we compare these observed narrow peaks in the precipitated energy spectra with our theoretical predictions. It should be noted that the precipitating electrons which were observed in the drift loss cone might have interacted with the wave near the equatorial region a large number of times during their bounce motions while drifting across a longitude sector. The total pitch angle scattering accumulated from all such individual interactions must thus have been large enough to be observed. We argue here that the spectral content of the precipitating electrons resulting from the cumulative interactions would be similar to that due only to one-pass interaction since the energy changes of these near-loss-cone particles after being pitch angle scattered have been found to be negligibly small compared to their unperturbed energies under conditions of moderate wave intensities. Therefore, the calculations of one-pass scattering of the test particles at the edge of either the drift loss cone or the bounce loss cone will reveal much of the spectral properties of the precipitating electrons.

For our comparison, we choose the data for June 16, 1979, presented by *Imhof et al.* [1981b] for comparison with our theoretical study. For this day, seven energy spectra at selected L shells from $L \sim 1.57$ to $L \sim 1.75$ were presented. We select three of these spectra, corresponding to $L \sim 1.57$, 1.65, and 1.75, with peak resonance energies of 277, 200, and 120 keV, respectively. It was suggested that a strong monochromatic wave at ~ 23 kHz measured by plasma wave experiments may have caused the sharp peaks in these spectra [*Imhof et al.*, 1981b]. To derive the equatorial cold plasma densities from the observed peak resonance energies, the waves were assumed to be traveling parallel to the magnetic field lines. For this set of data it was found that the plasma density profile varies as L^{-3} , being consistent with the plasma densities derived from the measured upper hybrid resonance frequencies. From the extrapolated profile the equatorial plasma density corresponding to $L=1.5$ on this day is found roughly equal to 4500 el/cm^3 . In our calculation we used this estimated value at $L=1.5$ as a reference and assumed an L^{-3} dependence as shown in Figure 4.11. Also shown in Figure 4.11 is the value of the equatorial bounce loss cone as a function of L . The loss cone angles are derived from the dipole magnetic field model by taking a mirror height of 100 km. Although propagation is likely to be nonducted in the low- L shell regions, we have assumed ducted longitudinal propagation for purposes of comparison. The equatorial wave amplitudes in all three cases were taken to be 5 pT. This value is within the range of typical intensities of signals from ground based VLF sources as measured on satellites [*Scarabucci*, 1969; *Inan et al.*, 1977].

Model Calculations

Having established the magnetospheric parameters for our computations, we present in Figure 4.12 the computed rms pitch angle scattering versus energy of the near-loss-cone particles induced by one-pass interactions with the 23-kHz waves for the three selected cases. The results are shown in a format similar to that of Figure 2.12. For cases of lower equatorial resonance energy in Figures 2.12 and 4.12 the peak scattering is larger while the absolute width of the peak in keV is narrower. The differences in peak width of the rms scattering for the different cases can be attributed to the same factor as discussed in connection with Figure 2.12. The peak energies corresponding to $L=1.57$, 1.65, and 1.75 cases in Figure 4.12 are 257, 187, and 126 keV, respectively; these are not exactly equal to those observed by *Imhof et al.* since the cold plasma densities deduced by them are only approximately equal to the extrapolated densities that we have used. However, this obviously will have little effect on our results.

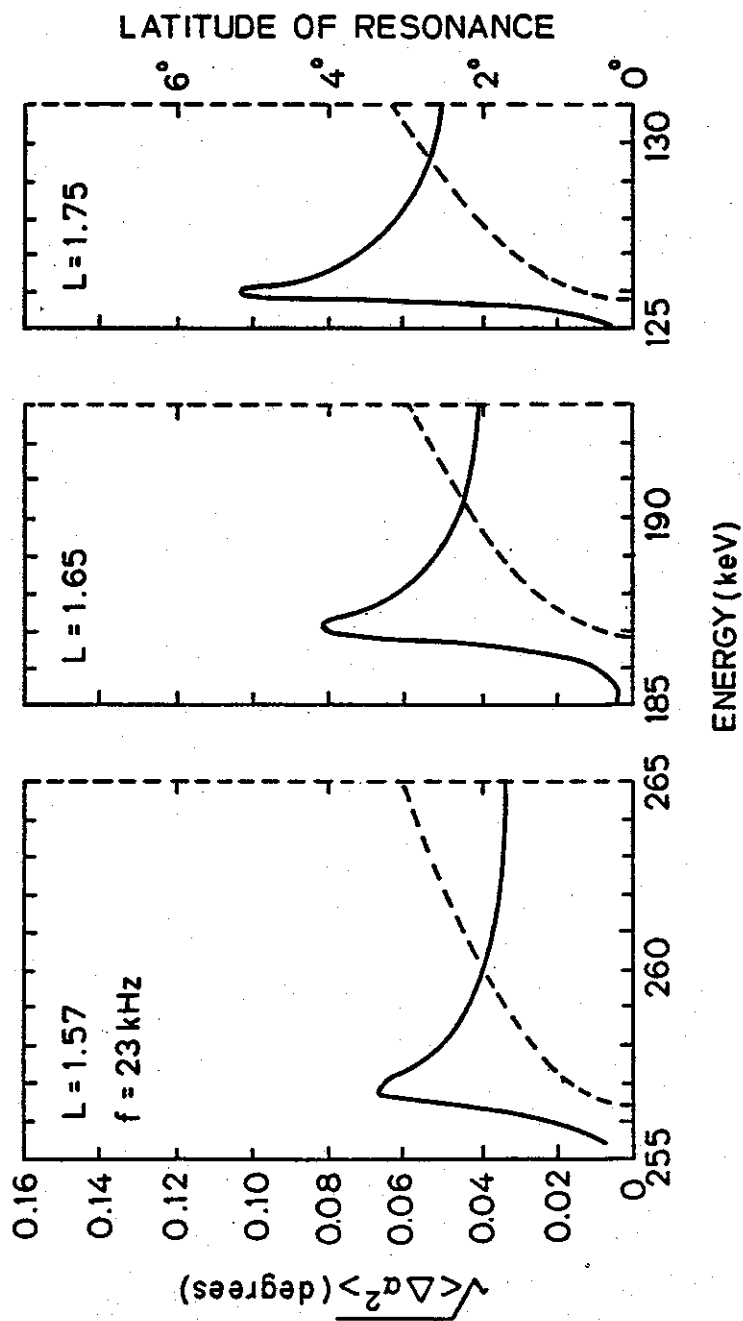


FIGURE 4.12 THE ENVELOPE OF RMS SCATTERING PATTERN VS. ENERGY FOR THE NEAR-LOSS-CONE PARTICLES RESULTING FROM ONE-PASS INTERACTIONS WITH A 23-KEV WAVE ON THREE DIFFERENT L SHELLS. The dashed curves show the latitude of resonance versus energy.

The rms pitch angle changes in Figure 4.12 drop to about one half of the maximum value when the latitude of resonance moves $\sim 3^\circ$ from the equator for all three cases. The resonance energy corresponding to this latitude is less than 10 keV above the equatorial resonance energy in each case. Thus, in terms of our definition of FWHM the peak width is less than 10 keV. For our computations we have assumed a monochromatic wave with equal intensity on both sides of the equator, and the conjugate resonances have been treated as phase-correlated. In the presence of other electromagnetic turbulence, however weak it may be, the dephasing of the two resonances would occur at some latitude above the equator. The resulting smearing out of the interference pattern in rms scattering would cause the total scattering to drop to a lower level and possibly a reduction in the effective peak also.

We have shown in chapter II that the peak width in energy of the precipitation flux is generally less than that of the rms scattering. Referring to Figure 4.12 and the above discussion, the theoretical peak width of the precipitated energy spectra will thus be less than ~ 10 keV for the cases shown. As reported by *Imhof et al.* [1981a, b], in some cases the electron energy spectra have FWHM values of the order of 30 keV, which represent upper limit values since they include contributions from the instrument resolution. Widths as narrow as ~ 20 keV or less could be derived after the instrument resolution is unfolded. Therefore, our theoretical estimation of peak widths is within the possible upper limit values obtained from the experiments. Note that we have assumed a monochromatic wave with a sharply defined wave normal angle at 0° . Therefore the estimated peak results from the dependence of the interaction strength on the latitude of resonance only.

In the following we consider other possible effects which might cause the widening of the observed peaks and thus confirm the presumption that equatorial interactions at these low L shells would produce narrow peaks in the spectra of the precipitating electrons.

Discussion

While our model results show agreement with those of *Imhof et al.* [1981a, b], comparison with experimental results is complicated by a number of factors. One is the angular spread of the wave normals in the general case of nonducted propagation.

The parallel resonance velocity expressed by equation (2.22) applies only to longitudinally propagating waves. For a first-order correction for oblique propagation

with \mathbf{k} at an angle θ to the static magnetic field, the k in (2.22) has to be replaced by $k(\theta) \cos \theta$, which is the component of \mathbf{k} along the magnetic field line, where $k(\theta)$ is the magnitude of \mathbf{k} , a function of θ . Note that k is proportional to the refractive index μ , i.e., $k = (\omega/c)\mu$. For cases of Figure 4.12 the equatorial refractive index would increase from 8.30 to 8.48 as L varies from 1.57 to 1.75 under the cold plasma distribution given in Figure 4.11. If we take the angular spread of wave normals to be within $\pm 30^\circ$ with respect to the direction of longitudinal propagation, the range of the corresponding equatorial refractive index variation is found to be within $\sim 6\%$ below the equatorial refractive index for the longitudinally propagating wave. The broadening in the equatorial energy bands of electrons effected by this wave normal spread would be approximately 23 keV, 17 keV, and 12 keV for $L=1.57$, 1.65, and 1.75, respectively.

One interesting feature revealed by our results is the asymmetry in the rms scattering versus energy curve with respect to the peak. As pointed out in chapter II in connection with Figure 2.13, the strength of scattering decreases rapidly for particles with energy below the equatorial resonance energy. If this asymmetry could be detected experimentally, it might be used as an additional test of whether or not the peaks of the precipitated energy spectra are due to wave-particle interactions involving monochromatic waves.

E. DISCUSSION

In this chapter we have attempted to apply our theoretical formulation to the parameters of various cases of ground or satellite based observations of wave-induced precipitation events. In comparing our results, various limitations of the model and its dependence on various parameters must be considered. In the following we discuss the effect on our results of (i) the wave structure and intensity variation and (ii) the energetic electron distribution.

The Wave Structure and Intensity Variation

The interaction model studied in this report has been limited to the case of longitudinally propagating whistler mode wave as described by (2.7). In calculating the electron pitch angle scatterings and wave-induced perturbations of the energetic electron population, we have assumed that the wave structure is known as a function of space and time and have not directly included the effects on the wave of the electromagnetic fields generated by the perturbed particles. This amounts to, in

effect, assuming that the fields radiated by the perturbed particles are negligible, as in the case of an unamplified wave, or that this effect has been included in the model chosen for the wave structure.

To indirectly account for the effect of wave growth in some cases (e.g., Figure 3.6), we have presumed that the signal undergoes an amplification of at least 20 dB across the principal interaction region. Experimental and theoretical evidence suggest that the region of temporal growth is within a few degrees of the geomagnetic equator for the monochromatic waves [Helliwell, 1967; Helliwell and Katsufakis, 1974]. Any change in the wave amplitude structure will thus occur over a relatively small portion of the field line [Helliwell and Inan, 1982]. The effect of such a nonuniform amplitude variation on the total precipitated flux can be indirectly accounted for by choosing a suitable wave structure.

The wave amplitude variation along the field line within a whistler mode duct due to the dispersion and the inhomogeneous nature of the medium is discussed in connection with (2.8) and in Appendix B. We have found that this consideration is essential in the calculation of precipitation due to variable frequency signals.

We have considered cases of moderate wave intensities (e.g., $B_w \leq 10$ pT at $L \simeq 4$) in most of the calculations in this report. It has been demonstrated that for this range of wave intensities and for the parameters used, the precipitated flux is linearly proportional to B_w [Inan *et al.*, 1982]. The results presented in this report can thus be directly scaled up or down for estimating the precipitated flux levels induced by waves with given intensities in this range. The typical unamplified intensities of manmade VLF transmitter signals in the magnetosphere fall in this range [Inan *et al.*, 1977; Bell *et al.*, 1981; Tsuruda *et al.*, 1982]. However, the signal level might be higher after amplification and triggering. For example, for natural emissions, such as VLF chorus, measured wave intensities have been reported to be in the range of 1–100 pT [Burtis and Helliwell, 1975]. For such higher field intensity cases the trapping of particles may play a more significant role so that the precipitated flux can not simply be scaled up or down proportionally with B_w . However, our existing formulation can easily be applied to such cases.

Energetic Electron Distribution

We have considered initial trapped electron distribution functions as defined by (2.28). The coefficient A in (2.28) is proportional to the differential energy spectrum Φ_{E_0} of the trapped particles, as given by (2.29). By proper choice of $g(\alpha)$, n , and Φ_{E_0} ,

one can match the function defined by (2.28) to most observed energetic electrons in the magnetosphere.

In most of our calculations we have used $\Phi_{E_0} = 10^8$ el/cm² s sr keV for electrons with energy $E_0=1$ keV and at $\alpha=90^\circ$ pitch angle. This value is typical of the flux levels outside and just inside the plasmapause during geomagnetically disturbed times [Schield and Frank, 1970; Anderson, 1976] and was the reference flux level used in previous work [Inan et al., 1978]. Under other conditions, for instance, relatively quiet geomagnetic period, Φ_{E_0} could be as low as 10^5-10^6 el/cm² s sr keV [Lyons and Williams, 1975]. We have also chosen to present our results with the assumption that Φ_{E_0} is constant with L , although Φ_{E_0} has been observed to be a highly variable quantity. The precipitated energy fluxes given in this report are directly proportional to Φ_{E_0} . Thus, for any realistic variation of Φ_{E_0} as a function of L or for any other values of Φ_{E_0} , the precipitated flux values can be obtained from the results given by proper scaling.

For most of the results presented in this report we have used an isotropic distribution for which $g(\alpha)=1$ in (2.28). It should be noted that pitch angle isotropy over the atmospheric bounce loss cone can only be maintained under strong diffusion conditions [Kennel, 1969] and anisotropic distributions are more likely to occur in the magnetosphere [Lyons and Williams, 1975]. For anisotropic distributions peaked around $\alpha=90^\circ$, and for which $g(\alpha)$ is flat for a few degrees above the loss cone, the calculated flux values would be reduced by a factor $(g(90^\circ)/g(\alpha_{lc}))$, as discussed in chapter III. Moreover, when strong anisotropy in the vicinity of the loss cone rather than a sharp-edged loss cone is considered, a further reduction in precipitated flux levels might be necessary [Inan et al., 1982].

V. SUMMARY AND RECOMMENDATIONS

A. SUMMARY

We have employed a test particle computer simulation approach to study the cyclotron resonance interaction between radiation belt energetic electrons and coherent whistler mode VLF waves propagating longitudinally along the static magnetic field lines in the magnetosphere. We have concentrated on the wave-induced pitch angle scattering of near-loss-cone trapped electrons and their precipitation into the ionosphere.

In order to be able to study interactions involving electrons with quasi-relativistic energies of up to hundreds of keV, we have rewritten the equations of motion for the cyclotron resonance wave-particle interaction by taking into account relativistic effects. Our simulation model is then based on these generalized equations and the relativistic cyclotron resonance condition. It was suggested that the relativistic formulation be used for particle energies higher than 50 keV, corresponding to a 10% correction in average pitch angle scattering with respect to the nonrelativistic formulation.

We have computed the root mean square (rms) pitch angle scattering of the near-loss-cone quasi-relativistic electrons and the corresponding precipitated energy spectrum due to wave-particle interactions occurring near the equatorial plane. It was shown that although the energy spectrum of the precipitated flux is strongly dependent on the assumed trapped electron distribution, the full width at half maximum of the rms scattering pattern would give an upper bound to that of the energy spectrum. These peak widths were compared with and demonstrated to be consistent with those measured by recent satellite experiments. The results indicate that the L -dependent narrow peaks observed by satellite particle detectors could indeed be caused by wave-particle interactions involving monochromatic waves from ground based VLF transmitters.

Based on the test particle simulation method, we have developed a computer model for determining the detailed time evolution of the transient precipitated energy flux induced by short-duration VLF waves propagating along the geomagnetic field lines. The main purpose of this study is to provide a theoretical basis for experiments designed to detect precipitation induced by discrete coherent VLF waves, for instance, the signals injected from the Siple transmitter. The computer

model is useful in examining the characteristic shape of the wave-induced precipitation pulse under a wide range of wave parameters as well as various magnetospheric conditions.

During its traverse between the two hemispheres a VLF wave pulse interacts with energetic electrons of different energy and pitch angle. The precipitated energy flux thus consists of electrons that have encountered and resonated with the wave at different locations along the field line and that therefore arrive at ionospheric heights at different times. In our model we take into account the wave group travel time and the electron travel times and present the results as precipitated energy flux versus time after the injection of the wave into the magnetosphere.

Natural variable frequency VLF waves, such as lightning-generated whistlers, chorus emissions, triggered emissions, have been observed to induce energetic electron precipitation and cause ionospheric disturbances. Coherent variable frequency waves have also frequently been injected into the magnetosphere in the Siple VLF experiments. To examine the role of the frequency-time format of the interacting waves on the induced particle precipitation, we have extended the transient precipitation model to the more general cases of whistler mode waves with slowly varying frequency.

Our results show that although the temporal shape of the transient precipitation pulse induced by a variable frequency signal depends on the location of its principal interaction region, and thus its slope df/dt , there is little difference in total deposited energy or peak flux induced by signals with different frequency-time slopes under conditions of moderate wave intensities ($B_w < 10$ pT at $L=4$). When there are differences, they are controlled more by the falloff in energy of the trapped particle distribution function than by any other parameter. However, we have found that, when the wave growth in the vicinity of the phase equator or within the principal interaction region is taken into account, a signal with rising frequency is more efficient than one with decreasing frequency in inducing particle precipitation. Based on this result, the precipitation efficiency for the monochromatic cases falls between that of the riser and faller.

The precipitated electrons can cause ionization and conductivity enhancements, heating and the emission of X rays and light when penetrating to the lower ionosphere. Recent experiments have shown associations between isolated bursts of precipitating electrons at middle-latitudes and whistlers and triggered emissions. We have compared the predictions of our transient precipitation model with three

ground based observations of the ionospheric effects of particle precipitation. These three different events represent three different methods of detecting the ionospheric effects of precipitating electron fluxes, i.e., the observations of perturbations of sub-ionospheric VLF signals, bremsstrahlung X rays, and photoemissions.

Previous interpretation of these events was often based on comparing the measured time lag between the wave and precipitation bursts with the estimated travel times of the wave and the particles from the interaction region to the observation site. In general it was not possible to estimate the amplitude or the structure of the precipitation pulse that would be induced by a given wave. Using our model, however, we are able to consider the effects of changing frequency and full nonlinear scattering involving relativistic energies and thus obtain the precipitation flux level, pulse shape and associated time relationships and compare these with the reported data.

In summary, our results have demonstrated that the test particle computer model can be used to interpret the observed experimental results. Furthermore, the model results and observations, used together, provide a basis for additional diagnostics of the various parameters of the cold and energetic particle distributions in the magnetosphere. The successful application of the model to different experimental situations indicates its versatility; an obvious potential application is in planning of future experiments aimed at detecting wave-induced electron precipitation and its ionospheric effects.

B. RECOMMENDATIONS FOR FUTURE WORK

Incoherent Waves

We have limited our study to the specific case of interactions involving coherent VLF signals. We have shown that for fixed input wave energy the total precipitated energy density is not strongly dependent on the frequency-time format of the input signal as long as the same frequency range is considered. It is then conjectured that an incoherent wave with the same input wave energy and covering the same frequency range might induce the same amount of precipitated energy density [Dingle, 1977]. However, this argument needs to be checked by using, for example, a simulation in which a test particle is introduced into a random (i.e., incoherent) wave structure. In so doing one should be able to compare directly the efficiency of coherent and incoherent waves in inducing particle precipitation. Moreover, the

numerical results of pitch angle scattering for the cases of incoherent wide band noise can be compared with those derived from the theory of random diffusion.

Nonducted Waves

In the present work we have considered only waves propagating longitudinally along the geomagnetic field lines, as a good approximation to the propagation of whistler mode waves trapped within field-aligned ducts. In general, waves in the magnetosphere propagate in both ducted and nonducted modes [Bell *et al.*, 1981]. Since ducts occupy only a small fraction of the magnetosphere, most of the wave energy that is either injected from the ground or generated in the medium propagates in the nonducted mode. Nonducted waves do not generally propagate along the magnetic field line and thus are usually not observed on the ground. However, these waves need to be considered in obtaining a complete picture of electron precipitation phenomena.

To model the pitch angle scattering due to the nonducted waves, it is necessary to employ a different set of equations of motion to account for the non-zero wave normal angles with respect to the direction of the static magnetic field. Moreover, ray tracing in the anisotropic magnetospheric medium must be carried out in order to obtain the nonducted wave structure along a given field line. The topic of the gyroresonance wave-particle interaction involving coherent whistler mode VLF waves propagating at an arbitrary angle with respect to the earth's magnetic field has only recently begun to receive attention [Bell, 1983]. Based on these different equations and the wave structure obtained from ray tracing, our model and formulation could be easily extended to the case of nonducted waves, since the schemes for tracing the adiabatic motion of particles and for manipulation of the distribution function need not be changed.

Wave Energy Distributions

Theoretical modeling can predict the relative precipitation efficiency of incoherent and coherent waves as well as ducted and nonducted waves under comparable conditions, for instance, for constant input wave energy. However, to understand the relative importance to the global precipitated loss of electrons from the magnetosphere of different classes of waves, we need to know the wave energy distributions of different waves.

Lyons *et al.* [1972] claimed that lightning-generated whistlers made only a minor contribution to the total whistler mode wave energy in the magnetosphere. They

thus concluded that wave energy which was generated naturally within the magnetosphere, such as plasmaspheric hiss, dominated the magnetospheric wave spectrum and controlled the pitch angle diffusion of radiation belt electrons. However, the frequent occurrence of lightning strokes and whistlers observed on satellites [R. A. Helliwell, private communication] suggests the existence of potentially fruitful coherent wave energy that should be able to scatter particles effectively. To clarify the relative spectral intensities of incoherent magnetospheric noise and coherent whistler waves, further study such as statistical survey of satellite data should be performed.

Another topic of interest is the study of the roles of the ducted and nonducted wave energies on the precipitated electron energy into the ionosphere. Siple VLF experiments have shown that ducted signals often trigger emissions but nonducted signals are rarely associated with triggered emissions [Bell *et al.*, 1981, 1983]. This could imply higher wave energy densities within the whistler mode ducts and thus greater downcoming precipitated electron energy fluxes around the exits of the ducts. This conjecture needs to be experimentally investigated.

Energetic Particle Distributions

Our results, in particular the computed precipitation flux, depend strongly on the energetic particle distribution $f(E, \alpha)$ or the measurable differential energy spectrum Φ_E . Siple experiments have shown the correlations between the photometer measurements and natural signals propagating outside the plasmopause, as discussed in chapter IV. The photometer is suitable for investigating the effects due to the lower range of the electron energies [Helliwell *et al.*, 1980] and should be capable of detecting the lower energy electrons precipitated by Siple signals. The fact that the precipitation induced by Siple signals have so far not yet been observed might be attributed to a lower trapped flux level during quiet time conditions that are necessary for the transmission and thus the wave amplification of the injected signal. The simultaneous operations of the satellite particle detector to measure the trapped electron distribution in the magnetosphere and the ground based detectors to observe the ionospheric effects of precipitated electrons are then essential for the clarification of the role of $f(E, \alpha)$ on wave-induced precipitation. In addition, due to the lack of useful published particle data, better measurements of $f(E, \alpha)$ over L -shells in different magnetospheric conditions are necessary in order to obtain better theoretical predictions from our model.

Calculations of precipitated energy spectra

The energy spectrum of the electrons that comprise the peak of a precipitation pulse has been described by *Inan et al.* [1977]. It was found that the maximum contribution to the flux comes from the lower energy end of the spectrum for typical distributions. In the discussion in connection with Figure 3.5, it was pointed out that the energy-versus-time diagram defines the region in the time-energy domain where we expect to observe the precipitated flux after the injection of the input wave. It would be useful to calculate the precipitated energy spectrum in $\text{ergs/cm}^2 \text{ s keV}$ as a function of energy and time. This would give the information about the energy distribution of precipitated electrons at a given time as well as the time evolution of precipitation at a particular energy. One could thus obtain a more detailed signature of precipitation induced by different signals.

Calculations involving higher pitch angles

Scattering of higher pitch angle particles and thus perturbations of trapped electron distributions by coherent VLF waves is important to many magnetospheric phenomena involving growth and damping of waves, such as the 'quiet band' discussed in Appendix C. A thorough investigation requires calculations involving a large number of test particles. The study of how the particle population is modified by VLF waves, however, is essential in understanding the effects of wave-particle interactions and provides a basis for designing satellite experiments using particle detectors for observing wave-induced perturbation and for deducing particle distributions from wave data.

APPENDIX A: THE RELATIONSHIP BETWEEN $f(E, \alpha)$ AND Φ_E

We represent the trapped energetic electron population along a geomagnetic field line by a distribution function $f(E, \alpha)$ at the equator. The distribution function is defined in velocity space such that it gives the number density (el/cm³) of electrons when multiplied by the velocity space volume element $v^2 \sin \alpha dv d\alpha d\phi$ or $v_{\parallel}^2 (\sin \alpha / \cos^3 \alpha) dv_{\parallel} d\alpha d\phi$. Note that $E = mc^2[(1 - v^2/c^2)^{-1/2} - 1] = mc^2[(1 - v_{\parallel}^2/c^2 \cos^2 \alpha)^{-1/2} - 1]$.

In many experiments the particle information is often given in terms of the differential energy spectrum Φ_E in el/cm² s sr keV. The quantity $\Phi_E dA d\Omega dE dt$ then represents the number of particles with energy between E and $E + dE$ which, during the time dt , traverse the element of area dA in a direction within the element of solid angle $d\Omega$ around the normal to dA . The elements dA and $d\Omega$ are shown in Figure A1, where the angular coordinates θ and ϕ specify the direction of the normal to dA .

From conservation of particles Φ_E is related to the distribution function $f(E, \alpha)$ by the following equation

$$\Phi_E dA d\Omega dE dt = f(E, \alpha) v^2 dv d\Omega v dt dA. \quad (A1)$$

The v is the magnitude of the velocity of an electron with energy E . The volume element $v^2 dv d\Omega$ in velocity space accounts for those particles with direction of motion lying within the solid angle $d\Omega$ and with energy between E and $E + dE$. The element $v dt dA$ represents the volume in ordinary space through which these particles pass during the time dt .

The relationship between dE and dv is given by

$$dE = d\left\{mc^2\left(\frac{1}{\sqrt{1 - v^2/c^2}} - 1\right)\right\} = \frac{mc^2}{(1 - v^2/c^2)^{3/2}} \frac{v dv}{c^2} = mc^2 \gamma_E^3 \frac{v dv}{c^2}, \quad (A2)$$

where γ_E is the relativistic factor associated with the energy E . From (A1) and (A2) we have

$$f(E, \alpha) = \Phi_E \frac{m \gamma_E^3}{v^2}. \quad (A3)$$

(A3) indicates that for energies for which $\gamma_E^3 \simeq 1$, if Φ_E varies as v^{-n} , the distribution function will behave as v^{-n-2} .

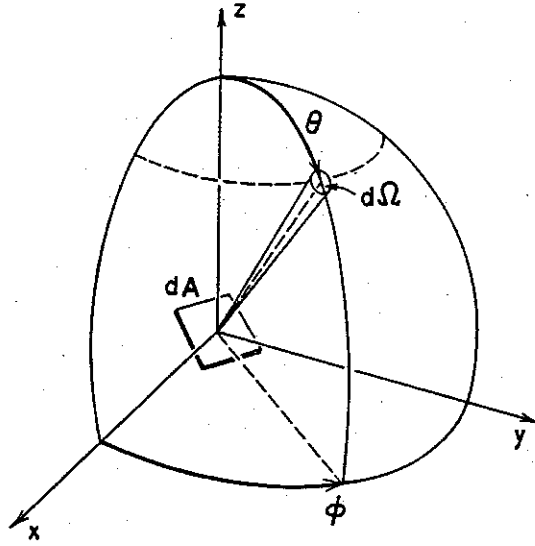


FIGURE A1 DEFINITION OF THE DIFFERENTIAL ENERGY SPECTRUM.

Since $v^2/c^2 = (\gamma_E^2 - 1)/\gamma_E^2$, (A3) becomes

$$f(E, \alpha) = \Phi_E \left(\frac{m}{c^2} \right) \left(\frac{\gamma_E^5}{\gamma_E^2 - 1} \right). \quad (\text{A4})$$

If $f(E, \alpha) = AE^{-n/2}g(\alpha)$ for $\alpha \geq \alpha_{eq}^{lc}$ with $g(\alpha) = 1$ at $\alpha = 90^\circ$ and if Φ_{E_0} is the differential energy spectrum of electrons at a given energy E_0 and with $\alpha = 90^\circ$ pitch angle, then the constant A can be related to Φ_{E_0} by

$$A = \Phi_{E_0} \left(\frac{m}{c^2} \right) \left(\frac{\gamma_0^5}{\gamma_0^2 - 1} \right) E_0^{n/2}, \quad (\text{A5})$$

where γ_0 is the γ_E for $E = E_0$. (A5) is the same as equation (2.29).

Note that from the Liouville theorem (see, e.g., Hess [1968]) Φ_E stays constant along a particle's orbit, that is,

$$\Phi_E(\alpha_1, B_1) = \Phi_E(\alpha_2, B_2) \quad (\text{A6})$$

along a field line, where α_1 and α_2 are the pitch angles and B_1 and B_2 are the magnetic field strengths at two different points, respectively, and are related by the mirror equation $\sin^2 \alpha_1 / B_1 = \sin^2 \alpha_2 / B_2$. Therefore Φ_E at the equator can be deduced from that measured elsewhere on the same field line.

APPENDIX B: WAVE AMPLITUDE VARIATION

In our model a short VLF wave pulse is assumed to enter into the magnetosphere at 1000 km altitude at time $t=0$ and is assumed to propagate longitudinally ($\mathbf{k} \parallel \mathbf{B}_0$) in a duct along the earth's magnetic field line.

For a monochromatic wave pulse the temporal pulse duration does not change during propagation, neglecting the possible distortion of the front and tail ends of the pulse [Chang and Helliwell, 1980]. If no loss of energy is assumed, the power flow along the duct is then constant. However, the power density varies, since the cross-sectional area of the duct is inversely proportional to the static magnetic field intensity B_0 or to the cold plasma electron frequency ω_H , assuming that the whistler mode wave is the superposition of a large number of rays that fill up the duct. In this slowly varying medium, the variation of the wave magnetic field intensity B_w along the field line can then be expressed as

$$B_w = B_{w\text{eq}}(\omega_H k / \omega_{H\text{eq}} k_{\text{eq}})^{1/2} \quad (B1)$$

since B_w^2 is proportional to the power density and the refractive index $\mu (=ck/\omega)$. In (B1), ω_H and k are local values, $\omega_{H\text{eq}}$ and k_{eq} are the equatorial values, $B_{w\text{eq}}$ is the equatorial wave intensity, c is the speed of light in free space, and ω is the angular wave frequency.

For a variable frequency signal the pulse duration varies due to the dispersive nature of the medium. The wave power density and so the wave intensity will depend on this additional factor. The local group velocity of a wave component of frequency f along the field line is given [Helliwell, 1965] by

$$v_g = 2c \frac{f^{1/2}(f_H - f)^{3/2}}{f_P f_H} \quad (B2)$$

where $f_P = \omega_P/2\pi$ and $f_H = \omega_H/2\pi$ are the local plasma frequency and gyrofrequency, respectively, and $\omega_P^2 \gg \omega_H^2$ has been assumed. The travel time, or the group delay, of this frequency component from the injection point to a point with coordinate z along the field line can be expressed as

$$t_g(f, z) = \int_{1000\text{km}}^z \frac{dz}{v_g} = \frac{1}{2c} \int_{1000\text{km}}^z \frac{f_P f_H}{f^{1/2}(f_H - f)^{3/2}} dz. \quad (B3)$$

Consider one component of a variable frequency signal with frequency f which is injected into the field line at time t . An adjacent frequency component $f + \Delta f$ is injected at time $t + \Delta t$. $\Delta f / \Delta t$ is then the slope in the $f - t$ domain of the input signal at frequency f . The components f and $f + \Delta f$ will travel to the point z at times t' and $t' + \Delta t'$, respectively. From (B3), $\Delta t'$ is then given by

$$\Delta t' = \Delta t + t_g(f + \Delta f, z) - t_g(f, z). \quad (B4)$$

Note that Δt and $\Delta t'$ may have different signs; however, in this report we do not treat this case. The difference in group delay can be approximated by

$$t_g(f + \Delta f, z) - t_g(f, z) = \frac{\partial t_g(f, z)}{\partial f} \Delta f \quad (B5)$$

where $\partial t_g(f, z) / \partial f$ is the slope of the $t_g(f)$ versus f curve measured at f and can be derived from (B3) as

$$\frac{\partial t_g(f, z)}{\partial f} = \frac{1}{2c} \int_{1000\text{km}}^z \frac{f_P f_H}{f^{1/2} (f_H - f)^{3/2}} \left[\frac{3}{2} \frac{1}{(f_H - f)} - \frac{1}{2f} \right] dz. \quad (B6)$$

Consequently, (B4) can be rewritten as

$$\frac{\Delta t'}{\Delta t} = 1 + \frac{\partial t_g(f, z)}{\partial f} \frac{\Delta f}{\Delta t}. \quad (B7)$$

If the energy contained between $f + \Delta f$ and f is conserved, the local power flow or power density corresponding to f is inversely proportional to its duration Δt . The wave intensity at z of this frequency component will accordingly be modified by the factor $(\Delta t / \Delta t')^{1/2}$ in addition to that given by (B1). Note that we have assumed that $\Delta t'$ does not go to zero. The complete expression for computing the wave intensity variation along the field line using the equatorial wave intensity as a reference is then given by

$$B_w(f, z) = B_{w\text{eq}}(f) \left[\frac{\omega_H(z) k(f, z) (1 + [\partial t_g(f, z_{\text{eq}}) / \partial f] [\Delta f / \Delta t])}{\omega_{H\text{eq}} k_{\text{eq}}(f) (1 + [\partial t_g(f, z) / \partial f] [\Delta f / \Delta t])} \right]^{1/2} \quad (B8)$$

where f and z indicate the dependence of the different quantities on the frequency and position along the field line, respectively, eq represents equatorial values, and $\Delta f / \Delta t$ is the slope of the signal in the input $f - t$ domain. Equations (B7) and (B8) are used in all of the model computations reported in this report.

APPENDIX C: TEST PARTICLE CALCULATIONS RELATED TO THE QUIET BAND PHENOMENON

The effect of 'quiet band' was discovered during the Siple transmitter experiments [Raghuram *et al.*, 1977b]. It was found that sometimes amplified signals are accompanied by a suppression of background natural noise in a narrowband just below the transmitter carrier frequency. Within this band, which is about 50–200 Hz wide, the natural noise is attenuated by more than 6 dB. The mechanism of the quiet band is so far not fully known. Modification of the electron distribution function involving pitch angle scattering of these electrons by a strong coherent wave has been proposed as an possible explanation [Raghuram, 1977; Cornilleau-Wehrlin and Gendrin, 1979].

Raghuram [1977] used a test particle simulation approach to calculate the modification of electron distribution due to wave-induced pitch angle scattering near the equator. Nevertheless, he could not determine whether the quiet band is due to the slopes in the modified distribution function or due to a reduction in the trapped flux. In his calculations only one pitch angle ($\alpha=30^\circ$) was considered and it was pointed out that an integration over all pitch angles should be done to obtain the true perturbed distribution.

Here we give one result of a similar kind of calculation using our test particle model by including a range of pitch angles. The calculation is done at $L = 3.5$ for a coherent wave frequency of 5.95 kHz and is shown in Figure C1. It was indicated by Raghuram, [1977] that $L = 3.5$ might be the optimum L value for production of quiet bands. We use a diffusive equilibrium model with an equatorial electron density of 600 el/cm³ for the cold plasma distribution and a dipole model for the earth's magnetic field. The wave intensity is taken to be $B_w=10$ pT on the upstream side of the particles and negligibly small on the down stream side to account for wave amplification across the equator [Helliwell and Inan, 1982]. We consider particles in a range of pitch angle between 15° and 35° and in a range of equatorial parallel velocity within a few percent of the equatorial resonant parallel velocity $v_{\parallel 0}$, defined as the resonant v_{\parallel} of particles at 30° pitch angle resonating with a 5.95 kHz wave. The bin size in pitch angle is 1° and the bin size in v_{\parallel} is 0.1% of $v_{\parallel 0}$. A total of 14,112 test particles has been used in this case. Note that a 1% increase in v_{\parallel} above $v_{\parallel 0}$ would correspond to a 50 Hz reduction in resonant wave frequency below 5.95 kHz, as indicated by the horizontal scales in Figure C1.

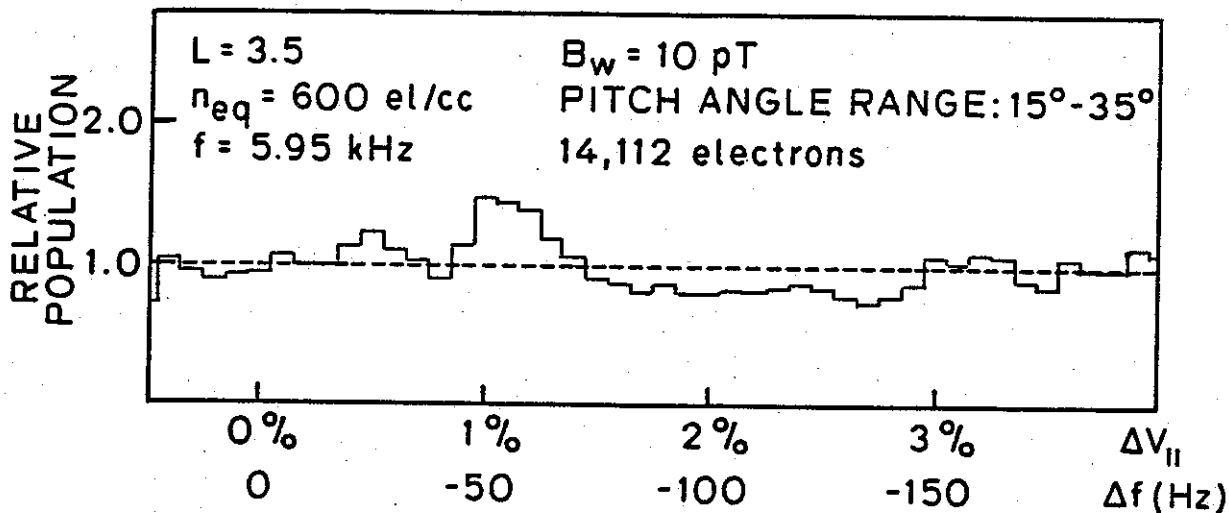


FIGURE C1 PERTURBATION OF ELECTRON POPULATION RESULTING FROM RESONANT INTERACTION WITH A 5.95 KHZ WAVE. The dashed line represents the initial isotropic distribution. A total of 14,112 test particles in the pitch angle range of 15° – 35° were used in the calculation.

The initial particle distribution is taken to be constant as a function of $v_{||}$ as represented by the dashed line. After a one pass interaction with the wave, the particle population is modified and is shown as the stepwise curve in Figure C1. It is noticed that the modified distribution shows a depletion region at 1.5% – 3% in $\Delta v_{||}$ with a reduction in flux of about 20%. However, the flux enhancement near $1\% \Delta v_{||}$ is puzzling. The correlation between this full distribution calculation and the observed data is still not good enough to establish a satisfactory interpretation. The initial distribution might not be flat as was assumed here in order to account for the existence of the hiss band. Also it might take several bounce periods for the depression in $v_{||}$ distribution to build up. Further detailed study of the quiet band effect should include different initial distributions as well as the consideration of more than one encounter between the wave and the particles.

It was argued by *Cornilleau-Wehrin and Gendrin* [1979] that higher pitch angle particles could be more important as far as the wave growth rate for the hiss is concerned. The examination of the effect of higher pitch angle particles is more complicated and can not be performed by simply integrating over pitch angle to obtain the relative population versus $v_{||}$ as was done in Figure C1. The reason is as

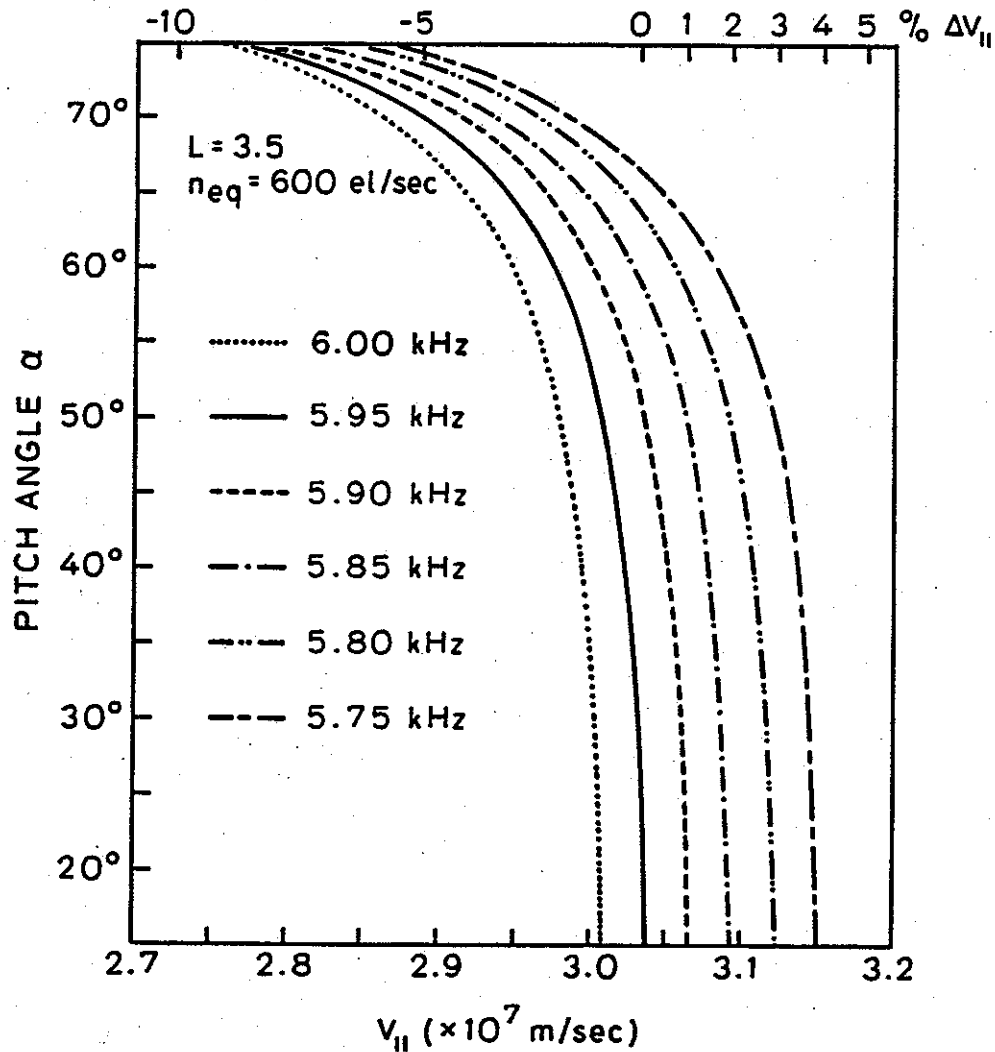


FIGURE C2 CURVES SHOWING THE RELATIONSHIP BETWEEN PITCH ANGLE AND EQUATORIAL RESONANT PARALLEL VELOCITY FOR VARIOUS WAVE FREQUENCIES. The 0% on the top scale corresponds to $v_{||}$ for 30° pitch angle and a wave frequency of 5.95 kHz.

follows. In figure C2 we show the relationship between pitch angle and equatorial resonant $v_{||}$ of particles in resonance with a wave with the wave frequency as a parameter. The percentage scale gives the deviation from $v_{||0}$ defined above. It is seen that for a given resonant wave frequency, $v_{||}$ significantly decreases as the pitch angle gets larger for those higher pitch angles. This is due to relativistic effects discussed in chapter II. It is clear from Figure C2 that for pitch angle less than 35°,

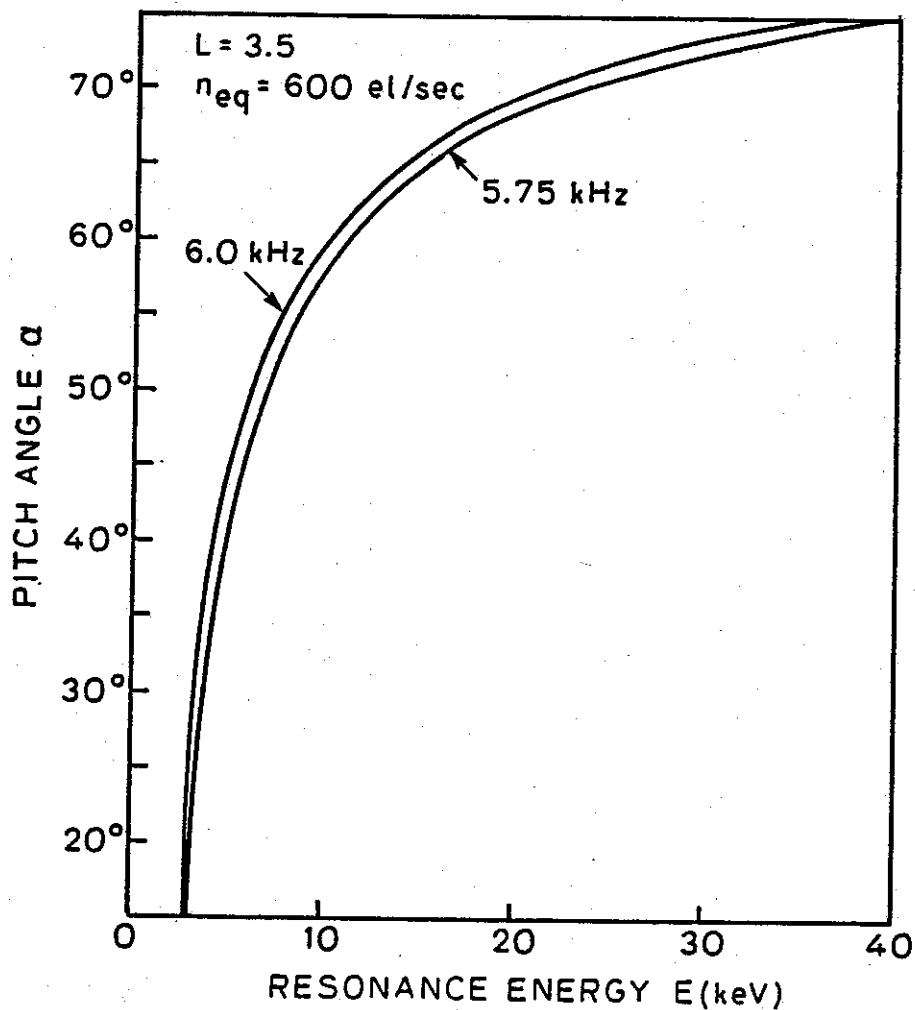


FIGURE C3 EQUATORIAL RESONANCE ENERGY AT DIFFERENT PITCH ANGLES FOR RESONANT WAVE FREQUENCIES OF 6.0 KHZ AND 5.75 KHZ.

the population versus v_{\parallel} plot is a useful illustration since v_{\parallel} can be clearly related to the wave frequency. However, for higher pitch angles a simple function of v_{\parallel} is not enough to define the wave-induced perturbations of the trapped distribution.

It is more interesting to see the behaviour of the resonant frequency curves of Figure C2 in the pitch angle and energy ($\alpha-E$) domain since it shows the detectability of the perturbation using existing particle detectors. Figure C3 shows two such curves for wave frequencies of 6.0 kHz and 5.75 kHz. Each curve shows the

equatorial resonance energy at different pitch angles. If the 6.0 kHz wave, which is assumed to cause the quiet band, does induce perturbations of electron distribution corresponding to frequencies below 6.0 kHz, in the α - E domain this perturbation would exist within the area between the two curves shown in Figure C3. Due to the narrowness of this region the detection of this effect requires high resolution both in pitch angle and in energy. For example, at low pitch angles we need an energy resolution of less than 0.2 keV. At high pitch angles above 70°, although a detector with channel bandwidth of 1 keV is enough, we need a pitch angle resolution of about 2°.

REFERENCES

- Alfvén, H., and C.-G. Fälthammar, *Cosmical Electrodynamics*, 2nd ed., Oxford University Press, London, England, 1963.
- Anderson, R. R., Wave particle interactions in the evening magnetosphere during geomagnetically disturbed periods, Ph.D. thesis, Univ. of Iowa, Iowa City, 1976.
- Angerami, J. J., A whistler study of the distribution of thermal electrons in the magnetosphere, *Tech. Rep. 3412-7*, Radiosci. Lab., Stanford Electron. Labs., Stanford Univ., Stanford, Calif., 1966.
- Angerami, J. J., and J. O. Thomas, Studies of planetary atmospheres, 1, the distribution of electrons and ions in the earth's exosphere, *J. Geophys. Res.*, **69**, 4537, 1964.
- Angerami, J. J., and D. L. Carpenter, Whistler studies of the plasmopause in the magnetosphere, 2, Equatorial density and total tube electron content near the knee in magnetospheric ionization, *J. Geophys. Res.*, **71**, 711, 1966.
- Ashour-Abdalla, M., Amplification of whistler waves in the magnetosphere, *Planet. Space Sci.*, **20**, 639, 1972.
- Banks, P. M., C. R. Chappell, and A. F. Nagy, A new model for the interaction of auroral electrons with the atmosphere: Spectral degradation, backscatter, optical emission, and ionization, *J. Geophys. Res.*, **79**, 1495, 1974.
- Barish, F. D., and R. E. Wiley, World contours of conjugate mirror locations, *J. Geophys. Res.*, **75**, 6342, 1970.
- Bell, T. F., Wave particle gyroresonance interactions in the earth's outer ionosphere, *Tech. Rep. 3412-5*, Radiosci. Lab., Stanford Electron. Labs., Stanford Univ., Stanford, Calif., 1964.
- Bell, T. F., Nonlinear Alfvén waves in a Vlasov plasma, *Phys. Fluids*, **8**, 1829, 1965.
- Bell, T. F., The nonlinear gyroresonance interaction between energetic electrons and coherent VLF waves propagating at an arbitrary angle with respect to the earth's magnetic field, submitted to *J. Geophys. Res.*, 1983.
- Bell, T. F., and O. Buneman, Plasma instability in the whistler mode caused by a gyrating electron stream, *Phys. Rev.*, **133**, A1300, 1964.
- Bell, T. F., and U. S. Inan, Transient nonlinear pitch angle scattering of energetic electrons by coherent VLF wave packets in the magnetosphere, *J. Geophys. Res.*, **86**, 9047, 1981.
- Bell, T. F., U. S. Inan, and R. A. Helliwell, Nonducted coherent VLF waves and associated triggered emissions observed on the ISEE-1 satellite, *J. Geophys. Res.*, **86**, 4649, 1981.
- Bell, T. F., U. S. Inan, I. Kimura, H. Matsumoto, T. Mukai, and K. Hashimoto, EXOS-B/Siple VLF wave-particle interaction experiments. 2. Transmitter signals and associated emissions, *J. Geophys. Res.*, **88**, 295, 1983.
- Berger, M. J., S. M. Seltzer, and K. Maeda, Some new results on electron transport in the atmosphere, *J. Atmos. Terr. Phys.*, **36**, 591, 1974.

- Bernhardt, P. A., and C. G. Park, Protonospheric-ionospheric modeling of VLF ducts, *J. Geophys. Res.*, **82**, 5222, 1977.
- Brice, N., Fundamental of VLF emission generation mechanism, *J. Geophys. Res.*, **69**, 4515, 1964.
- Brinca, A. L., Whistler sideband growth due to nonlinear wave particle interaction, *J. Geophys. Res.*, **77**, 1972.
- Budden, J. G., *Radio Waves in the Ionosphere*, Cambridge University press, Cambridge, England, 1961.
- Bud'ko, N. I., V. I. Karpman, and O. A. Pokshtelov, Nonlinear theory of the monochromatic circularly polarized VLF and ULF waves in the magnetosphere, *Cosmic Electrodyn.*, **3**, 147, 1972.
- Burtis, W. J., and R. A. Helliwell, Magnetospheric chorus: Amplitude and growth rate, *J. Geophys. Res.*, **80**, 3265, 1975.
- Carpenter, D. L., Whistler evidence of a 'knee' in the magnetospheric ionization density profile, *J. Geophys. Res.*, **68**, 1675, 1963.
- Carpenter, D. L., Whistler studies of the plasmapause in the magnetosphere; temporal variations in the position of the knee and some evidence on plasma motions near the knee, *J. Geophys. Res.*, **71**, 693, 1966.
- Carpenter, D. L., and C. G. Park, On what ionospheric workers should know about the plasmapause-plasmasphere, *Rev. Geophys. Space Phys.*, **11**, 13, 1973.
- Carpenter, D. L., and T. R. Miller, Ducted magnetospheric propagation of signals from the Siple, Antarctica, VLF transmitter, *J. Geophys. Res.*, **81**, 2692, 1976.
- Carpenter, D. L., and N. T. Seely, Cross- L plasma drifts in the outer plasmasphere: quiet time patterns and some substorm effects, *J. Geophys. Res.*, **81**, 2728, 1976.
- Carpenter, D. L., and J. W. LaBelle, A study of whistlers correlated with bursts of electron precipitation near $L=2$, *J. Geophys. Res.*, **87**, 4427, 1982.
- Chang, D. C. D., and R. A. Helliwell, Emission triggering in the magnetosphere by controlled interruption of coherent VLF signals, *J. Geophys. Res.*, **84**, 7170, 1979.
- Chang, D. C. D., and R. A. Helliwell, VLF pulse propagation in the magnetosphere, *IEEE Trans. Antennas Propagat.*, **AP28**, 170, 1980.
- Chang, H. C., and U. S. Inan, Quasi-relativistic electron precipitation due to interactions with coherent VLF waves in the magnetosphere, *J. Geophys. Res.*, **88**, 318, 1983a.
- Chang, H. C., and U. S. Inan, A theoretical model study of observed correlations between whistler mode waves and energetic electron precipitation events in the magnetosphere, *J. Geophys. Res.*, in press, 1983b.
- Chang, H. C., U. S. Inan, and T. F. Bell, Energetic electron precipitation due to gyroresonant interactions in the magnetosphere involving coherent VLF waves with slowly-varying frequency, *J. Geophys. Res.*, **88**, 7037, 1983.

- Cornilleau-Wehrlin, N., and R. Gendrin, VLF transmitter-induced quiet bands: a quantitative interpretation, *J. Geophys. Res.*, **84**, 882, 1979.
- Cornwall, J. M., Scattering of energetic trapped electrons by very-low-frequency waves, *J. Geophys. Res.*, **69**, 1251, 1964.
- Coroniti, F. V., F. L. Scarf, C. F. Kennel, W. S. Kurth, and D. A. Gurnett, Detection of Jovian whistler mode chorus; implications for the Io torus aurora, *Geophys. Res. Lett.*, **7**, 45, 1980.
- Crystal, T. L., Nonlinear currents stimulated by monochromatic whistler mode (WM) waves in the magnetosphere, *Tech. Rep. 3465-4*, Radiosci. Lab., Stanford Electron. Labs., Stanford Univ., Stanford, Calif., 1975.
- Das, A. C., A mechanism for VLF emissions, *J. Geophys. Res.*, **76**, 6915, 1971.
- Dingle, B., Burst precipitation of energetic electrons from the magnetosphere, Ph.D. thesis, Stanford Univ., Stanford, Calif., 1977.
- Dingle, B., and D. L. Carpenter, Electron precipitation induced by VLF noise bursts at the plasmopause and detected at conjugate ground stations, *J. Geophys. Res.*, **86**, 4597, 1981.
- Doolittle, J. H., Modification of the ionosphere by VLF wave-induced electron precipitation, *Tech. Rep. E4-21301318*, Radiosci. Lab., Stanford Electron. Labs., Stanford Univ., Stanford, Calif., 1982.
- Doolittle, J. H., and D. L. Carpenter, Photometric evidence of electron precipitation induced by first hop whistlers, *Geophys. Res. Lett.*, in press, 1983.
- Dungey, J. W., Loss of Van Allen electrons due to whistlers, *Planet. Space Sci.*, **11**, 591, 1963.
- Dysthe, K. B., Some studies of triggered whistler emissions, *J. Geophys. Res.*, **76**, 6915, 1971.
- Edgar, B. C., The structure of the magnetosphere as deduced from magnetospherically reflected whistlers, *Tech. Rep. 3438-2*, Radiosci. Lab., Stanford Electron. Labs., Stanford Univ., Stanford, Calif., 1972.
- Foster, J. C., and T. J. Rosenberg, Electron precipitation and VLF emissions associated with cyclotron resonance interactions near the plasmopause, *J. Geophys. Res.*, **81**, 2183, 1976.
- Gold, T., Motions in the magnetosphere of the earth, *J. Geophys. Res.*, **64**, 1219, 1959.
- Helliwell, R. A., *Whistlers and Related Ionospheric Phenomena*, Stanford University Press, Stanford, Calif., 1965.
- Helliwell, R. A., A theory of discrete VLF wave emissions from the magnetosphere, *J. Geophys. Res.*, **72**, 4773, 1967.
- Helliwell, R. A., Intensity of discrete VLF emissions, in *Particles and Fields in the Magnetosphere*, edited by B. M. McCormac, p. 292, D. Reidel, Hingham, Mass., 1970.

- Helliwell, R. A., Controlled VLF wave injection in the magnetosphere, *Space Sci. Rev.*, **15**, 781, 1974.
- Helliwell, R. A., Active very-low-frequency experiments on the magnetosphere from Siple Station, Antarctica, *Phil. Trans. R. Soc. London Ser. B.*, **279**, 213, 1977.
- Helliwell, R. A., and T. L. Crystal, A feedback model of cyclotron interaction between whistler-mode waves and energetic electrons in the magnetosphere, *J. Geophys. Res.*, **78**, 7357, 1973.
- Helliwell, R. A., and U. S. Inan, VLF wave growth and discrete emission triggering in the magnetosphere: A feedback model, *J. Geophys. Res.*, **87**, 4427, 1982.
- Helliwell, R. A., and J. P. Katsufakis, VLF wave injection into the magnetosphere from Siple Station, Antarctica, *J. Geophys. Res.*, **79**, 2511, 1974.
- Helliwell, R. A., and J. P. Katsufakis, Controlled wave-particle interaction experiments, in *Upper Atmosphere Research in Antarctica*, *Antarctic Res. Ser.*, vol. 29, edited by L. J. Lanzerotti and C. G. Park, AGU, Washington, D.C., 1978.
- Helliwell, R. A., J. P. Katsufakis, and M. L. Trimpi, Whistler-induced amplitude perturbation in VLF propagation, *J. Geophys. Res.*, **78**, 4679, 1973.
- Helliwell, R. A., S. B. Mende, J. H. Doolittle, W. C. Armstrong, and D. L. Carpenter, Correlations between $\lambda 4278$ optical emissions and VLF wave events observed at $L \sim 4$ in the Antarctic, *J. Geophys. Res.*, **85**, 3376, 1980a.
- Helliwell, R. A., D. L. Carpenter, and T. R. Miller, Power threshold for growth of coherent VLF signals in the magnetosphere, *J. Geophys. Res.*, **85**, 3360, 1980b.
- Hess, W. N., *The Radiation Belt and the Magnetosphere*, Blaisdell Publishing Co., Mass., 1968.
- Imhof, W. L., E. E. Gaines, and J. B. Reagan, Evidence for the resonance precipitation of energetic electrons from the slot region of the radiation belts, *J. Geophys. Res.*, **79**, 3141, 1974.
- Imhof, W. L., E. E. Gaines, and J. B. Reagan, Observations of multiple, narrow energy peaks in electrons precipitating from the inner radiation belt and their implications for wave-particle interactions, *J. Geophys. Res.*, **86**, 1591, 1981a.
- Imhof, W. L., R. R. Anderson, J. B. Reagan, and E. E. Gaines, The significance of VLF transmitters in the precipitation of inner belt electrons, *J. Geophys. Res.*, **86**, 11225, 1981b.
- Imhof, W. L., J. B. Reagan, H. D. Voss, E. E. Gaines, D. W. Datlowe, J. Mobilia, R. A. Helliwell, U. S. Inan, J. P. Katsufakis, and R. G. Joiner, Direct observation of radiation belt electrons precipitated by controlled injection of VLF signals from a ground-based transmitter, *Geophys. Res. Lett.*, **10**, 361, 1983a.
- Imhof, W. L., J. B. Reagan, H. D. Voss, E. E. Gaines, D. W. Datlowe, J. Mobilia, R. A. Helliwell, U. S. Inan, J. P. Katsufakis, and R. G. Joiner, The modulated precipitation of radiation belt electrons by controlled signals from VLF transmitters, *Geophys. Res. Lett.*, in press, 1983b.

- Inan, U. S., Non-linear gyroresonant interactions of energetic particles and coherent VLF waves in the magnetosphere, *Tech. Rep. 344-3*, Radiosci. Lab., Stanford Electron. Labs., Stanford Univ., Stanford, Calif., 1977.
- Inan, U. S., and R. A. Helliwell, DE-1 observations of VLF transmitter signals and wave-particle interactions in the magnetosphere, *Geophys. Res. Lett.*, **9**, 917, 1982.
- Inan, U. S., T. F. Bell, D. L. Carpenter, and R. R. Anderson, Explorer 45 and Imp 6 observations in the magnetosphere of injected waves from the Siple Station VLF transmitter, *J. Geophys. Res.*, **82**, 1177, 1977.
- Inan, U. S., T. F. Bell, and R. A. Helliwell, Nonlinear pitch angle scattering of energetic electrons by coherent VLF waves in the magnetosphere, *J. Geophys. Res.*, **83**, 3235, 1978.
- Inan, U. S., T. F. Bell, and H. C. Chang, Particle precipitation induced by short-duration VLF waves in the magnetosphere, *J. Geophys. Res.*, **87**, 6243, 1982.
- Inan, U. S., H. C. Chang, and R. A. Helliwell, Electron Precipitation Zones Around Major Ground Based VLF Signal Sources, submitted to *J. Geophys. Res.*, 1983.
- Karpman, V. I., Ja. N. Istomin, and D. R. Shklyar, Nonlinear frequency shift and self-modulation of the quasi-monochromatic whistlers in the inhomogeneous plasma (magnetosphere), *Planet. Space Sci.*, **22**, 859, 1974a.
- Karpman, V. I., Ja. N. Istomin, and D. R. Shklyar, Nonlinear theory of a quasi-monochromatic whistler mode wave packet in inhomogeneous plasma, *Plasma Phys.*, **16**, 685, 1974b.
- Karpman, V. I., Ja. N. Istomin, and D. R. Shklyar, Effects of nonlinear interaction of monochromatic waves with resonant particles in the inhomogeneous plasma, *Physica Scripta*, **11**, 278, 1975.
- Kennel, C. F., Consequences of a magnetospheric plasma, *Rev. Geophys.*, **7**, 379, 1969.
- Kennel, C. F., and H. E. Petschek, Limit on stably trapped particle fluxes, *J. Geophys. Res.*, **71**, 1, 1966.
- Koons, H. C., B. C. Edgar, and A. L. Vampola, Precipitation of inner zone electrons by whistler mode waves from VLF transmitters UMS and NWC, *J. Geophys. Res.*, **86**, 640, 1981.
- Liemohn, H. B., Radiation belt particle orbits, *Rep. D1-82-0116*, Boeing Scientific Labs., June, 1961.
- Lohrey, B., and A. B. Kaiser, Whistler-induced anomalies in VLF propagation, *J. Geophys. Res.*, **84**, 5722, 1979.
- Lyons, L. R., and R. M. Thorne, Equilibrium structure of radiation belt electrons, *J. Geophys. Res.*, **78**, 2142, 1973.
- Lyons, L. R., and D. J. Williams, The quiet time structure of energetic (35-560 keV) radiation belt electrons, *J. Geophys. Res.*, **80**, 943, 1975.
- Lyons, L. R., R. M. Thorne, and C. F. Kennel, Pitch-angle diffusion of radiation belt electrons within the plasmasphere, *J. Geophys. Res.*, **77**, 3455, 1972.

- Matsumoto, H., Theoretical studies on whistler mode wave particle interactions in the magnetospheric plasma, Ph.D. thesis, Kyoto Univ., Kyoto, Japan, 1972.
- Matsumoto, H., and Y. Omura, Cluster- and channel-effect phase bunching by whistler waves in a nonuniform geomagnetic field, *J. Geophys. Res.*, **86**, 779, 1981.
- Matsumoto, H., K. Hashimoto, and I. Kimura, Dependence of coherent nonlinear whistler interaction on wave amplitude, *J. Geophys. Res.*, **85**, 644, 1980.
- Mende, S. B., R. L. Arnoldy, L. J. Cahill, Jr., J. H. Doolittle, W. C. Armstrong, and A. C. Fraser-Smith, Correlation between $\lambda 4278\text{-\AA}$ optical emissions and a Pc 1 pearl event observed at Siple Station, Antarctica, *J. Geophys. Res.*, **85**, 1194, 1980.
- Nunn, D., A theory of VLF emissions, *Planet. Space Sci.*, **19**, 1141, 1971.
- Nunn, D., A self-consistent theory of triggered VLF emissions, *Planet. Space Sci.*, **22**, 349, 1974.
- Omura, Y., and H. Matsumoto, Computer simulation of basic processes of coherent whistler wave-particle interactions in the magnetosphere, *J. Geophys. Res.*, **87**, 4435, 1982.
- Palmadesso, G., and G. Schmidt, Collisionless damping of a large amplitude whistler wave, *Phys. Fluids*, **14**, 1411, 1971.
- Palmadesso, G., and G. Schmidt, Stability of a steady, large amplitude whistler wave, *Phys. Fluids*, **15**, 485, 1972.
- Park, C. G., Methods of determining electron concentrations in the magnetosphere from nose whistlers, *Tech. Rep. 3454-1*, Radiosci. Lab., Stanford Electron. Labs., Stanford Univ., Stanford, Calif., 1972.
- Park, C. G., Generation of whistler-mode side-bands in the magnetosphere, *J. Geophys. Res.*, **82**, 2286, 1981.
- Park, C. G., D. L. Carpenter, and D. B. Wiggin, Electron density in the plasmasphere: whistler data on solar cycle, annual, and diurnal variations, *J. Geophys. Res.*, **83**, 3137, 1978.
- Paulikas, G. A., Precipitation of particles at low and middle latitudes, *Rev. Geophys. Space Phys.*, **13**, 709, 1975.
- Raghuram, R., Suppression effects associated with VLF transmitter signals injected into the magnetosphere, *Tech. Rep. 3456-3*, Radiosci. Lab., Stanford Electron. Labs., Stanford Univ., Stanford, Calif., 1977.
- Raghuram, R., T. F. Bell, R. A. Helliwell, and J. P. Katsufakis, Echo-induced suppressions of coherent VLF transmitter signals in the magnetosphere, *J. Geophys. Res.*, **82**, 2787, 1977a.
- Raghuram, R., T. F. Bell, R. A. Helliwell, and J. P. Katsufakis, A quiet band produced by VLF transmitter signals in the magnetosphere, *Geophys. Res. Lett.*, **4**, 199, 1977b.
- Ratcliffe, J. A., *The Magneto-Ionic Theory and Its Application to the Ionosphere*, Cambridge University Press, Cambridge, England, 1959.

- Rees, M. H., Auroral ionization and excitation by incident energetic electrons, *Planet. Space Sci.*, 11, 1209, 1963.
- Roberts, C. S., Electron loss from the Van Allen zones due to pitch angle scattering by electromagnetic disturbances, in *Radiation Trapped in the Earth's Magnetic Field*, edited by B. M. McCormac, pp. 403-421, D. Reidel, Hingham, Mass., 1966.
- Roederer, J. G., *Dynamics of Geomagnetically Trapped Particles*, Springer, New York, 1970.
- Rosenberg, T. J., R. A. Helliwell, and J. P. Katsufakis, Electron precipitation associated with discrete very-low-frequency emissions, *J. Geophys. Res.*, 76, 8445, 1971.
- Rosenberg, T. J., J. C. Siren, D. L. Matthews, K. Marthinsen, J. A. Holtet, A. Egeland, D. L. Carpenter, and R. A. Helliwell, Conjugacy of electron microbursts and VLF chorus, *J. Geophys. Res.*, 86, 5819, 1981.
- Roux, A., and R. Pellat, A study of triggered emissions, in *Magnetospheric Particles and Fields*, edited by B. M. McCormac, p. 209, D. Reidel, Hingham, Mass., 1976.
- Roux, A., and R. Pellat, A theory of triggered emissions, *J. Geophys. Res.*, 83, 1433, 1978.
- Scarabucci, R. L., Interpretation of VLF signals observed on the OGO-4 satellite, *Tech. Rep. 3418-2*, Radiosci. Lab., Stanford Electron. Labs., Stanford Univ., Stanford, Calif., 1969.
- Schild, M. A., and L. A. Frank, Electron observations between the inner edge of the plasma sheet and the plasmasphere, *J. Geophys. Res.*, 75, 5401, 1970.
- Smith, R. L., Propagation characteristics of whistlers trapped in field-aligned columns of enhanced ionization, *J. Geophys. Res.*, 66, 3699, 1961.
- Spjeldvik, W. N., and R. M. Thorne, The cause of storm after effects in the middle latitude D-region, *J. Atmos. Terr. Phys.*, 37, 777, 1975.
- Sudan, R. N., and E. Ott, Theory of triggered VLF emissions, *J. Geophys. Res.*, 76, 4463, 1971.
- Thorne, R. M., E. J. Smith, R. K. Burton, and R. E. Holzer, Plasmaspheric hiss, *J. Geophys. Res.*, 78, 1581, 1973.
- Tolstoy, A. T. J. Rosenberg, and D. L. Carpenter, The influence of localized precipitation-induced D-region ionization enhancements on subionospheric VLF propagation, *Geophys. Res. Lett.*, 9(5), 563, 1982.
- Tsuruda, K., S. Machida, T. Terasawa, A. Nishida, and K. Maezawa, High spatial attenuation of the Siple transmitter signal and natural VLF chorus observed at ground-based chain stations near Roberval, Quebec, *J. Geophys. Res.*, 87, 742, 1982.
- Vampola, A. L., and G. A. Kuck, Induced precipitation of inner zone electrons, 1. Observations, *J. Geophys. Res.*, 83, 2543, 1978.
- Vomvoridis, J. L., and J. Denavit, Test particle correlation by a whistler wave in a non-uniform magnetic field, *Phys. Fluids*, 22, 367, 1979.

Vomvoridis, J. L., and J. Denavit, Nonlinear evolution of a monochromatic whistler wave in a nonuniform magnetic field, *Phys. Fluids*, **23**, 174, 1980.

Vomvoridis, J. L., T. L. Crystal, and J. Denavit, Theory and computer simulations of magnetospheric very low frequency emissions, *J. Geophys. Res.*, **87**, 1473, 1982.

Voss, H., and L. G. Smith, Global zones of energetic particle precipitation, *J. Atmos. Terr. Phys.*, **42**, 227, 1980.

Walt, M., W. M. MacDonald, and W. E. Francis, Penetration of auroral electrons into the atmosphere, in *Physics of the Magnetosphere*, edited by R. L. Carovillano, J. F. McClay, and H. R. Radoski, pp. 534-555, D. Reidel, Dordrecht, Holland, 1968.